2020

ESTIMATION OF VEHICLE TRAILER ROTATION USING CALIBRATED RADARS WITH MULTIPLE VIEWPOINTS

Kunle Olutomilayo
Michigan Technological University, ktolutom@mtu.edu

ESTIMATION OF VEHICLE TRAILER ROTATION USING CALIBRATED RADARS WITH MULTIPLE VIEWPOINTS

By

Kunle T. Olutomilayo

A DISSERTATION

Submitted in partial fulfillment of the requirements for the degree of

DOCTOR OF PHILOSOPHY

In Electrical Engineering

MICHIGAN TECHNOLOGICAL UNIVERSITY

2020

This dissertation has been approved in partial fulfillment of the requirements for the Degree of DOCTOR OF PHILOSOPHY in Electrical Engineering.

Department of Electrical and Computer Engineering

Dissertation Advisor:	*Dr. Daniel R. Fuhrmann*
Committee Member:	*Dr. Saeid Nooshabadi*
Committee Member:	*Dr. Timothy J. Schulz*
Committee Member:	*Dr. Timothy C. Havens*
Committee Member:	*Dr. Allan A. Struthers*
Interim Chair:	*Dr. Glen E. Archer*

Dedication

To my family

for the love and support.

Contents

List of Figures

List of Tables

Preface

This dissertation contains one published conference paper and three journal articles of which two have been submitted for publication. I, Kunle T. Olutomilayo, conducted the research alongside my advisor, Dr. Daniel R. Fuhrmann and other co-authors. The main contributions of all authors are provided for each article as follows. I contributed the most to the research and appear as the first author in each article.

Chapter 2: Estimation of Trailer-Vehicle Articulation Angle Using 2D Point-Cloud Data [1]. The article is reprinted with permission [2].

(a) K. Olutomilayo: algorithm development, investigation, methodology, simulation and programming, writing the article

(b) D. Fuhrmann: problem formulation, technical discussions, article review and editing

Chapter 3: Trailer Angle Detection Using Radar Point Clouds: A part of this article has been submitted to the IEEE Journal of Selected Topics in Signal Processing (Special Issue on Recent Advances in Automotive Radar Signal Processing).

(a) K. Olutomilayo: experiment setup, data collection, investigation, methodology, algorithm development, programming, performance analysis, writing the article

(b) M. Bahramgiri: experiment setup, data collection, technical discussions

(c) S. Nooshabadi: sponsor relationship, technical discussions

(d) J. Oh: conceptualization, technical discussions, article review

(e) M. Lakehal-Ayat: conceptualization, technical discussions

(f) D. Rogan: conceptualization, technical discussions

(g) D. Fuhrmann: sponsor relationship, technical discussions, article review and editing

Chapter 4: Least Squares Calibration of Automotive Radar Mount Angles and Translation Vectors. This article has been submitted to the IEEE Transactions on Instrumentation and Measurement.

(a) K. Olutomilayo: experiment setup, data collection, investigation, methodology, algorithm development, simulation and programming, writing the article

(b) M. Bahramgiri: experiment setup, technical discussions

(c) S. Nooshabadi: sponsor relationship, technical discussions

(d) D. Fuhrmann: sponsor relationship, technical discussions, article review and editing

Chapter 5: Extrinsic Radar Calibration with Overlapping FoV and Hitch Ball Position Estimation. This article is in preparation for submission to a journal.

(a) K. Olutomilayo: experiment setup, data collection, investigation, methodology, algorithm development, simulation and programming, writing the article

(b) M. Bahramgiri: experiment setup, technical discussions

(c) S. Nooshabadi: sponsor relationship, technical discussions

(d) D. Fuhrmann: sponsor relationship, technical discussions, article review and editing

Acknowledgments

Thanks to my wife Gbemisola, children, and parents for their love and support during this study. The support is immense as our children were born during this program.

I wrote this quote in November 2018 shortly after my qualifying examinations, *'PhD is like an apprenticeship, it really matters who you learn the trade from'.* The quote is based solely on my opinion. Thanks to my advisor, Dr. Daniel R. Fuhrmann for his guidance, superb advising, recommendations for teaching and research assistant supports amidst many others. I am grateful! I appreciate my committee members: Dr. Saeid Nooshabadi, Dr. Timothy J. Schulz, Dr. Timothy C. Havens, and Dr. Allan A. Struthers for providing useful discussions and comments. I had multiple technical discussions with Dr. Struthers on some mathematical theories which improved my mathematical modelling skills.

I also appreciate Dr. Glen E. Archer, who was my supervisor through the six semesters during which I was a teaching assistant.

A big thanks goes to the research sponsors. The work presented in Chapter 2 was supported in part by the Michigan Technological University, using funds from an endowed professorship provided by the Dave House Family Foundation. The research presented in Chapters 3 to 6 was supported by the Ford Motor Company as an

Alliance Project under Ford/MTU Master Agreement #83437205. Dr. Daniel R. Fuhrmann served as the principal investigator, while Dr. Saeid Nooshabadi and Dr. Nathir Rawashdeh served as co-principal investigators.

My appreciation also goes to Dr. Nathir Rawashdeh of the Department of Applied Computing, Michigan Technological University; Dr. JinHyoung Oh, Mohsen Lakehal-Ayat, and Douglas Rogan of Ford Greenfield Labs, Palo Alto, CA, for useful discussions and comments. Thanks to my colleague Mojtaba Bahramgiri, who we jointly setup the truck-trailer apparatus, for also providing useful discussions and comments. The truck mock-up used in this research was constructed by Michael Goldsworthy, Research Associate in the ECE Department at Michigan Tech. Thanks to Mark Sloat, Research Associate in the ECE Department at Michigan Tech, for the personal loan of his flatbed trailer used for the experiments.

Finally, I thank everyone that has contributed to my program. I am indeed grateful.

Abstract

Multiple sensors are increasingly being deployed on systems for perception applications. In particular, vehicles are becoming equipped with a suite of sensors for advanced driver assistance features and autonomous driving. This dissertation considers automotive radar sensors mounted at the rear of a vehicle with the main objective of using their point cloud detections to estimate the rotation of a trailer which is attached to the vehicle's hitch ball. A simulation-based study of the problem is presented first. Thereafter, the problem is considered with respect to experimental radar data collected in both indoor and outdoor environments; the environmental difference is in the roughness of the ground surfaces. The apparatus used for the data collection includes two radars, which provide point detections in two dimensions – range and azimuth, installed in the tail light fixtures of a truck. The estimation algorithm, based on the experimental data, includes the fusion of radar detections onto a coordinate system centered at the hitch ball position, a rotational point set registration algorithm, constrained orthogonal Procrustes optimization, and state estimation with the Kalman filter to obtain smooth estimates of the trailer rotation angle. In one implementation of the estimation algorithm, the dimensions of the radar geometry, which are required in its radar fusion procedure, are obtained by direct measurement. In another implementation, the calibration of the radar geometry is considered; two extrinsic calibration methods which estimate the dimensions of the geometry using

the radar detections are provided. The trailer angle estimation algorithm is then used with respect to the calibration parameters. The results presented show that the trailer angle estimates obtained with respect to a direct measurement of the radar geometry parameters are comparable with those obtained with respect to the calibration parameters and that the algorithms presented for trailer angle estimation and extrinsic radar calibration are feasible for deployment. It is also shown that the trailer angle estimation algorithm has improved performance with the indoor dataset than with the outdoor dataset. The challenges observed with the outdoor dataset are presented and recommended for future research.

Chapter 1

Introduction

1.1 Research Overview

Recent technological and research advances have resulted in smaller sensors which are both low-cost and readily available to the public. For instance, [1]radar systems, which were once beyond the reach of civilians, are now available in small form factors (few centimeters in length) for industrial and automotive applications. In particular, the automotive industry now uses multiple sensors to provide data for perception algorithms which enhance advanced driver assistance features and autonomous driving technologies.

[1]RADAR, which originally was an acronym for RAdio Detection and Ranging, is now widely accepted as a single word.

This dissertation considers the use of automotive radar sensors, which are installed at the rear of a vehicle, to estimate the rotation of a trailer which is attached to the hitch ball of the vehicle. The radars are installed at separate locations on the vehicle, such that their detections represent multiple viewpoints of the trailer. The point cloud detections provided by the radars are used for the estimation. One of the steps involved in the estimation, as described in this dissertation, is the fusion of detections from the radars onto a convenient coordinate system, so that the different viewpoints of the radars are merged for combined observation in the same coordinate system. Therefore, this dissertation also contains extrinsic calibration methods which estimate the radar geometry parameters required for the fusion procedure, with the objective of using the calibration parameters in the trailer angle estimation algorithm.

In the literature, the angle of trailer rotation about the hitch ball, defined with respect to the longitudinal axis of the vehicle, is often referred to as the trailer angle or the hitch angle. The angle is needed in algorithms used for trailer control and backup applications. A review of existing methods, which estimate the trailer angle, is provided in sections 2.2 and 3.2. Some challenges observed in the existing methods, based on the literature review, are listed below.

(a) Installing a new hardware or sensor at the hitch ball position to measure the trailer angle increases the production cost of the system.

(b) Methods which require a sticker to be placed on the trailer do not encourage easy

trailer replacement when a spare sticker becomes unavailable. Also, stickers can gradually become occluded with dust, thereby preventing vision-based tracking if the stickers are not cleaned regularly.

(c) Some methods require the dimensions of the trailer to be known. This also does not encourage easy trailer replacement when the replacement trailer's dimensions have not been determined.

(d) Camera-based methods, which track the trailer or a feature on the trailer, generally have a reduced performance in extreme weather conditions [3].

The approach discussed for trailer rotation estimation in this dissertation addresses the above challenges. It does not introduce a new hardware sensor; rather, it reuses the existing radars such as those installed for blind spot applications. Stickers are not used, the trailer's dimensions are not required to be known, and radar sensing has advantages over camera-based sensing in extreme weather conditions [3]. The extrinsic calibration methods presented for the radar fusion procedure are also novel to the best of our knowledge.

1.2 Organization

The remainder of this dissertation is arranged as follows:

Chapter 2 is a preliminary study of the trailer angle estimation problem. Two radars are simulated to be directly located behind the vehicle, close to the tail light fixtures, such that the radars' boresights are in the direction of the vehicle's longitudinal axis. The work was tested on synthetic data only.

Unlike the research presented in chapter 2, it became necessary to estimate the trailer angle using experimental data collected from two blind spot information radars in both indoor and outdoor environments; the outdoor environment has a rougher ground surface than the indoor environment. As seen in existing vehicular designs, blind spot information radars often have non-zero mount angles and their boresights are not in the direction of the vehicle's longitudinal axis. Chapter 3 implemented the new design constraints and presents a procedure which estimated the trailer angle.

The first step in the estimation procedure presented in chapter 3 is the fusion of radar detections. The step requires the detections from both radars to be transformed onto a coordinate system, whose origin is the hitch ball position, for further signal processing. Therefore, the radar geometry parameters required for the fusion need to be

determined. The geometry parameters used in chapter 3 are ground truth measurements obtained from the experimental apparatus with protractors and a meter rule. Meanwhile, they can be estimated. Chapters 4 and 5 present two extrinsic calibration methods which estimate the geometry parameters using the radar detections.

Chapter 6 combines the theories presented in chapters 3 to 5. The radar data collected from the indoor and outdoor environments in chapter 3 are reused for the trailer angle estimation. Unlike the use of ground truth measurements of the radar geometry in chapter 3, the trailer angle estimation algorithm makes use of the geometry parameters obtained by the extrinsic calibration methods, which are provided in chapters 4 and 5. The trailer angle estimates obtained by combining the theories are presented and discussed.

Chapter 7 provides the conclusions based on the results obtained from testing the trailer angle estimation algorithm and the extrinsic calibration algorithms. Some recommendations for future research are also provided.

Chapter 2

Estimation of Trailer-Vehicle Articulation Angle Using 2D Point-Cloud Data

2.1 Chapter Abstract

In the quest to achieving more autonomous features on articulated vehicles, such as backing up and trailer stability, the vehicles need to keep track of the angle of articulation for proper control. While there are existing approaches which estimate

The material contained in this chapter was previously published in the 2019 IEEE Radar Conference (RadarConf) Proceedings [2]. The work was supported by Michigan Technological University and the Dave House Family Foundation.

the angle, most of the methods require a sticker on the trailer or additional hardware, which adds to the many-sensors already on the vehicle. This study considers a typical single-trailer articulation. Our approach takes advantage of the existing radar sensors at the rear side of the vehicle. Fortunately, most vehicle manufacturers follow this design. This prevents sourcing additional hardware for the task. We demonstrate the estimation approach with simulated point clouds for one of the radars at the rear of the vehicle with a view to implementing the approach on other sensors. The methods used are ordinary least squares (OLS), principal component analysis (PCA), and maximum likelihood estimation (MLE). Based on the simulation results, all three methods were comparable for point clouds having a low variance along the vehicle's longitudinal axis. When the variance along the axis was increased, OLS had a reduced performance while the PCA and the MLE methods retained their comparable performance. Meanwhile, the MLE method required more computational resource than the PCA method.

2.2 Introduction

Articulated vehicles have attracted some recent autonomous driving research due to the potential to automate many driver-assistance features on them. A common challenge is that the vehicles are susceptible to unstable motions with varying trailer dynamics [4]. Such instabilities can result in a road crash. A well-known metric used in tracking the trailer's stability is the articulation angle, the angle θ in Fig. 2.1, with

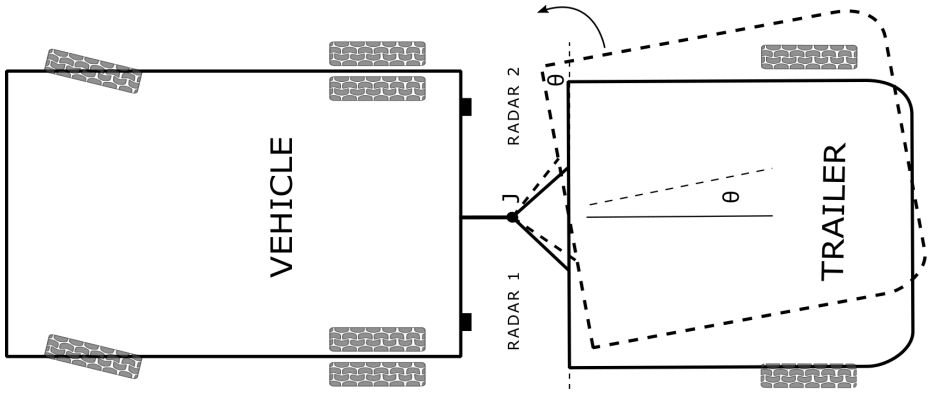

Figure 2.1: Plan view of a typical trailer-vehicle articulation.

which the trailer aligns with the vehicle. The metric is also required in applications involving automated backing up of the trailer. Therefore, the articulation angle is an important feature to study.

Previous works including [5] and [6] provided ways to measure the angle, however their methods require a new hardware or sensor on the vehicle. A more recent work [7], again requires a marker or sticker to be placed on the trailer for the angle estimation. It also introduced a computing unit together with a camera display of the tracked trailer unit to the driver. This then requires that the stickers be available before the angle can be estimated. In [8], a controller design based on fuzzy logic was proposed to track the angle. The design relies on the velocity dynamics on the hitch ball (therein referred to as the fifth wheel) and a yaw rate sensing of the trailer unit. Similarly, [9] considered the articulation joint's velocity and yaw dynamics to design a state observer for the angle estimation. The approach would also require a sensor for the trailer dynamics.

Generally, most methods require additional hardware, a computing unit, or a sticker. Meanwhile, a typical autonomous vehicle already has many sensors installed, with large amounts of data from the different sensors to process and fuse together. The data processing is also required to be done in quick succession for time-critical decisions to be made. Therefore, being able to estimate the articulation angle with neither an increase in sensors nor a reliance on a special sticker is a promising method, similar to the implementation in [10]. The invention in [10] performed sensor fusion to estimate the angle using the data obtained from sensors which could comprise of light detection and ranging sensor (LiDAR), radar, camera, and ultrasonic transducers. However, the invention required the trailer's dimensions for the estimation. This can be a limiting factor when another trailer is being towed such that the trailer's dimensions change.

We propose the angle estimation with sensor point clouds without needing the dimensions of the trailer. We also take advantage of the existing sensing devices on a typical autonomous vehicle. Most designs already include sensors at the rear of the vehicle. We demonstrate the estimation approach with one of the sensors' simulated point cloud data. While we considered an automotive radar, the same approach could be used with multiple sensing devices for their point clouds with the aim of implementing a sensor fusion.

2.3 Model

A typical trailer-vehicle articulation is presented in Fig. 2.1. The physical model is based on the general vehicular designs which include sensors at the rear side. The sensors, radars in this case, detect the spatial locations of point scatterers, which include the range and angle information. A set of those detections is referred to as the point cloud. While the radar manufacturer's proprietary algorithms may not be available to the public, the detections are available for use. An example radar that can provide 2D point clouds from point scatterers is one of NXP's latest sensors, the MR3003 transceiver [11]. The trailer, in the figure, rotates about the articulation joint J, from the vehicle-aligned position through the angle of interest θ, herein referred to as the articulation angle.

We simulated point clouds for Radar 1 represented in Figs. 2.2 and 2.3. The radar, as illustrated, has two point clouds before and after the trailer's rotation. While it is likely that some points could be false alarms, classification algorithms such as described in [12] could be employed to separate the possible false alarms. However, the scope of this work is to provide a theory into analyzing point clouds for angle estimation. Therefore, the problem statement reduces to the estimation of the articulation angle given the before-rotation and after-rotation point clouds.

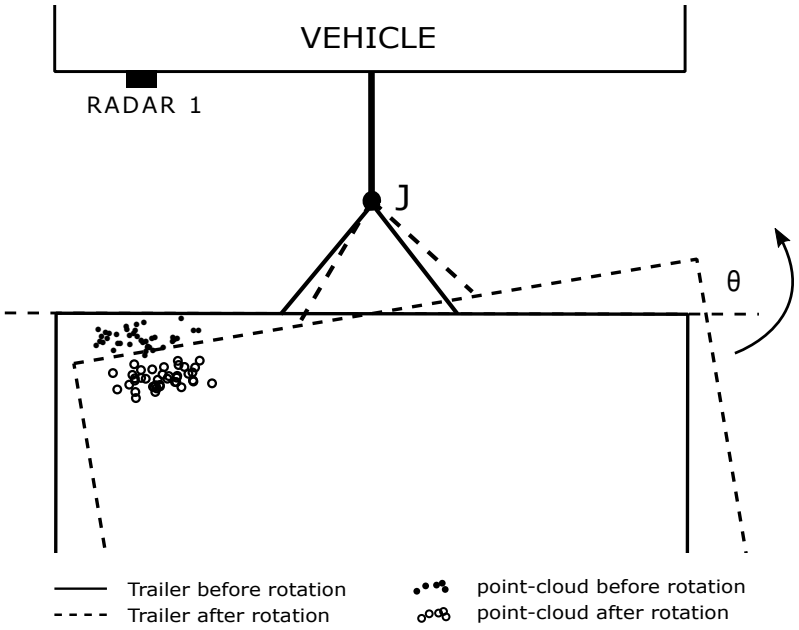

Figure 2.2: A depiction of point cloud returns having a low variance on vehicle's longitudinal axis, before and after rotation.

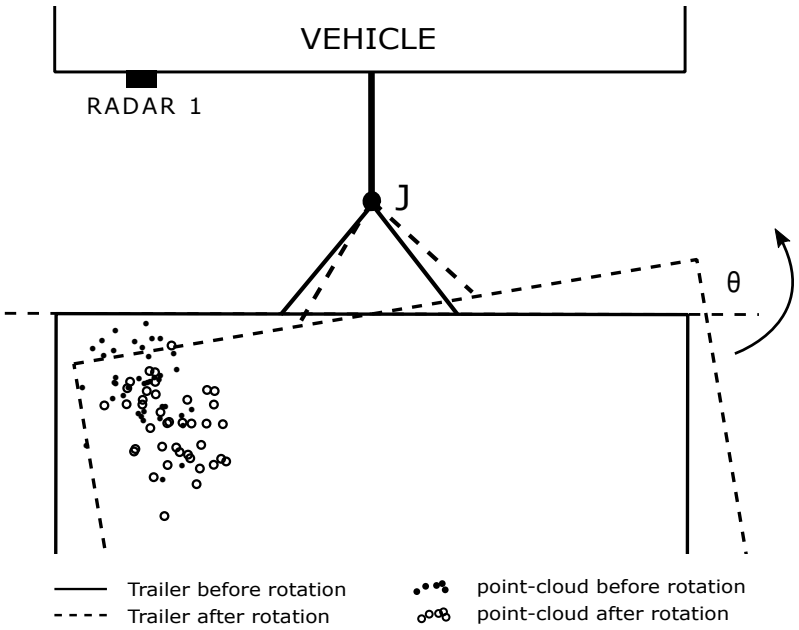

Figure 2.3: A depiction of point cloud returns having a higher variance on vehicle's longitudinal axis, before and after rotation.

For an ease in notation, the before-rotation points shall be called **reference point cloud**, and the after-rotation points called **observed point cloud**.

2.4 Estimation Methods

Three methods were explored as described in this section.

2.4.1 Ordinary Least Squares (OLS) Method

This method fits least-squares regression lines through the reference and observed point clouds, and computes the angle enclosed by the two lines. As described in Fig. 2.4, the zero-intercept regression line passes through the pivot.

Algorithm 1 Estimation via OLS

X and Y are column vectors for the x and y point-cloud coordinates respectively.

1: Determine line $\hat{y}_1 = \beta_1 x$ to fit the reference point cloud
2: Angle before rotation, $\theta_1 = tan^{-1}(\beta_1)$
3: Determine line $\hat{y}_2 = \beta_2 x$ to fit the observed point cloud
4: Angle after rotation, $\theta_2 = tan^{-1}(\beta_2)$
5: Rotation angle, $\hat{\theta} = \theta_2 - \theta_1$

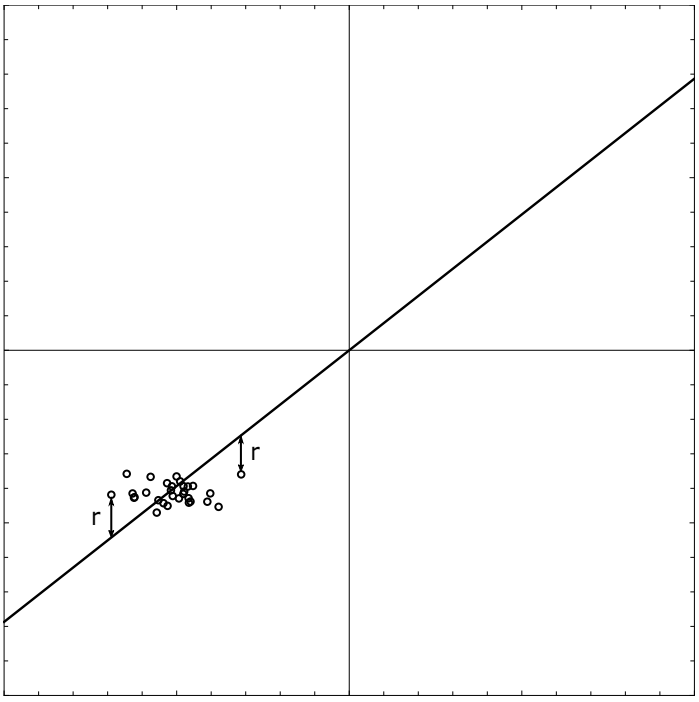

Figure 2.4: A least squares regression line that fits a dataset, together with the residual r.

Given a dataset, $D_{n\times 2}$, let X and Y be the first and second column vectors respectively. The regression line is given by

$$\hat{Y} = \beta X$$

$$Residual = \hat{Y} - Y = \beta X - Y \tag{2.1}$$

$$Cost\ function, C_{(\beta)} = \|\beta X - Y\|^2$$

$$= \beta^2 X^T X - 2\beta X^T Y + Y^T Y$$

$$\hat{\beta} = \underset{\beta}{\operatorname{argmin}}(C_{(\beta)})$$

$$\nabla_\beta\ C_{(\beta)} = 2\beta X^T X - 2X^T Y \to 0$$

$$\hat{\beta}_{ols} = (X^T Y)/(X^T X) \tag{2.2}$$

While equation 2.2 is well known, it is provided here to communicate the effect of the residual, in equation 2.1, on the estimation as presented in the simulation results. The residual, also depicted in Fig. 2.4 as r, is the vertical distance from a point to the regression line. Therefore, it is rotation-variant. Algorithm 1 describes the estimation procedure using β_{ols} for β_1 and β_2 as necessary.

2.4.2 Principal Component Analysis (PCA) Method

This method compares the principal vector-components in the point clouds and computes the angle enclosed by the vector pairs.

Algorithm 2 Estimation via PCA

Dataset, D has two columns; the point-cloud's x coordinates in the first column and the y coordinates in the second.
SVD$(D) = U\Sigma V^T$

1: Compute $V_{1_{2\times 2}}$ with the reference point cloud
($V_{1_{2\times 2}}$ contains two orthogonal vectors a_1 and b_1)
2: Compute $V_{2_{2\times 2}}$ with the observed point cloud
($V_{2_{2\times 2}}$ also contains two orthogonal vectors a_2 and b_2)
3: Rotation angle, $\hat{\theta}$ is the *signed angle* enclosed by either vector pair a_1 and a_2 OR by the pair b_1 and b_2

Given a dataset, $D_{n\times 2}$, $SVD(D_{n\times 2}) = U\Sigma V^T$ is a *rotation-scale-rotation* operation. We are interested in the rotation in 2D space as provided by the matrix V. The matrix contains two orthonormal vectors. The linear span of one of the vectors is a total least squares' fit to the dataset as illustrated in Fig. 2.5.

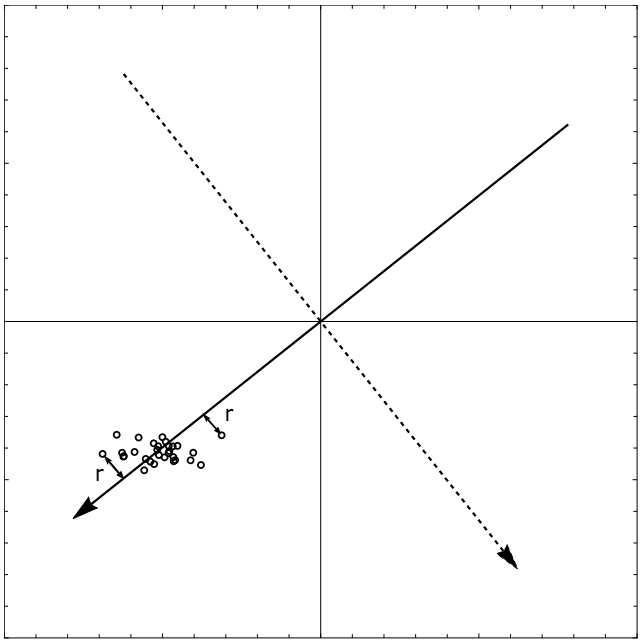

Figure 2.5: Two principal vectors in a dataset. One of the vectors' span is a total least squares' fit, unto which residual r is projected.

The residual to the line of fit, also represented in Fig. 2.5 with notation r, is an orthogonal projection to the line, having components in both coordinates. Due to this, the residual is rotation-invariant, which is an advantageous estimation feature for the PCA-approach as presented in the simulation results.

Using algorithm 2, the angle estimate is the *signed angle* enclosed by the vectors pairs. Either pair described in the algorithm suffices, since V is unitary with orthonormal vectors. Computing the *signed angle* is required to preserve the direction of rotation, i.e. the rotation angle from the reference point cloud to the observed point cloud. PCA algorithm on the dataset is equivalent to implementing the algorithm on the covariance matrix, since $SVD(D^T D)$ points to the same matrix V. Therefore, directly implementing it on the dataset saves some computation resources.

2.4.3 Maximum Likelihood Estimation (MLE) Method

In the absence of any experimental data, we do not have a model for the locations of the scatterers on the trailer as seen by the radar. Therefore, for the purpose of this simulation, we assume a bivariate Gaussian model for the point scatterers. This assumption relates to the maximum likelihood method which requires the model for both simulation of the points and estimation. Meanwhile, the first two methods (OLS and PCA) do not rely on the model for estimation. We shall explore the point scatterers with real experiments in future work.

Algorithm 3 Estimation via Maximum Likelihood

Dataset, $X_{2\times(n+p)} = [X_{a_{2\times n}},\ Q^T_{(\theta)}X_{b_{2\times p}}]$

1: Compute the sample mean, $\hat{\mu}_{(\theta)}$ using equation 2.3
2: Compute the sample covariance, $\hat{K}_{(\theta)}$ using equation 2.4
3: Form the likelihood with equation 2.9
4: $\hat{\theta} = \underset{\theta}{\text{argmax}}(-\log[\det(\hat{K}_{(\theta)})])$

It is well known that the mean and covariance estimates of the independent and identically-distributed (i.i.d.) multivariate Gaussian distribution are the sample mean and the biased sample covariance respectively [13].

$$\textit{Sample mean},\ \hat{\mu}_s = \frac{1}{n}\sum_{i=1}^{n} x_i \tag{2.3}$$

Biased sample covariance,

$$\hat{K}_s = \frac{1}{n}\sum_{i=1}^{n}(x_i - \hat{\mu}_s)(x_i - \hat{\mu}_s)^T \tag{2.4}$$

We form a dataset of i.i.d. column vectors

$$X_{2\times(n+p)} = \left[X_{a_{2\times n}},\ Q_{(\theta)}^{T} X_{b_{2\times p}}\right]$$

where $X_{a_{2\times n}}$ is the reference point cloud and $X_{b_{2\times p}}$ is the observed point cloud.

Using equations 2.3 and 2.4,

$$\hat{\mu} = \frac{1}{n+p}\sum_{i=1}^{n+p} x_i \tag{2.5}$$

$$\hat{K} = \frac{1}{n+p} S \tag{2.6}$$

$$where,\ S = \sum_{i=1}^{n+p} (x_i - \hat{\mu})(x_i - \hat{\mu})^T \tag{2.7}$$

When θ is known, there are closed-form expressions for $\hat{\mu}$ and $\hat{K}$, but θ is unknown. Therefore, stepping θ through a set hypothesized angles would estimate $\hat{\mu}$ and $\hat{K}$ for all the θ steps. The expression $Q_{(\theta)}^{T} X_{b_{2\times p}}$ in algorithm 3 performs an inverse rotation $\left(Q_{(\theta)}^{-1} = Q_{(\theta)}^{T}\right)$ on the observed points, stepping θ through a range of angles. We seek the combinations of $\hat{\mu}$ and $\hat{K}$ that maximizes the likelihood, when the combined point cloud has the least spread. Maximizing the likelihood with respect to θ gives the $\hat{\mu}$ and $\hat{K}$ combination.

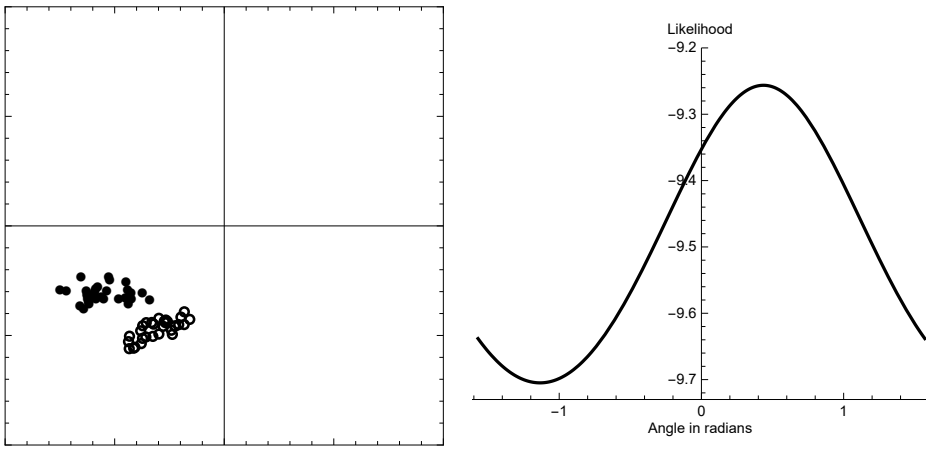

Figure 2.6: *Left*: An illustration of two point clouds. The reference point cloud is described with filled circles, and the observed point cloud with open circles. *Right*: The log likelihood is maximized when the observed point cloud, through an inverse rotation, *superimposes* the reference point cloud.

The log likelihood,

$$
\begin{aligned}
l_{(\theta,\hat{\mu},\hat{K})} &= -\frac{n+p}{2}\log\big[\det(\hat{K})\big] - \frac{1}{2}\mathrm{tr}\big[\hat{K}^{-1}S\big] + constant \\
&\qquad\qquad where,\ S = (n+p)\hat{K} \ \text{ from (2.6)} \\
&= -\frac{n+p}{2}\log\big[\det(\hat{K})\big] - \frac{n+p}{2}\mathrm{tr}\big[\hat{K}^{-1}\hat{K}\big] + constant \\
&\qquad\qquad \mathrm{tr}\big[\hat{K}^{-1}\hat{K}\big] = \mathrm{tr}\big[I_{2\times 2}\big] = \ 2 \\
&= -\frac{n+p}{2}\log\big[\det(\hat{K})\big] + constant
\end{aligned}
\tag{2.8}
$$

Maximizing the log likelihood $l_{(\theta,\hat{\mu},\hat{K})}$ with respect to θ gives the angle estimate

$$
\hat{\theta}_{mle} = \underset{\theta}{\mathrm{argmax}}\big(-\log\big[\det\big(\hat{K}_{(\theta)}\big)\big]\big) \tag{2.9}
$$

The illustration in Fig 2.6 shows the log likelihood's response as it steps θ through

the range $(-\frac{\pi}{2}, \frac{\pi}{2})$ *rad*. The function goes maximum when the the two point clouds are superimposed.

2.5 Simulation

We assume that the point cloud is bivariate Gaussian distributed i.e. the points were sampled from the distribution. Two cases were explored; *without re-sampling*, and *with re-sampling*. In the *without re-sampling* case, the observed point cloud is simply the same reference point cloud rotated by θ_{truth}. It is reasonable that in some situations the position of the point scatterers on the trailer could be the same or vary a little. For the *with re-sampling* case, the observed point cloud is the result of re-sampling a new cloud from the Gaussian distribution and rotating with θ_{truth}. The number of points n in the reference point cloud and the number of points p in the observed point cloud may also differ in this case. The pivot, J in the simulation, is set to be at the origin i.e. coordinate $(0, 0)$.

2.6 Results and Cost Analysis

2.6.1 Discussion of Results

2.6.1.1 Lower cloud variance on vehicle's longitudinal axis

In this simulation, the point clouds have a lower variance along the vehicle's longitudinal axis as depicted in Fig. 2.2. The bivariate Gaussian parameters used are

$$\text{Mean} = \begin{pmatrix} -60 \\ \\ -61 \end{pmatrix} \text{cm} \quad \text{Covariance} = \begin{pmatrix} 100 & 0 \\ \\ 0 & 50 \end{pmatrix} \text{cm}^2$$

such that the standard deviation along the longitudinal axis is $\sqrt{50}cm \approx 7.07cm$. Considering three-standard deviations up/down the mean, the point cloud spans about six standard deviations ($42.42cm$) along the axis.

Without re-sampling the point cloud, both the PCA and the MLE methods estimated θ_{truth} *perfectly* for all the simulation runs as presented in Fig. 2.7. However, the least squares approach could not, due to the rotation-variant residuals given in equation 2.1 and depicted as r in Fig. 2.4.

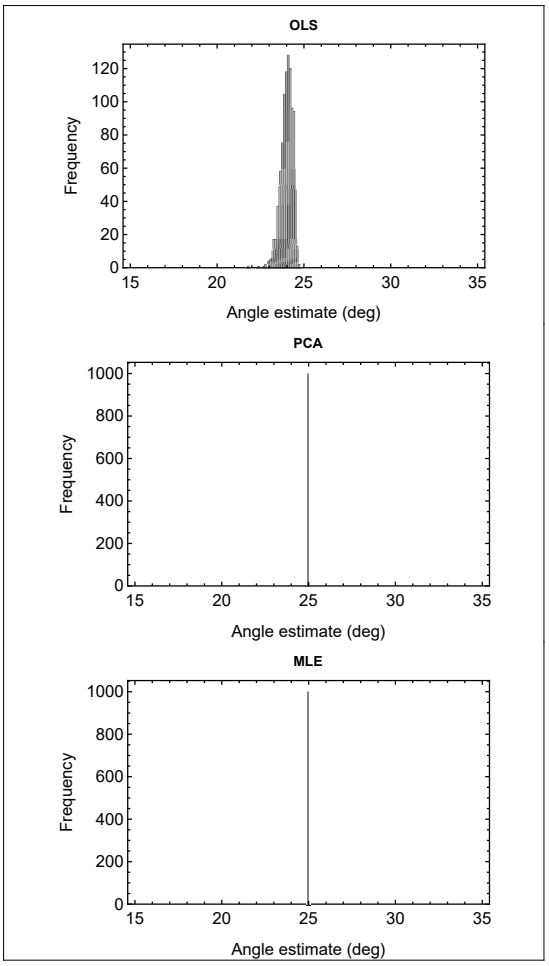

Figure 2.7: Without re-sampling the points: Monte Carlo simulation with 1000 runs, $n = p = 20,\ \theta_{truth} = 25°$.

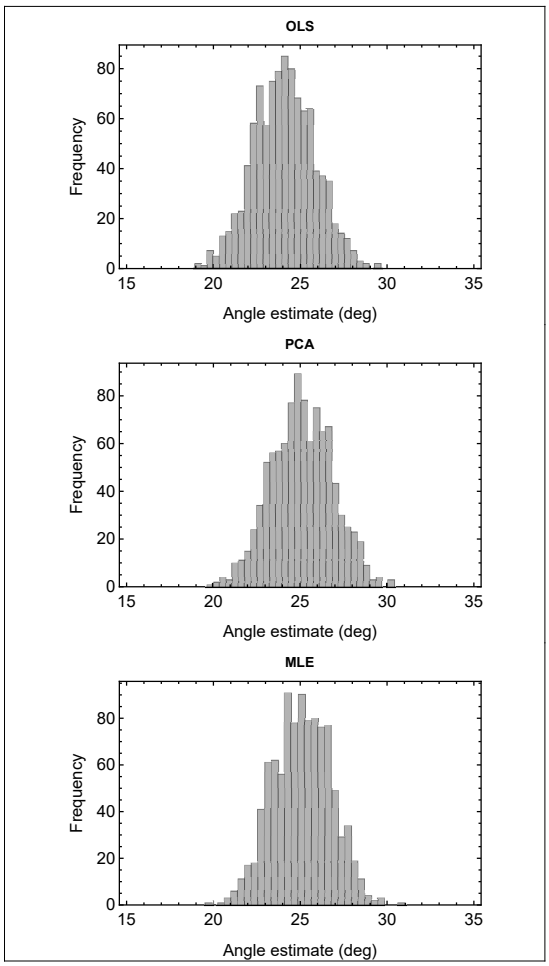

Figure 2.8: With re-sampling of points: Monte Carlo simulation with 1000 runs, $n = 20,\ p = 22,\ \theta_{truth} = 25°$. Point cloud has low variance along the vehicle's longitudinal axis.

With re-sampling of the points, the estimation would have some bias, the results are presented in Figs. 2.8, 2.9, and 2.10. The error bars in Fig. 2.9, computed from the standard deviations, put the results as statistically equivalent.

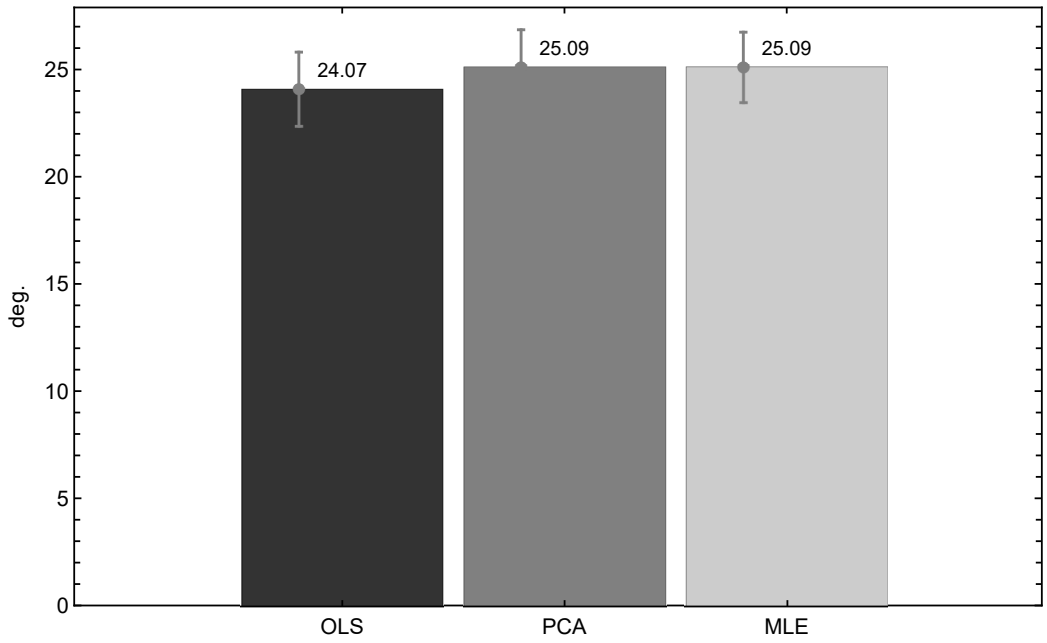

Figure 2.9: With re-sampling of points: Mean estimated angle for 1000 simulation runs, $n = 20,\ p = 22,\ \theta_{truth} = 25°$. Point cloud has low variance along the vehicle's longitudinal axis.

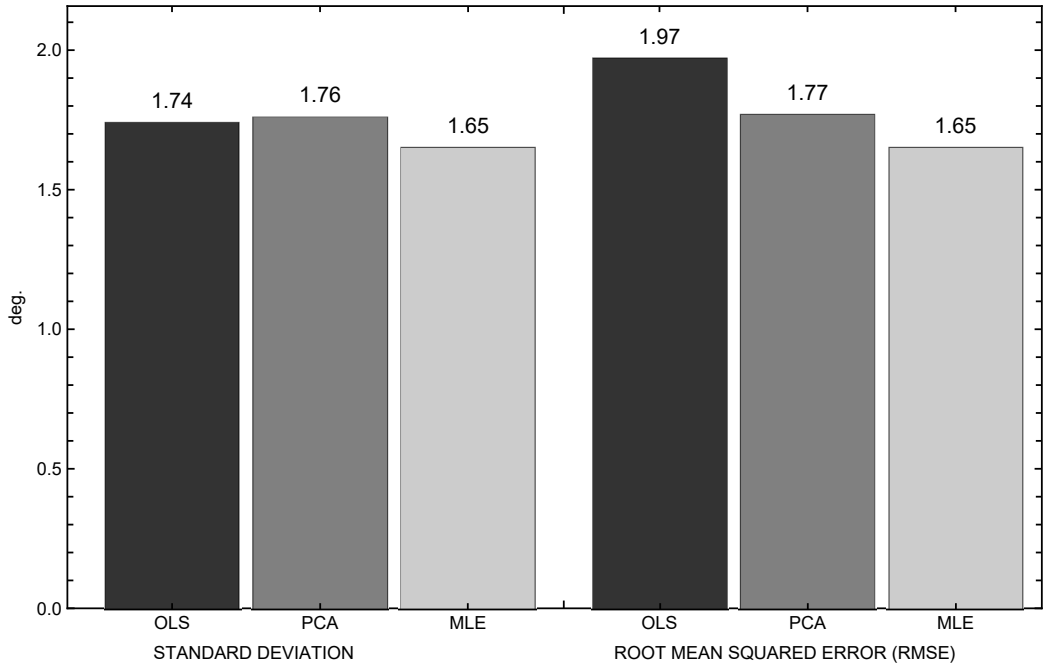

Figure 2.10: Estimation deviations for the simulation presented in Figs. 2.8 and 2.9.

2.6.1.2 Higher cloud variance on vehicle's longitudinal axis

Sometimes the point scatterers on the trailer can be more dispersed, such that the returns have a higher variance along the vehicles' longitudinal axis as depicted in Fig. 2.3. Given this consideration, the Gaussian parameters were adjusted, without changing the number of points, as follows:

$$\text{Mean} = \begin{pmatrix} -60 \\ \\ -100 \end{pmatrix} \text{cm} \quad \text{Covariance} = \begin{pmatrix} 100 & 0 \\ \\ 0 & 400 \end{pmatrix} \text{cm}^2$$

such that the standard deviation along the longitudinal axis was increased to $20cm$. This makes the point cloud span about six standard deviations ($120cm$) along the axis.

This was done with re-sampling of the point cloud. The result, as presented in Figs. 2.11 and 2.12, indicate that the PCA and MLE methods retain their comparable performance, while the least squares approach is more susceptible to the change in point cloud variance along the vehicle's longitudinal axis.

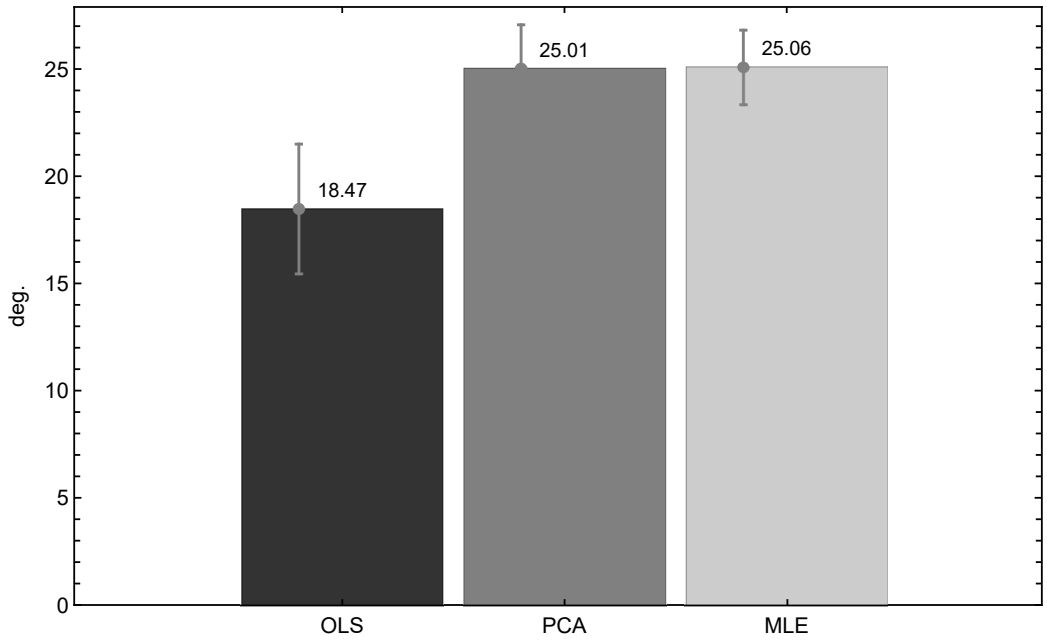

Figure 2.11: With re-sampling of points: Mean estimated angle for 1000 simulation runs, $n = 20$, $p = 22$, $\theta_{truth} = 25°$. Point cloud has a higher variance along the vehicle's longitudinal axis.

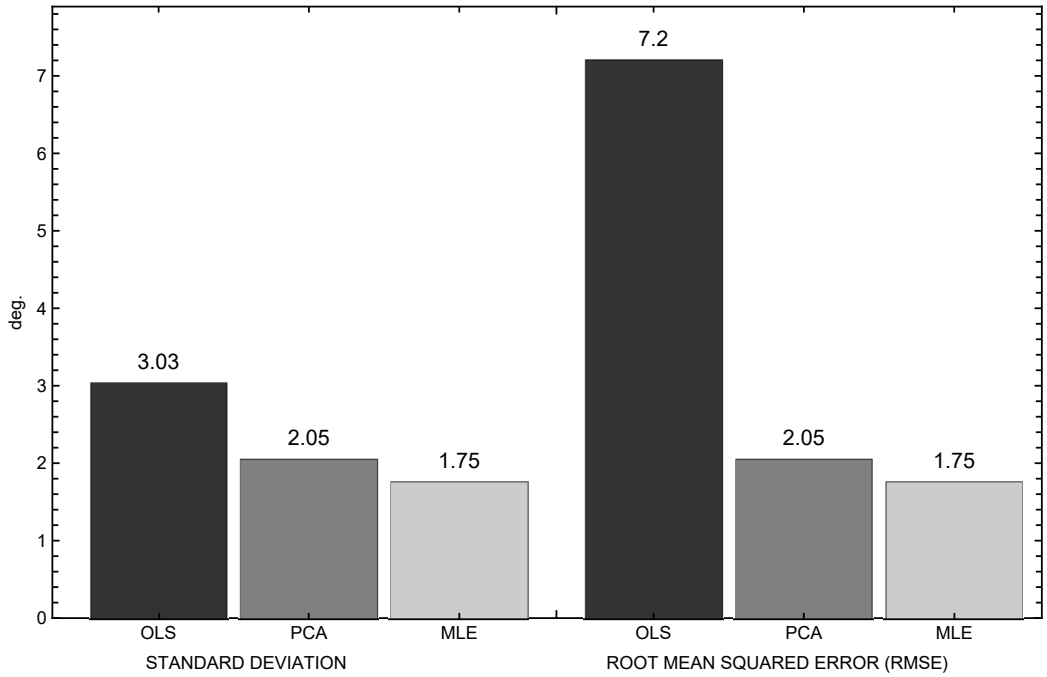

Figure 2.12: Estimation deviations for the simulation presented in Fig. 2.11.

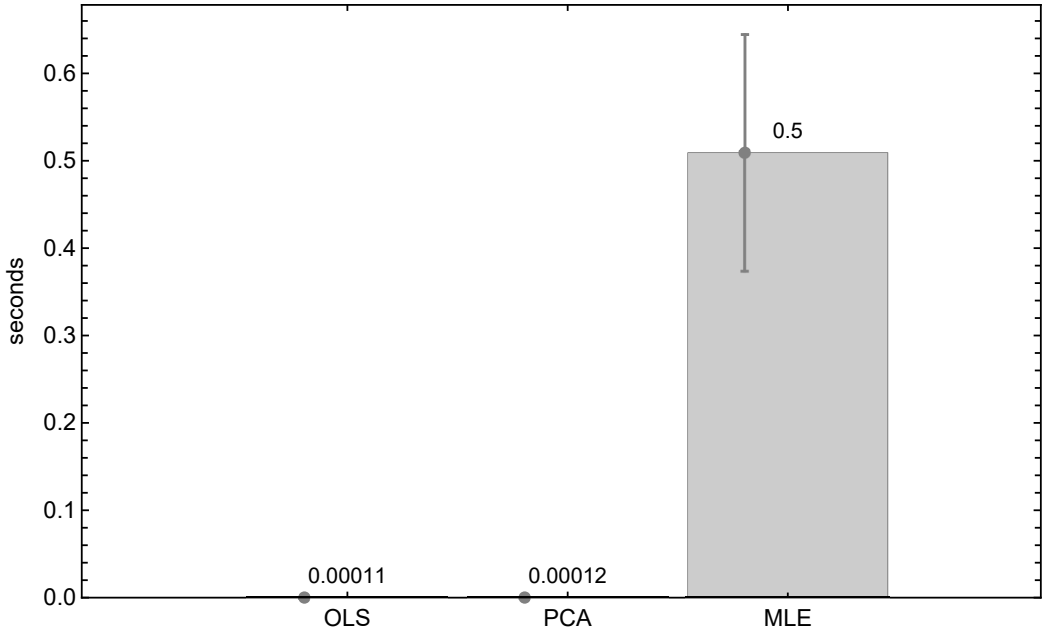

Figure 2.13: Computation time averaged over 1000 runs, $n = 20,\ p = 22$.

2.6.2 Computational Cost Analysis

The simulation was implemented with Wolfram's Mathematica [14] on a 2.50GHz CPU, 12GB RAM computer. The likelihood in equation 2.9 was numerically maximized using Mathematica's `NMaximize[]` function with the `DifferentialEvolution` method.

Both the PCA and the MLE methods have comparable performance based on the simulation results. However, MLE's performance comes with a cost. Its major computation is spent in maximizing the likelihood such that every value of θ creates a $Q^T_{(\theta)}$ on which both $\hat{\mu}_{(\theta)}$ and $\hat{K}_{(\theta)}$ also depend. Therefore, stepping the likelihood through the range of angles requires more computational resources.

Meanwhile, computational complexity and communication bandwidth are big considerations on autonomous vehicles, which already have a large amount of data to process from other sensors. Therefore, PCA could be a candidate for implementation due to its faster computation, relative to the MLE method, without a significant reduction in performance, and non-reliance on a distribution for estimation.

2.7 Conclusion

This work presented a theory for estimating a trailer's articulation angle using the point cloud data obtained from sensors which are already at the rear of the vehicle. We simulated point clouds for one of the sensors, a radar, with a view to implementing the approach on other sensors. Three methods were presented and their simulation results shown. Importantly, the methods neither introduced additional hardware nor stickers for the estimation.

Chapter 3

Trailer Angle Detection Using Radar Point Clouds

3.1 Chapter abstract

Algorithms for trailer control and backup need to keep track of the trailer angle, also known as the hitch angle, and therefore the angle needs to be determined. In this work, we estimate the angle using 2D point clouds collected from two automotive radars installed in the tail light fixtures of a truck which attaches to a trailer

The material contained in this chapter has been submitted to the IEEE Journal of Selected Topics in Signal Processing (Special Issue on Recent Advances in Automotive Radar Signal Processing). The work was supported by the Ford Motor Company as an Alliance Project under Ford/MTU Master Agreement #83437205.

at the truck's hitch ball. The detection threshold of each radar is reduced to allow more detections of the trailer and consequently, more false positives are introduced. A rotational point set registration algorithm is presented to match pairs of the radar detection sets as the trailer rotates. The objective is to differentiate the trailer detections from the false positives. Two estimation methods are provided based on the registration algorithm, one which estimates the angle relative to a zero-angle position of the trailer, and another method which introduces an additional measurement at a nonzero-angle position. Angle estimates are refined through an application of the orthogonal Procrustes algorithm and a Kalman filter. The experimental results and computational cost analysis suggest that both methods are feasible for deployment.

3.2 Introduction

The detection of trailer angle or hitch angle has been of interest to the automotive industry through the past few decades. The angle (illustrated as θ in Figure 3.1) is needed in various trailer control applications such as backing up and the prevention of trailer jackknife.

Due to this significance, multiple patents have been filed by researchers and automotive organizations, few are [5, 7, 10, 15–21]. The methods described in [5, 15, 16] require a sensing hardware to be integrated with the hitch ball in order to estimate

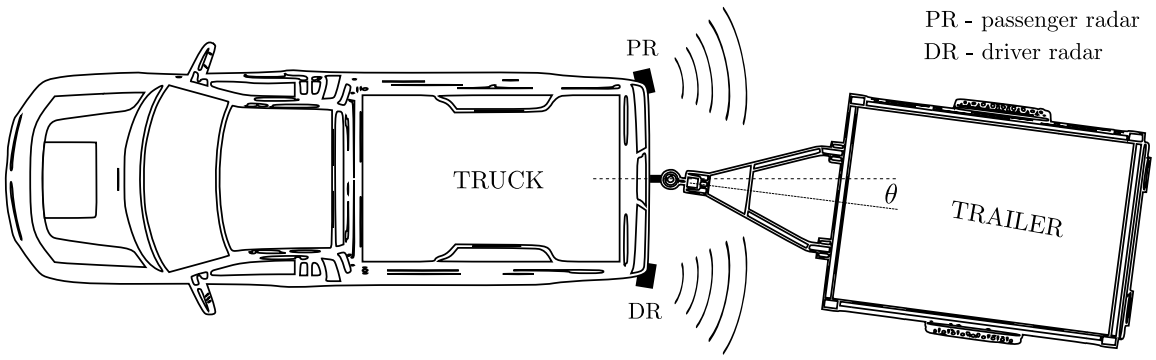

Figure 3.1: A truck and trailer diagram showing the trailer angle (or hitch angle) θ which is to be estimated.

the angle. In [17], ultrasonic sensors were installed at the vehicle rear and reflectors were placed on the trailer surface. The distances measured between the sensors and the reflectors were used to estimate the angle. A short-range communication device was installed each on the truck and trailer in [18]. Either one of the devices has its antenna spaced-apart so that the trailer angle can be determined using signal processing methods. There were also vision-based approaches. One or more cameras were installed at the vehicle rear to capture images from the trailer which were then processed to determine the angle [7, 19–21]. A special sticker was placed on the trailer in [7] to be tracked by the rear camera. In [10], existing sensors on the truck such as radar, camera, and ultrasonic sensors were combined for the estimation. However, the method requires some trailer dimensions.

This problem has also attracted the attention of researchers. In [22], the angle was estimated by comparing different templates of the trailer images captured by a camera. The method was recommended for trailers having plain fronts. In [23], a wide-angle

camera was installed at the vehicle rear. The video frames from the camera were processed to estimate the angle. The approach provided in [9, 24] used a state observer for the estimation. The observer requires some signals from different sources such as yaw rate, lateral acceleration, and wheel angle sensors. In addition to the use of signals, [24] also requires certain dimensions of the vehicle and trailer.

There are some challenges with most of the existing methods. Installing another hardware sensor on the vehicle or trailer increases the production cost of the system. It is also well known that vision-based sensing (and lidar if considered) is (are) not reliable in extreme weather conditions [3]. Also, the camera-sticker technology does not encourage easy trailer replacement when a spare sticker becomes unavailable. Hence, like in [10], we recommend estimating the angle using existing sensors installed on the vehicle, we considered radars in this work. This approach is plausible since radars perform well in extreme weather conditions [3] and because no additional sensor or sticker will be required. Also, our approach does not require the dimensions of the trailer.

This paper is arranged as follows: section 3.3 describes the problem statement and the experimental apparatus, section 3.4 gives an account of two estimation methods, estimation results from both methods are discussed in section 3.5 (with computational analysis), some more results are provided in section 3.6, and conclusion presented in section‘3.7. These are the general notations used: $\boldsymbol{a}$ in bold lower case is a column vector, A in upper case is a matrix, and ^{T} represents a transpose operation.

Figure 3.2: *Left*: The experimental apparatus consists of a trailer coupled with a truck mock-up. The inset image shows a Vernier **rotary motion sensor** installed on the hitch ball to read the ground truth, it was not used for the estimation. *Right*: The driver and passenger **radars** (encircled) installed on the sides of the truck mock-up. A rear gate **camera** (shown in square bounds) was also installed on the mock-up for trailer visualization, it was not used for the estimation.

3.3 Problem Statement and Experimental Apparatus

3.3.1 Problem Statement

Modern vehicles have blind spot information system radars installed in similar locations as the two radars illustrated in Figure 3.1. We want to estimate the trailer angle θ (shown in the figure) using only the detections obtained from both the driver radar (DR) and the passenger radar (PR). As a constraint, we like to perform the estimation without introducing a new hardware or sensor.

Table 3.1
Waveform consideration

Parameter	Value
Maximum range	$6.5m$
Range resolution	$4.1cm$
Maximum velocity	$32cm/s$
Velocity resolution	$2cm/s$

3.3.2 Experimental Apparatus

The apparatus was constructed as illustrated in Figure 3.2. The truck mock-up is simply a truck's rear gate mounted on a three-wheel platform. We simulated the trailer's rotation by actually rotating the truck mock-up instead, while the trailer was fixed in its position. This was because the platform would be displaced if the trailer rotated. Therefore, trailer rotation in this paper refers to this procedure. Two radar modules were installed on the sides of the mock-up. We used the TI AWR1642BOOST radar [25]. It has 2 transmit and 4 receive channels. There is an available bandwidth of 4GHz in the $76 - 81$GHz band. In multiple-input multiple-output (MIMO) mode, its 8 virtual array elements spaced at half-wavelength apart give a half-power transmit beamwidth of $0.25rad \approx 14.3°$ (in azimuth) at boresight. The MIMO configuration is for each radar having collocated elements. No attempt was made to synchronize the configuration on both radars. Meanwhile, the radar detections are in range, angle, and Doppler. We do not process the raw radar data.

The considerations used in designing the frequency-modulated continuous-wave (FMCW) waveform are provided in Table 3.1. We reduced the constant false alarm rate (CFAR) range detection threshold through the radar configuration file to $3dB$ to allow for more trailer detections. The waveform considerations and the detection threshold are not guaranteed to be optimal in all situations and with all radars.

We wanted to be sure that the pulses received by a radar was transmitted by the same radar. Therefore, we energized the radars sequentially (one after the other) for data collection.

3.4 Estimation Methods

3.4.1 Method 1 - Detector block and the Kalman filter

Referring to the illustration in Figure 3.3. The detector block (DB) has two point set inputs: $X_0^r \in \mathbb{R}^{2\times n}$ is the zero-degree set containing the detections obtained when the trailer is directly behind the truck and $Y^r \in \mathbb{R}^{2\times m}$ is the set containing the detections obtained after trailer rotation. Both are in radar coordinates. The truck can be driven in a straight line to obtain X_0^r. The following describes the three modules in DB and the Kalman filter.

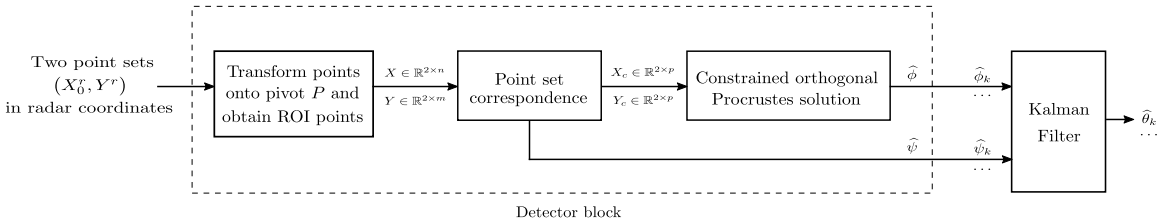

Figure 3.3: Method 1 - Detector block and the Kalman filter.

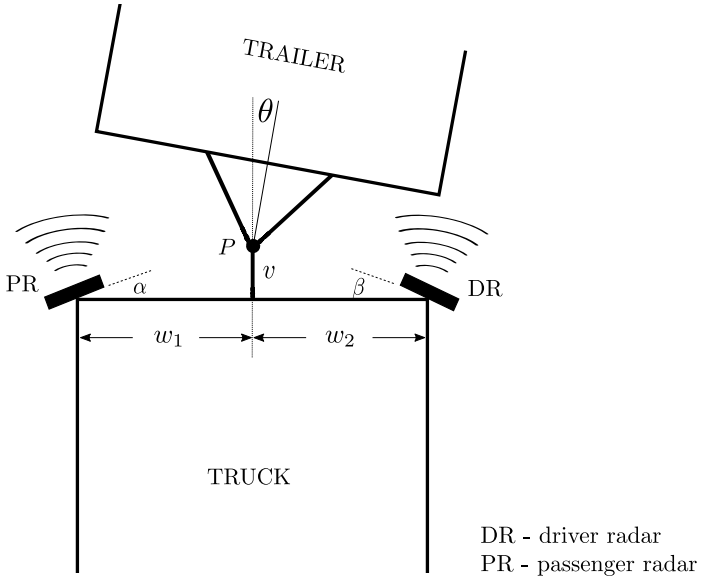

Figure 3.4: A schematic diagram of the truck and trailer illustrated in Figure 3.1. The trailer rotates about the hitch ball (pivot P) at true angle θ with respect to the zero-degree position. The parameters α and β are the radar installation angles, w_1 and w_2 are the lateral distances from the truck center to PR and DR respectively, and v is the perpendicular distance from the hitch ball to the lateral line connecting the radars.

3.4.1.1 Transform points onto pivot P and obtain ROI points

The trailer rotates about the hitch ball (pivot P). Therefore, let us transform the radar detections onto a common Cartesian coordinate having its origin at P. Let

$$Q_{(\alpha)} = \begin{bmatrix} \cos(\alpha) & -\sin(\alpha) \\ \sin(\alpha) & \cos(\alpha) \end{bmatrix}$$

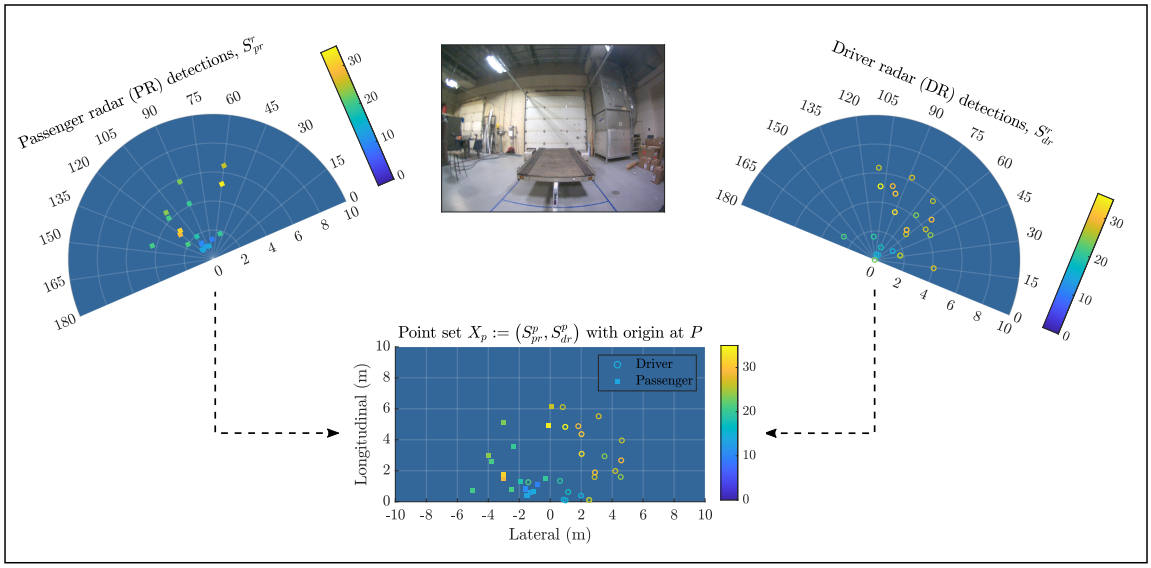

Figure 3.5: Data collection **before trailer rotates** i.e. at the zero-degree trailer angle. Both radar detections are transformed onto a common Cartesian coordinate having its origin on the hitch ball (pivot P). The color bars indicate signal strengths of the detections. The image shows the trailer, it is not used for the estimation.

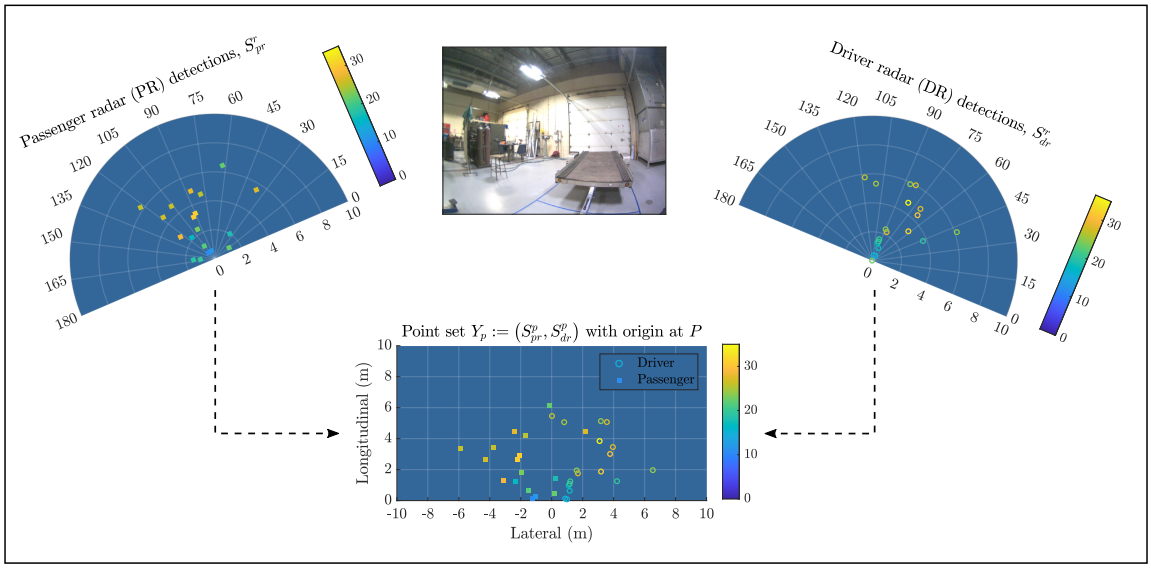

Figure 3.6: Data collection **after trailer rotates**. Both radar detections are transformed onto a common Cartesian coordinate having its origin on the hitch ball (pivot P). The color bars indicate signal strengths of the detections. The image shows the rotated trailer, it is not used for the estimation.

be a rotation matrix at an angle α (rotating a vector counter-clockwisely if α is positive), $\mathcal{S}_{pr}^{r}$ and $\mathcal{S}_{dr}^{r}$ respectively be the PR and DR detections represented in range-azimuth coordinates, $\mathcal{S}_{pr}^{p}$ and $\mathcal{S}_{dr}^{p}$ be the transformed PR and DR detections onto the common Cartesian coordinate at origin P, and $\mathbf{1}$ be the column vector of 1's of an appropriate size. The rotation and translation parameters (α, β, w_1, and v) used in equations (3.1) and (3.2) are described in Figure 3.4. The detections are transformed onto pivot P as follows:

$$\mathcal{S}_{pr}^{p} = Q_{(\alpha)}\acute{\mathcal{S}}_{pr}^{r} - \begin{bmatrix} w_1 \\ \\ v \end{bmatrix} \mathbf{1}^T \tag{3.1}$$

$$\mathcal{S}_{dr}^{p} = Q_{(\beta)}^{T}\acute{\mathcal{S}}_{dr}^{r} - \begin{bmatrix} -w_2 \\ \\ v \end{bmatrix} \mathbf{1}^T \tag{3.2}$$

where $\acute{\mathcal{S}}_{pr}^{r}$ and $\acute{\mathcal{S}}_{dr}^{r}$ are the Cartesian coordinate representations of $\mathcal{S}_{pr}^{r}$ and $\mathcal{S}_{dr}^{r}$ respectively. The transformations in (3.1) and (3.2) will be performed in two instances: for the detections obtained before trailer rotates (i.e. the trailer lies at the zero-degree position) and for those obtained after trailer rotates.

Before trailer rotates: If the radar data was collected when the trailer was directly behind the truck i.e. at the zero-degree position, then the detections before transformation make the zero-degree point set, $X_0^r \coloneqq \left(\acute{\mathcal{S}}_{pr}^{r}, \acute{\mathcal{S}}_{dr}^{r}\right)$. This is the first input set to Method 1 as described in Figure 3.3. An illustration of the transformed detections

$X^p \coloneqq \left(\mathcal{S}^p_{pr}, \mathcal{S}^p_{dr}\right)$ having origin at P is provided in Figure 3.5.

After trailer rotates: Likewise, if the radar data was collected after trailer rotates, then the detections before transformation make the after-rotation point set, $Y^r \coloneqq \left(\acute{\mathcal{S}}^r_{pr}, \acute{\mathcal{S}}^r_{dr}\right)$. This is the second input set to Method 1 as described in Figure 3.3. The transformed set of detections $Y^p \coloneqq \left(\mathcal{S}^p_{pr}, \mathcal{S}^p_{dr}\right)$ having origin at P is illustrated in Figure 3.6.

It is necessary to only process the detections found within an area in which the trailer can be found and discard the obvious non-trailer detections. Hence, we define a region of interest (ROI) as the space in which the trailer occupies. The ROI used in this work is the space within ranges $\big[1, 4\big]m$ of the hitch ball (pivot P). This was chosen based on the form of the trailer used in this work. The points in the after-transformation sets X^p and Y^p (both having origin at P) are then checked for existence in the ROI. For each set, let the detections found within the ROI be passed to the output of the module for further processing, $X^p \rightarrow X$ and $Y^p \rightarrow Y$. The output sets $X \in \mathbb{R}^{2\times n}$ and $Y \in \mathbb{R}^{2\times m}$ respectively contain the detections found within the ROI before and after the trailer rotates. They will be processed to estimate the trailer angle.

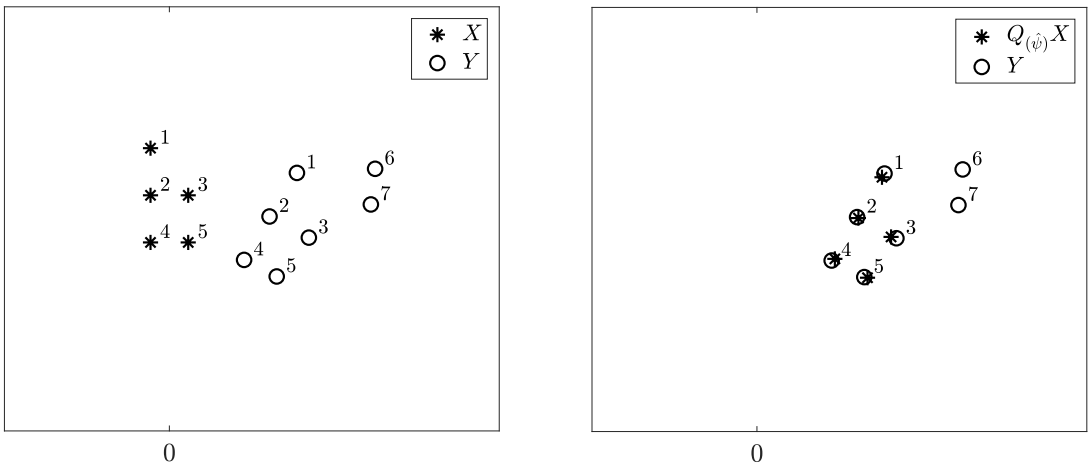

Figure 3.7: An illustration of the **rotational point set registration** with a minimal example. *Left*: Take sets X and Y as the trailer detections at the zero-degree angle and after rotation respectively where points 6 and 7 are extra detections after rotation. *Right*: Search for angle $\widehat{\psi}$ which aligns $Q_{(\widehat{\psi})}X$ and Y. The corresponding pairs $1, 2, 3, 4$, and 5 are obtained using the condition in (3.4).

3.4.1.2 Point set correspondence

This is a major component of the detector block. The basic operating principle used in this work is in the reduction of the radar threshold to obtain more detections of scatterers from the trailer. Consequently, this increases the false positives. Meanwhile, the true trailer detections are persistent while the false positives are not. The idea then is to identify the persistent detections across different point sets. Hence, estimating the trailer angle reduces to finding the rotational transformation of the persistent detections in the sets X and Y. This is equivalent to finding the corresponding points in both sets through point set registration methods, a review of the literature is provided in [26].

We obtain the corresponding points from $X = \left(\boldsymbol{x}_i\right)_{i=1}^{n}$ and $Y = \left(\boldsymbol{y}_j\right)_{j=1}^{m}$ by using the rotational point set registration given in Algorithm 4 and illustrated with a minimal example in Figure 3.7. We did not consider the signal strengths of the detections in the registration algorithm because the signal strengths vary considerably with rotation. The algorithm was motivated by the iterative closest point (ICP) [27]. The ICP considers both rotation and translation parameters while Algorithm 4 only considers rotation because the trailer is constrained for rotational motion only.

Algorithm 4 Rotational point set registration

1: **function** CORRESPONDENCE($X, Y, searchRange, r$)
2: Search for angle $\widehat{\psi}$ as in (3.3)
▷ We used coarse-to-fine search in ***searchRange*** over 5 divisions
3: Obtain corresponding sets X_c and Y_c based on (3.4)
4: **return** $\widehat{\psi}$, X_c, Y_c
5: **end function**

The steps in Algorithm 4 are described as follows. The algorithm searches for a rotation angle $\widehat{\psi}$ which aligns $Q_{(\widehat{\psi})}X$ and Y.

$$\widehat{\psi} = \underset{\psi}{\operatorname{argmin}} \sum_{i=1}^{n} d\big(Q_{(\psi)}\boldsymbol{x}_i, \boldsymbol{y}_{nearest}\big) \tag{3.3}$$

where $d(.)$ is a choice distance function, and $\boldsymbol{y}_{nearest} \in Y$ is the nearest neighbor to $Q_{(\psi)}\boldsymbol{x}_i$ with respect to the distance function. We used the Euclidean distance metric in this work. Therefore, $d(\boldsymbol{x}, \boldsymbol{y}) \coloneqq \|\boldsymbol{x} - \boldsymbol{y}\|$ where $\|.\|$ is the 2-norm. The search is conducted within the angle bounds provided in *searchRange*. We used the coarse-to-fine search approach to achieve (3.3) by first splitting *searchRange* coarsely into

a number of divisions (we chose 5 divisions). We further split the division where the minimum exists and iterate into finer divisions until convergence.

After obtaining angle $\widehat{\psi}$, we proceed to match the corresponding points in the aligned sets $\big(Q_{(\widehat{\psi})}X,\ Y\big)$. Alignment here does not interpret complete overlapping of the points since the detections are noisy and quantized in space (illustrated in Figure 3.7). The registration algorithm assumes that two points matched for correspondence represent the detections from closely-located scatterers on the trailer before and after trailer rotation. The amount of closeness between the scatterers is defined in (3.4) as a basis for correspondence matching.

Let $\boldsymbol{y}_{closest} \in Y$ be the nearest neighbor to the rotated point $Q_{(\widehat{\psi})}\boldsymbol{x}_i$. Use the condition,

$$d\big(Q_{(\widehat{\psi})}\boldsymbol{x}_i,\ \boldsymbol{y}_{closest}\big) \leq r \tag{3.4}$$

to match $\big(\boldsymbol{x}_i,\ \boldsymbol{y}_{closest}\big)$ as a pair of corresponding points, where r is the radius or scatterer closeness parameter defined by the user. If a point in Y is paired in more than one instance, keep the pair of points that has the least distance metric. This ensures a one-to-one mapping. Save each point in the matched pair respectively in X_c and Y_c such that the ith points in X_c and Y_c have correspondence. Hence, if there are p unique matches, the output corresponding sets have the same size $X_c, Y_c \in \mathbb{R}^{2\times p}$.

3.4.1.3 Constrained orthogonal Procrustes solution

Distance-based point set registration methods often require a least squares refinement of a transformation which was initially obtained for the purpose of finding the pairs of points that have correspondence [26]. We implement the same concept by solving for a least squares refinement of the search angle $\widehat{\psi}$ obtained in (3.3) in the Euclidean distance sense, with which the corresponding sets X_c and Y_c were found.

Therefore, we are interested in the best rotational transformation from X_c to Y_c in the least squares sense to obtain angle $\widehat{\phi}$. The problem is formulated as follows:

$$\widehat{\phi} = \underset{\phi}{\operatorname{argmin}} \|Q_{(\phi)} X_c - Y_c\|_F$$

subject to

$$Q_{(\phi)}^T Q_{(\phi)} = I, \ \det\left(Q_{(\phi)}\right) = +1$$

where $\|.\|_F$ is the Frobenius norm. The constraints ensure that the rotation matrix $Q_{(\widehat{\phi})}$ does not include reflection. This is the constrained orthogonal Procrustes problem [28][29]. The solution, which is based on the singular value decomposition (SVD) of $Y_c X_c^T \in \mathbb{R}^{2\times 2}$, is presented in Algorithm 5.

Algorithm 5 Constrained orthogonal Procrustes solution

function CoProcrustesAngle(X_c, Y_c)
  $W\Sigma V^T \leftarrow \text{SVD}(Y_c X_c^T)$
    ▷ Let the singular values in Σ be arranged in descending order
  $Q_{(\widehat{\phi})} \leftarrow W \begin{bmatrix} 1 & 0 \\ 0 & \det(WV^T) \end{bmatrix} V^T$
    ▷ The diagonal matrix ensures the determinant $\det\left(Q_{(\widehat{\phi})}\right) = +1$
  Obtain angle $\widehat{\phi}$ from the 2×2 rotation matrix $Q_{(\widehat{\phi})}$
  return $\widehat{\phi}$
end function

Trailer tracking

We track the trailer in motion to narrow down the correspondence search region used for the procedure in (3.3) and to prevent possible minimums outside the region. In this experiment, the trailer was initialized directly behind the truck (i.e. at the zero-degree position) before being rotated. Take subscript k as the time step. Let us define the vector of angle search range, passed to Algorithm 4, as follows:

$$searchRange \coloneqq \big[-\delta,\ \delta\big], \quad \text{for } k = 1 \tag{3.5}$$

$$searchRange \coloneqq \big[\widehat{\phi}_{k-1} - \delta,\ \widehat{\phi}_{k-1} + \delta\big], \quad \text{for } k > 1 \tag{3.6}$$

where $\widehat{\phi}_{k-1}$ is the most recent orthogonal Procrustes observation. We choose to perform the tracking with respect to the Procrustes angle $\widehat{\phi}$ because it is a least squares refinement of $\widehat{\psi}$. The angle parameter δ is defined by the user. The parameter should be chosen based on the dynamics of the trailer rotation. For instance, backing

up applications may consider a small value since the trailer is not swinging rapidly. A small value can be seen as a measure of confidence that the trailer angle is really within the range. However, setting the value too small will result in the propagation of error. We varied δ in the results section.

3.4.1.4 Kalman filter (for Method 1)

Here, we use the Kalman filter to smooth the two angle estimates $\widehat{\phi}$ and $\widehat{\psi}$ over time. The angles will be referred to as observations. The filter, a well known tool, estimates the state of a system using noisy observations recorded over time with respect to the system's dynamics (in this case the trailer's rotation). The observation errors are assumed to be Gaussian. We used the constant angular acceleration motion model of the form,

$$\varphi = \varphi_0 + \dot{\varphi}_0 \Delta T + \frac{1}{2} a (\Delta T)^2 \tag{3.7}$$

$$\dot{\varphi} = \dot{\varphi}_0 + a \Delta T \tag{3.8}$$

where φ_0 and $\dot{\varphi}_0$ are respectively the initial angular displacement and velocity, φ and $\dot{\varphi}$ are respectively the angular displacement and velocity after the time interval ΔT, and a is the constant angular acceleration through the time interval.

Define a two-element state vector as $\boldsymbol{\varphi} \coloneqq \begin{bmatrix} \varphi \\ \dot{\varphi} \end{bmatrix}$ for the angular displacement and velocity quantities. From (3.7) and (3.8), the linear time-invariant discrete state-space model is given as:

$$\boldsymbol{\varphi}_k = A\boldsymbol{\varphi}_{k-1} + Ga_{k-1} \tag{3.9}$$

$$\boldsymbol{y}_k = C\boldsymbol{\varphi}_k + \boldsymbol{v}_k \tag{3.10}$$

where

$$A = \begin{bmatrix} 1 & \Delta T \\ 0 & 1 \end{bmatrix},\ G = \begin{bmatrix} \frac{1}{2}(\Delta T)^2 \\ \Delta T \end{bmatrix},\ \boldsymbol{y}_k = \begin{bmatrix} \widehat{\phi}_k \\ \widehat{\psi}_k \end{bmatrix},\ C = \begin{bmatrix} 1 & 0 \\ 1 & 0 \end{bmatrix}$$

with (3.9) as the state transition equation and (3.10) as the measurement equation. The system is observable since the observability matrix $\begin{bmatrix} C \\ CA \end{bmatrix}$ is full-ranked, at $\Delta T \neq 0$.

Without a control input, Ga_{k-1} is modeled as the process noise. The acceleration term $a_{k-1} \sim \mathcal{N}(0, \sigma_{k-1}^2)$ so that the covariance matrix $Q_{k-1} \coloneqq \mathrm{cov}(Ga_{k-1})$ is given as

$$Q_{k-1} = GG^T\sigma_{k-1}^2 = \begin{bmatrix} \frac{1}{4}(\Delta T)^4 & \frac{1}{2}(\Delta T)^3 \\ \frac{1}{2}(\Delta T)^3 & (\Delta T)^2 \end{bmatrix}\sigma_{k-1}^2 \tag{3.11}$$

Similarly, the measurement noise $\boldsymbol{v}_k \sim \mathcal{N}(0, R_k)$. We set the variance of the acceleration term in (3.11) as $\sigma_{k-1}^2 = 1(deg/s^2)^2$ to obtain Q_{k-1} , $\forall k$ and estimated R_k directly from the observations using a similar [1]heuristic method described in [30].

Let $\widehat{\boldsymbol{\varphi}}_{k|k-1}$ denote the predicted state at time step k without including the measurement at k and $P_{k|k-1}$ be the corresponding state covariance. Also, let $\widehat{\boldsymbol{\varphi}}_{k|k}$ denote the estimated state at time step k including the measurement at k and $P_{k|k}$ be the corresponding state covariance.

The trailer was kept stationary directly behind the truck (the zero-degree position) at the initialization stage. Thus, we initialized the state distribution as

$$\widehat{\boldsymbol{\varphi}}_{0|0} = \begin{bmatrix} 0 \\ \\ 0 \end{bmatrix}, \quad P_{0|0} = \begin{bmatrix} 0.01 & 1 \\ \\ 1 & 0.01 \end{bmatrix}.$$

The diagonals of $P_{0|0}$ show a high confidence about the initialized state while keeping the matrix positive definite. The two steps of the filter are given below with equations for time step $k \geq 1$:

(a) Prediction step (a-priori):

$$\widehat{\boldsymbol{\varphi}}_{k|k-1} = A\widehat{\boldsymbol{\varphi}}_{k-1|k-1}$$

$$P_{k|k-1} = AP_{k-1|k-1}A^T + Q_{k-1}$$

[1]We used the exponential moving average smoothing, one of the options provided in [30].

(b) Update step (a-posteriori):

$$\boldsymbol{g}_k = \boldsymbol{y}_k - C\widehat{\boldsymbol{\varphi}}_{k|k-1}$$

$$S_k = CP_{k|k-1}C^T + R_k$$

$$K_k = P_{k|k-1}C^T S_k^{-1}$$

$$\widehat{\boldsymbol{\varphi}}_{k|k} = \widehat{\boldsymbol{\varphi}}_{k|k-1} + K_k\boldsymbol{g}_k$$

$$P_{k|k} = (I - K_kC)P_{k|k-1}$$

where $\widehat{\boldsymbol{\varphi}}_{k|k-1}$ and $P_{k|k-1}$ are the prior state estimate and covariance respectively, $\boldsymbol{g}_k$ is the innovation, S_k is the innovation covariance, K_k is the Kalman gain, $\widehat{\boldsymbol{\varphi}}_{k|k}$ and $P_{k|k}$ are the posterior state estimate and covariance respectively.

The kth Kalman filter output is

$$\widehat{\theta}_k \coloneqq \begin{bmatrix}1 & 0\end{bmatrix}\widehat{\boldsymbol{\varphi}}_{k|k} \ .$$

The vector of estimation results $\widehat{\boldsymbol{\theta}} = \left(\widehat{\theta}_k\right)_{\forall k}$ will be presented in section 3.5.

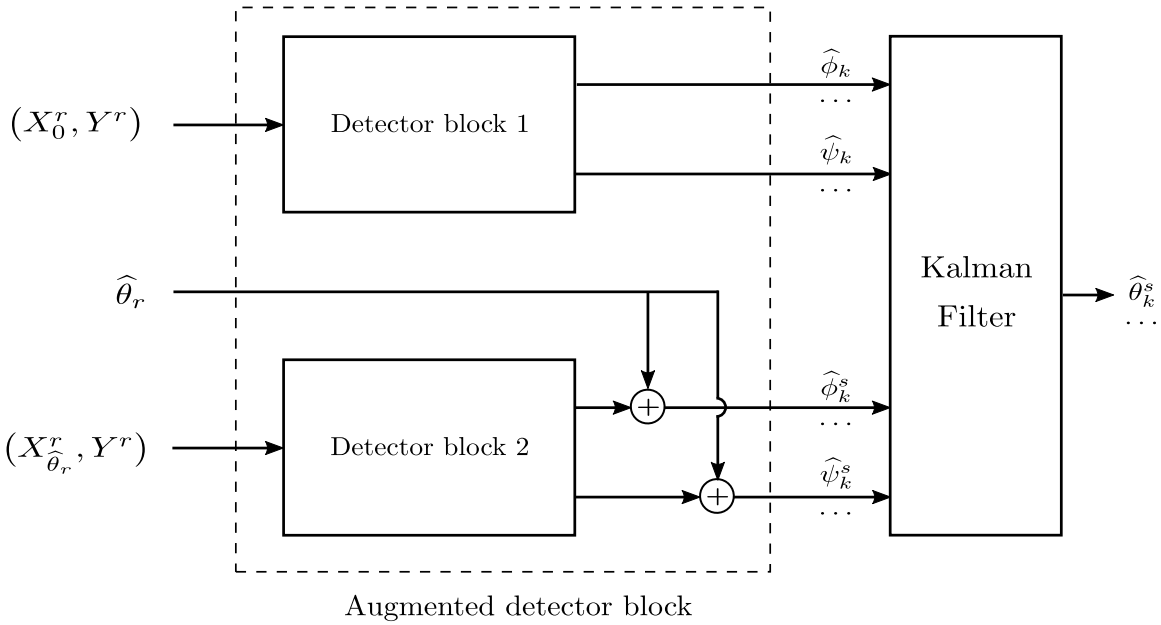

Figure 3.8: Method 2 - Augmented detector block and the Kalman filter.

3.4.2 Method 2 - Augmented detector block and the Kalman filter

Let us refer to a 'reference set' as the set to which the after-rotation set Y^r is being compared for rotation estimation. Method 1 has X_0^r as the zero-degree reference set. The set Y^r is always compared with X_0^r. This is too much reliance on X_0^r. The method has one pair of input sets $\left(X_0^r, Y^r\right)$.

This method, illustrated in Figure 3.8, introduces another $\widehat{\theta}_r$-degree reference set $X_{\widehat{\theta}_r}^r$ which will be learnt online. The set Y^r will be compared with two reference sets X_0^r and $X_{\widehat{\theta}_r}^r$. This reduces the reliance on X_0^r. The method will have two pairs of input

sets $\left(X_0^r, Y^r\right)$ and $\left(X_{\widehat{\theta}_r}^r, Y^r\right)$ for the estimation.

The following gives a description of the augmented detector block and the Kalman filter, contained in this method.

3.4.2.1 Augmented detector block

This has two detector blocks, DB 1 and DB 2. Each is a duplicate of DB from Method 1. Let us define the following functions for DB 1 and DB 2 respectively:

$$\left[\widehat{\phi}_k, \widehat{\psi}_k\right] \coloneqq \textsc{ExecuteDB1}\left(X_0^r, Y^r\right) \tag{3.12}$$

$$\left[\widehat{\phi}_k^s, \widehat{\psi}_k^s\right] \coloneqq \textsc{ExecuteDB2withShift}\left(X_{\widehat{\theta}_r}^r, Y^r, \widehat{\theta}_r\right) \tag{3.13}$$

where ExecuteDB1 returns the observations $\widehat{\phi}_k$ and $\widehat{\psi}_k$, and ExecuteDB2withShift returns the shifted observations $\widehat{\phi}_k^s$ and $\widehat{\psi}_k^s$. Both functions will be called from Algorithm 6.

The after-rotation set Y^r is common to both detector blocks but their reference sets differ, X_0^r is for DB 1 and $X_{\widehat{\theta}_r}^r$ is for DB 2. Unlike DB 1, the outputs of DB 2 are not relative to the zero-degree angle, but to the reference angle $\widehat{\theta}_r$. Hence, we add $\widehat{\theta}_r$ to the outputs to make observations $\widehat{\phi}_k^s$ and $\widehat{\psi}_k^s$, where $\widehat{\phi}_k^s$ is the *shifted* orthogonal Procrustes angle and $\widehat{\psi}_k^s$ is the *shifted* correspondence search angle. Together with

the two DB 1 observations, there are four observations passed to the Kalman filter.

Executing Method 2

The steps are provided in the METHOD2 procedure (Algorithm 6). The procedure keeps a library *RefLib* of reference angles and their associated sets, in which a candidate gets selected. The library is initialized with the zero-degree reference angle and its set X_0^r. For each time step k, we run DB 1 and DB 2 in lines 6 and 7. The resulting four observations are passed to the Kalman filter to obtain the trailer angle estimate $\widehat{\theta}_k^s$. The library needs to be updated. We append the angle $\widehat{\theta}_r \coloneqq \widehat{\theta}_k^s$ and the after-rotation set $X_{\widehat{\theta}_r}^r \coloneqq Y^r$ in paired association to the library if $\widehat{\theta}_k^s$ is approximately a multiple of an angle interval parameter $\theta_{interval}$. A way to identify when this occurs is to keep track of the absolute difference of two moduli $\mod\left(\widehat{\theta}_{k-1}^s, \theta_{interval}\right)$ and $\mod\left(\widehat{\theta}_k^s, \theta_{interval}\right)$, there will be a spike to signify the occurrence. This can be interpreted as sampling the estimates around the multiples of $\theta_{interval}$. For example, if $\theta_{interval} = 5°$, the library will be updated when $\widehat{\theta}_k^s \approx \left(0°, \pm 5°, \pm 10°, \dots\right)$.

Running detector block 2 and learning $X_{\widehat{\theta}_r}^r$ online

The zero-degree reference set X_0^r can be obtained by driving the truck in a straight line. However, we do not expect a prior knowledge of the $\widehat{\theta}_r$-degree reference sets.

Algorithm 6 Procedure to execute Method 2

procedure METHOD2
▷ Define parameters and initialize library of reference sets and angles
  Set $\theta_{difference}$ and $\theta_{interval}$
  $RefLib.angle = \{0\}$
  $RefLib.set = \{X_0^r\}$
  for each k time step **do**
    $[\widehat{\phi}_k, \widehat{\psi}_k] =$ EXECUTEDB1(X_0^r, Y^r) ▷ Referring to (3.12)
    $[\widehat{\phi}_k^s, \widehat{\psi}_k^s] =$ DB2ONLINE$(RefLib, Y^r, \widehat{\phi}_k, \widehat{\theta}_{k-1}^s, \theta_{difference})$
    ▷ The **function** is provided below
    $\widehat{\theta}_k^s \leftarrow \mathcal{K}_{(\widehat{\phi}_k, \widehat{\psi}_k, \widehat{\phi}_k^s, \widehat{\psi}_k^s)}$
    save estimate $\widehat{\theta}_k^s$
    ▷ Add new reference angle and set to the libary
    if $\widehat{\theta}_k^s$ is approximately a multiple of $\theta_{interval}$ **then**
      append $\widehat{\theta}_r := \widehat{\theta}_k^s$ to $RefLib.angle$
      append $X_{\widehat{\theta}_r}^r := Y^r$ to $RefLib.set$
    end if
  end for
end procedure

function DB2ONLINE$(RefLib, Y^r, \widehat{\phi}_k, \widehat{\theta}_{k-1}^s, \theta_{difference})$
  $anglesRejected = \{\}$
  while 1 **do**
    $angleList \leftarrow RefLib.angle - anglesRejected$
    ▷ Seek candidate reference angle and set
    $\widehat{\theta}_r \leftarrow$ nearest in $angleList$ to $\widehat{\theta}_{k-1}^s$
    $X_{\widehat{\theta}_r}^r \leftarrow$ set in $RefLib.set$ associated with $\widehat{\theta}_r$
    $[\widetilde{\phi}_k^s, \widetilde{\psi}_k^s] =$ EXECUTEDB2WITHSHIFT$\big(X_{\widehat{\theta}_r}^r, Y^r, \widehat{\theta}_r\big)$
    ▷ Referring to (3.13)
    if $|\widehat{\phi}_k - \widetilde{\phi}_k^s| \le \theta_{difference}$ or $\widehat{\theta}_r = 0°$ **then**
      ▷ Accept the candidate reference angle $\widehat{\theta}_r$ and its set $X_{\widehat{\theta}_r}^r$
      $\widehat{\phi}_k^s \leftarrow \widetilde{\phi}_k^s$
      $\widehat{\psi}_k^s \leftarrow \widetilde{\psi}_k^s$
      break ▷ Exit the **while** loop
    else
      ▷ Reject the candidate reference angle $\widehat{\theta}_r$ and its set $X_{\widehat{\theta}_r}^r$
      append $\widehat{\theta}_r$ to $anglesRejected$
    end if
  end while
  return $\widehat{\phi}_k^s$, $\widehat{\psi}_k^s$ ▷ Shifted observations from DB 2
end function

Therefore, we need to learn $X^r_{\widehat{\theta}_r}$ online. The online learning steps are given in the DB2ONLINE function (Algorithm 6). The function's objective is to select a candidate from the library *RefLib*. We want the candidate reference angle (through which the reference set will be selected) to be nearest to the most recent trailer angle estimate $\widehat{\theta}^s_{k-1}$ (line 5). This is because we expect more corresponding points at small angles. The function proceeds to execute DB 2 with respect to the candidate reference angle and its associated set to obtain candidate observations (line 7). The observations will either be accepted or rejected. The condition for acceptance is either that the absolute difference of the Procrustes angle from DB 1 and the candidate Procrustes angle from DB 2 is within a threshold $\theta_{difference}$ (the Procrustes solutions give the best possible rotations in least squares terms [29]) or that the zero-degree reference angle is the candidate (line 8). Note that the *reference set shifting* is prone to error accumulation since the reference angle $\widehat{\theta}_r$ is an estimate of the underlying true value. However, the comparison of the Procrustes estimates from both detector blocks using the parameter $\theta_{difference}$ mitigates the error accumulation effect. Upon acceptance, the two observations $\widehat{\phi}^s_k$ and $\widehat{\psi}^s_k$ are returned to the main procedure in Algorithm 6. If the observations are rejected, we append the candidate reference angle to the list of rejected angles and run the loop again. In the worst case of rejecting multiple candidates, the algorithm reverts to the zero-degree reference angle and its associated set such that DB 2 becomes DB 1.

Trailer tracking in Method 2

The angle search range used by the point set correspondence module while executing DB 1 (line 6 of METHOD2 in Algorithm 6) is the same as that defined in (3.5) and (3.6). However, the search range used by the correspondence module while executing DB 2 (line 7 of DB2ONLINE in Algorithm 6) is defined as follows:

$$searchRange \coloneqq \big[-\delta,\ \delta\big], \quad \text{for } k = 1 \tag{3.14}$$

$$searchRange \coloneqq \big[\big(\widehat{\phi}^s_{k-1} - \widehat{\theta}_r\big) - \delta,\ \big(\widehat{\phi}^s_{k-1} - \widehat{\theta}_r\big) + \delta\big], \quad \text{for } k > 1 \tag{3.15}$$

where $\widehat{\theta}_r$ is the reference angle illustrated in Figure 3.8.

3.4.2.2 Kalman filter (for Method 2)

The filter equations described in section 3.4.1.4 remain unchanged. However, the state-space model in (3.9) and (3.10) now has four observations:

$$A = \begin{bmatrix} 1 & \Delta T \\ 0 & 1 \end{bmatrix},\ G = \begin{bmatrix} \frac{1}{2}(\Delta T)^2 \\ \Delta T \end{bmatrix},\ \boldsymbol{y}_k = \begin{bmatrix} \widehat{\phi}_k \\ \widehat{\psi}_k \\ \widehat{\phi}^s_k \\ \widehat{\psi}^s_k \end{bmatrix},\ C = \begin{bmatrix} 1 & 0 \\ 1 & 0 \\ 1 & 0 \\ 1 & 0 \end{bmatrix}$$

The kth Kalman filter output is

$$\widehat{\theta}_k^s := \begin{bmatrix} 1 & 0 \end{bmatrix} \widehat{\boldsymbol{\varphi}}_{k|k} \ .$$

The vector of estimation results $\widehat{\boldsymbol{\theta}}^s = \left(\widehat{\theta}_k^s\right)_{\forall k}$ will be presented in section 3.5.

3.5 Results and Discussion

The parameters used to transform radar detections onto the common coordinate at P (as illustrated in Figure 3.4) are $\alpha = 22.0°$, $\beta = 20.5°$, $w_1 = 0.8m$, $w_2 = 0.8m$, and $v = 0.32m$ based on our measurements. For the point set correspondence module, function $d(.)$ was the Euclidean distance and the radius/proximity parameter $r = 0.5m$. Radar data was collected at $3Hz$ and saved for post-processing. The results presented in this section are from the saved dataset. The trailer was not modified to enhance its detection (such as having corner reflectors on it).

We used the root mean square error (RMSE) to assess estimation performance.

$$RMSE_{(\tilde{\boldsymbol{\theta}})} = \sqrt{\mathbb{E}\Big[\left(\tilde{\boldsymbol{\theta}} - \boldsymbol{\theta}_{truth}\right)^T \left(\tilde{\boldsymbol{\theta}} - \boldsymbol{\theta}_{truth}\right)\Big]} \tag{3.16}$$

where $\tilde{\boldsymbol{\theta}}$ is the vector of angle estimates compared for performance and $\boldsymbol{\theta}_{truth}$ is the vector of ground truth angles obtained from the rotary motion sensor (installed on the hitch ball).

Table 3.2
Performance metric of Method 1 estimates $\widehat{\boldsymbol{\theta}}$ (in degrees)

	$\delta = 5°$	$\delta = 4°$	$\delta = 3°$	$\delta = 2°$	$\delta = 1°$
$RMSE_{(\widehat{\boldsymbol{\theta}})}$	1.15	1.12	1.05	1.08	1.26

Table 3.3
$RMSE_{(\widehat{\boldsymbol{\theta}}^s)}$ of Method 2 estimates varied by the online set learning parameters (in degrees)

		$\theta_{difference} = 1°$					$\theta_{difference} = 2°$				
		$\delta = 5°$	$\delta = 4°$	$\delta = 3°$	$\delta = 2°$	$\delta = 1°$	$\delta = 5°$	$\delta = 4°$	$\delta = 3°$	$\delta = 2°$	$\delta = 1°$
$\theta_{interval}$	5°	1.11	1.05	1.10	1.05	1.19	1.18	0.98	0.99	0.79	1.44
	6°	1.15	1.09	1.03	1.10	1.27	1.02	1.06	0.89	0.92	0.98
	7°	1.12	1.08	1.08	0.99	1.25	1.19	1.18	0.87	0.97	1.47
	8°	1.13	1.08	1.03	1.05	1.23	1.00	1.03	1.11	1.04	1.48
	9°	1.12	1.11	1.04	1.04	1.33	1.20	1.16	1.07	0.81	1.20
	10°	1.12	0.93	0.94	0.99	1.15	1.08	0.94	1.02	1.09	1.30

An increasing estimation error may be tolerated as the true angle increases. Hence, we define a hypothetical region of tolerance as

$$\pm\Big(|10\%\ \boldsymbol{\theta}_{truth}| + 0.25° \Big) \tag{3.17}$$

where 0.25° is the accuracy of the rotary motion sensor. Note that this region is only defined for visualization on the result plots, it is not used to assess estimation performance.

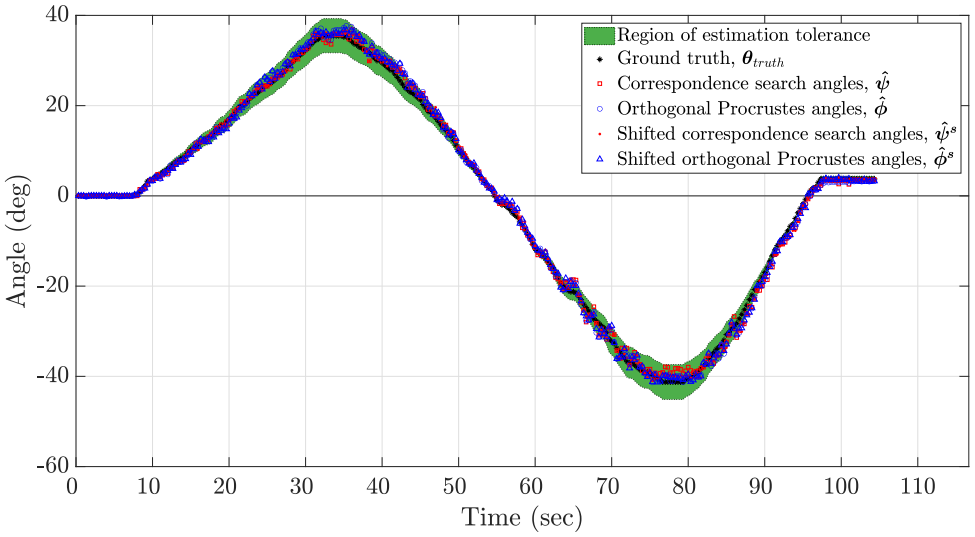

Figure 3.9: The four observations from both detector blocks (DB 1 and DB 2) in Method 2 **before Kalman filtering**. The unshifted observations, $\widehat{\boldsymbol{\psi}}$ and $\widehat{\boldsymbol{\phi}}$ are from DB 1 which are the same observations from the detector block in Method 1, $\boldsymbol{\delta = 2°}, \theta_{interval} = 5°,$ and $\theta_{difference} = 1°$.

Trailer angle estimates for both methods

Some observations **before Kalman-filtering** are shown in Figure 3.9. Subsequent plots exclude the observations for cleaner presentation. The **Kalman-filtered** (trailer angle) estimates are provided in Figures 3.10 to 3.14, varied by δ. The online set learning parameters for Method 2 were fixed at $\theta_{interval} = 5°$ and $\theta_{difference} = 1°$ in all the plots.

In addition to the plots, more results are summarized in Tables 3.2 and 3.3 with respect to the RMSE performance metric defined in (3.16). Table 3.2 (for Method 1) is varied by δ while Table 3.3 (for Method 2) varies by δ and the two set learning

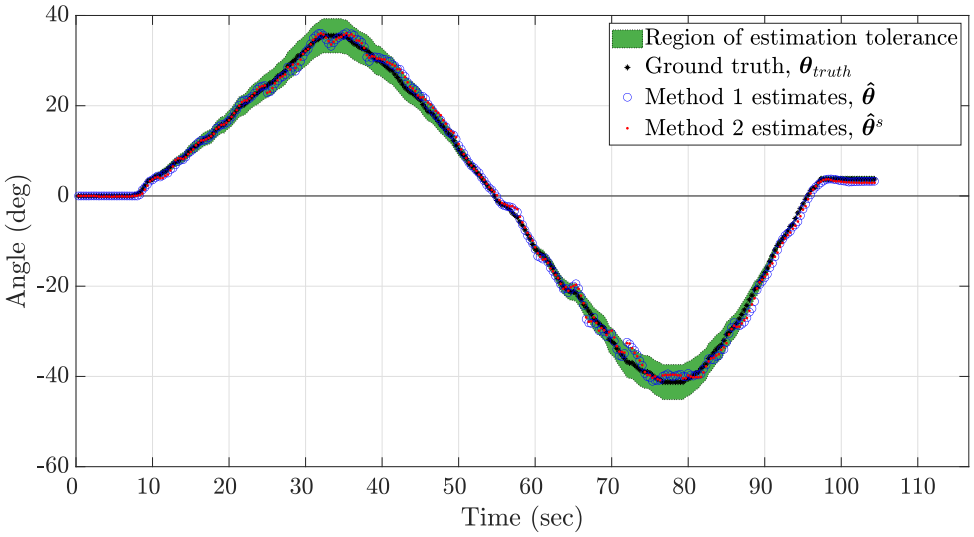

Figure 3.10: The **Kalman-filtered** estimates from both methods: Method 1 ($\boldsymbol{\delta = 5°}$) and Method 2 ($\boldsymbol{\delta = 5°}, \theta_{interval} = 5°$, and $\theta_{difference} = 1°$).

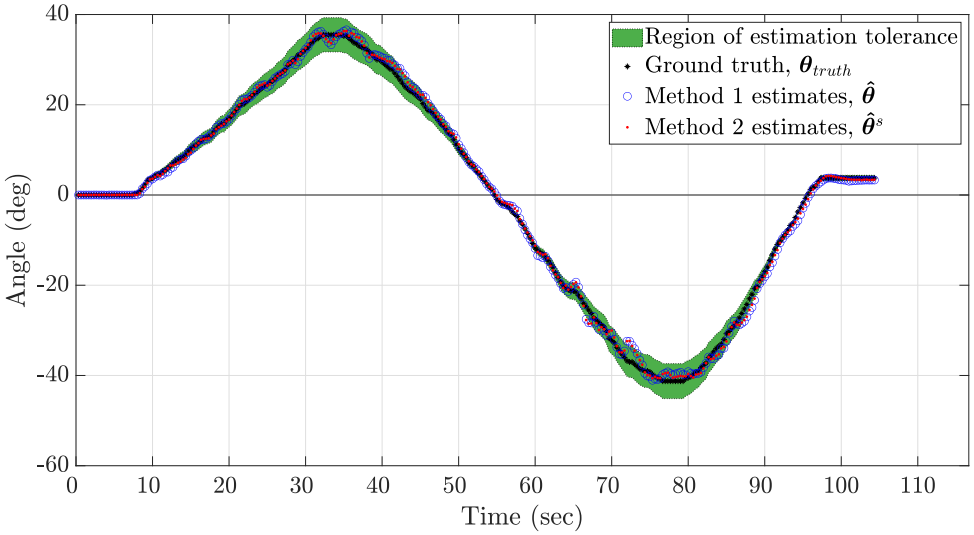

Figure 3.11: The **Kalman-filtered** estimates from both methods: Method 1 ($\boldsymbol{\delta = 4°}$) and Method 2 ($\boldsymbol{\delta = 4°}, \theta_{interval} = 5°$, and $\theta_{difference} = 1°$).

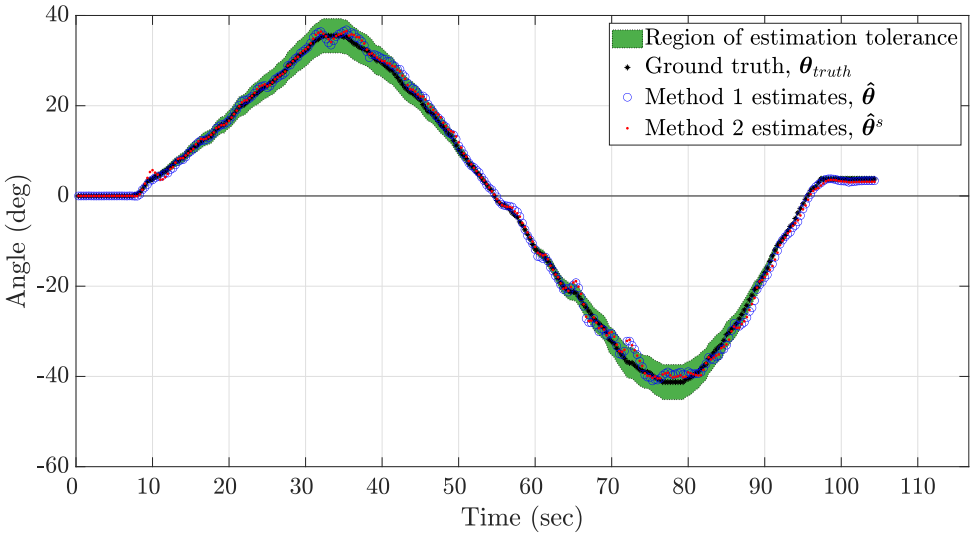

Figure 3.12: The **Kalman-filtered** estimates from both methods: Method 1 ($\boldsymbol{\delta = 3°}$) and Method 2 ($\boldsymbol{\delta = 3°}, \theta_{interval} = 5°$, and $\theta_{difference} = 1°$).

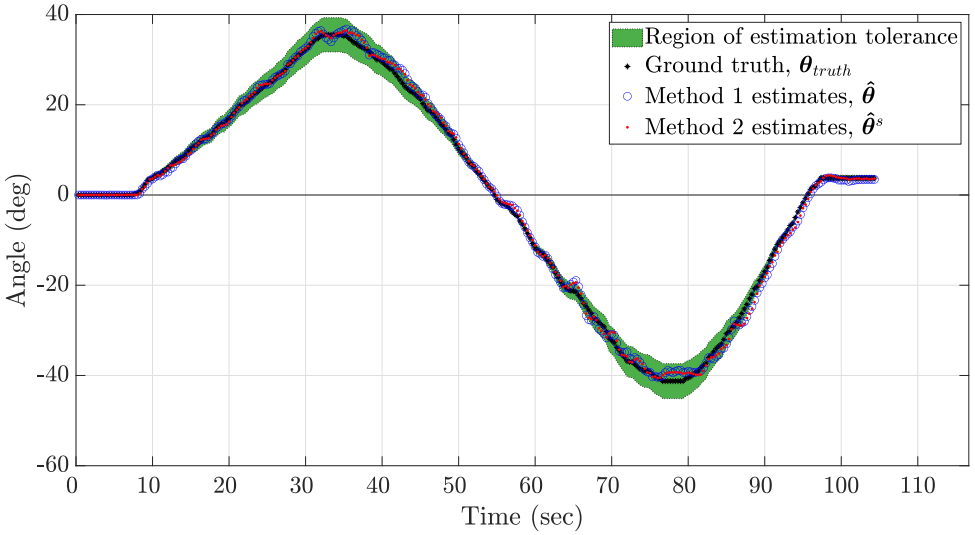

Figure 3.13: The **Kalman-filtered** estimates from both methods: Method 1 ($\boldsymbol{\delta = 2°}$) and Method 2 ($\boldsymbol{\delta = 2°}, \theta_{interval} = 5°$, and $\theta_{difference} = 1°$).

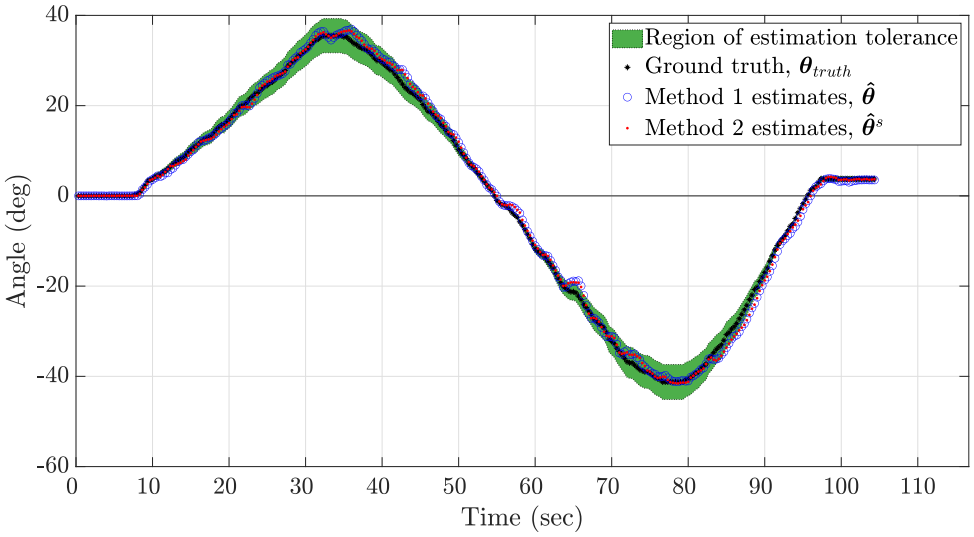

Figure 3.14: The **Kalman-filtered** estimates from both methods: Method 1 ($\boldsymbol{\delta = 1°}$) and Method 2 ($\boldsymbol{\delta = 1°}, \theta_{interval} = 5°$, and $\theta_{difference} = 1°$).

parameters $\theta_{interval}$ and $\theta_{difference}$. While the plots in Figures 3.10 to 3.14 appear to be smoother as δ reduces, we notice from the two tables that $\delta = 1°$ seems to result in error propagation suggesting that the value was set too small. The RMSE values provided in both tables are comparable. Therefore, it is not obvious which method performs better in this experiment based on the tables. However, the methods can be differentiated as discussed below.

Both methods rely on the point set correspondence module. The number of corresponding point pairs from Method 1 are indicated as (b) in Figure 3.15 (DB 1 is the same detector block used in Method 1). More point pairs seem to be matched for correspondence at lower angles, this can be seen in a time-axis comparison of the figure with any of the plots in Figures 3.10 to 3.14. This is expected because the method

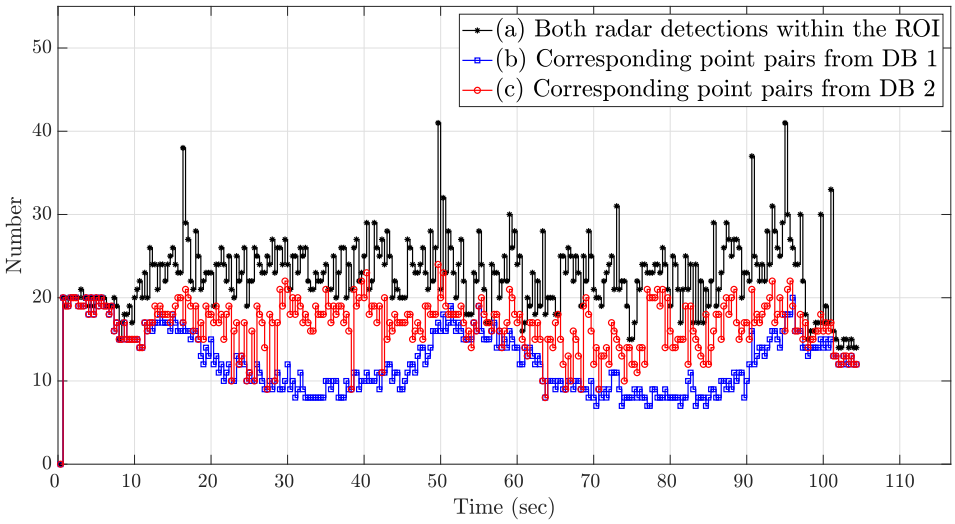

Figure 3.15: (a) The number of the combined detections from both radars found within the ROI. (b) The number of point pairs matched by the point set correspondence module in detector block 1, ($\boldsymbol{\delta = 2°}$). (c) The number of point pairs matched by the point set correspondence module in detector block 2, ($\boldsymbol{\delta = 2°}, \theta_{interval} = 5°,$ and $\theta_{difference} = 1°$).

uses the zero-degree point set for correspondence always. Therefore, lesser number of point pairs would be matched at large angles when the trailer's profile significantly changes from its zero-degree position. Meanwhile, Method 2 combines DB 1 and DB 2. The number of corresponding point pairs matched in DB 2 (indicated as (c) in Figure 3.15) are generally more than those from DB 1. Again, this is expected because the algorithm makes it a priority to choose a reference angle $\widehat{\theta}_r$ that is close to the most recent estimated trailer angle (lines 5 and 6 of DB2Online, Algorithm 6). This means that the current set of radar detections is few angles away from the $\widehat{\theta}_r$-degree reference set, which in turn yields more pairs of points to be matched for correspondence. Generally, it is better to have more point pairs matched for correspondence because the radar detections are quantized. More points would sample the quantized

space better than with few points. Therefore, this analysis suggests that Method 2 will be favored in situations when Method 1 could only match very few points for correspondence.

3.5.1 Computational Analysis

The methods were implemented in [1]MATLAB R2019b [31] on a 2.50GHz CPU, 12GB RAM computer. The radar data was collected at a rate of $3Hz$ for a duration of 104 secs. This makes 312 time steps in the dataset. We post-processed a saved dataset which was pre-loaded into the MATLAB workspace. Therefore, the analysis presented in this section includes the time it took the algorithm to read the detections for each time step from the workspace.

3.5.1.1 Analysis on Method 1

As illustrated in Figure 3.3, the 'Point set correspondence' module is in the 'Detector block' which is also in the 'Detector block and Kalman filter'. The cumulative computation time for the three items is presented in Figure 3.16. The error bar on each item represents the standard error (standard deviation estimate) of the computation time vector recorded over the time steps.

[1]We expect the algorithms to still run faster with Python and C languages.

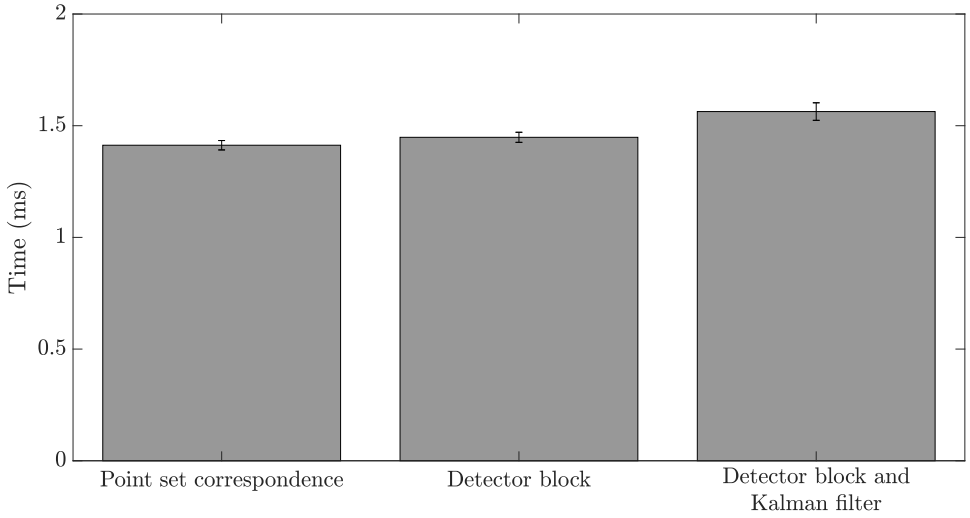

Figure 3.16: Average computation time for Method 1 at $\boldsymbol{\delta = 2°}$.

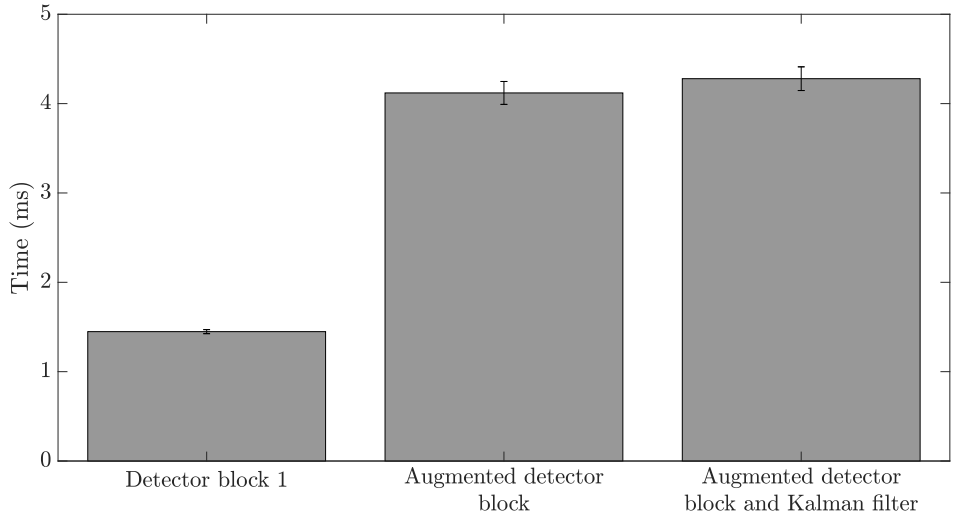

Figure 3.17: Average computation time for Method 2 at $\boldsymbol{\delta = 2°}$ and online set learning parameters $\theta_{interval} = 5°$, $\theta_{difference} = 1°$.

The input sets to the point set correspondence module had different sizes depending on the number of radar detections found within the ROI, shown as (a) in Figure 3.15. Hence, the variation in computation time indicated by the error bars.

The constrained orthogonal Procrustes solution, based on the SVD operation on a 2×2 matrix, is very cheap to compute. Radar collection at a rate of $3Hz$ gives a time interval of about $333ms$ in between the collection. Meanwhile, the average computation time spent on the method (Detector block and Kalman filter) $\approx 1.6ms$. This suggests that the method is feasible for deployment.

3.5.1.2 Analysis on Method 2

In Figure 3.8, the 'Detector block 1' is in the 'Augmented detector block' which is also in the 'Augmented detector block and Kalman filter'. The cumulative computation time for the three items is presented in Figure 3.17. As seen with the error bars, the variation in computation time on 'Augmented detector block' is noticeably more than that of 'Detector block 1'. This is due to the set learning process which involves a decision to either accept or reject a candidate set during the execution of DB2Online in Algorithm 6.

The average computation time spent on the method (Augmented detector block and Kalman filter) $\approx 4.5ms$ while the time interval in between data collection is $333ms$. This again suggests that the method is feasible for deployment.

3.6 More Results based on Supplemental Indoor and Outdoor Data Collections[1]

To further test the trailer angle estimation algorithm, more experiments were carried out in both indoor and outdoor environments. In the experiments, the transformation parameters, based on the radar geometry illustrated in Figure 3.4, are:

$$\alpha = 19.0^{\circ}, \quad \beta = 20.0^{\circ}$$

$$w_1 = w_2 = 0.8m, \qquad v = 0.32m$$

The parameters were obtained by directly measuring the dimensions from the experimental apparatus with protractors and a meter rule. The radar mount angle parameters (α, β) differ from those provided in section 3.5 because the angles were adjusted on the apparatus to demonstrate the performance of the algorithm with the new mount angles. The estimation results for each experiment are presented and discussed as follows.

[1]The supplemental experiments were conducted after submitting the research for publication.

3.6.1 Trailer Angle Estimates with Supplemental Indoor Dataset

A supplemental experiment was conducted in the same indoor environment where the experiment presented in section 3.5 was carried out. The environment has a smooth floor surface, which makes the truck mock-up vibrate minimally during the trailer rotation. The trailer was rotated through a range of ground truth angles $[-43.25^\circ \;\; 43.00^\circ]$ and the radar data was collected at a rate of $3Hz$ for a duration of 190 secs. This makes 570 time steps in the dataset.

The estimates of the trailer angle are obtained with respect to the two methods discussed in section 3.4. The results based on using estimation Method 1 ($\delta = 2^\circ$) and Method 2 ($\delta = 2^\circ, \theta_{interval} = 5^\circ$, and $\theta_{difference} = 1^\circ$) are provided in Figure 3.18. More results are summarized with the RMSE performance metric for the Method 1 estimates in Table 3.4 and for the Method 2 estimates in Table 3.5. It can be observed from the figure that the estimates tend to be more accurate at smaller angles than at larger angles; the estimation errors are larger as the trailer's true rotation angle approaches $\pm 40^\circ$. The RMSE values provided in the tables for both methods seem comparable. However, as shown in Figure 3.19, the number of point set matches obtained with estimation Method 2 are in most cases more than the number of matches obtained with Method 1. This is a similar result presented in section 3.5.

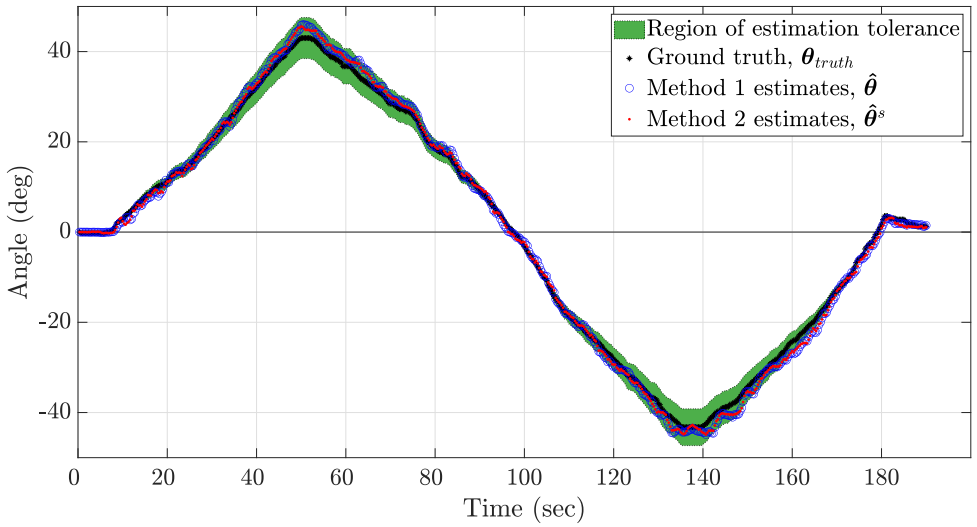

Figure 3.18: INDOOR DATASET: The **Kalman-filtered** estimates from both methods: Method 1 ($\boldsymbol{\delta = 2°}$) and Method 2 ($\boldsymbol{\delta = 2°}, \theta_{interval} = 5°$, and $\theta_{difference} = 1°$).

Table 3.4
INDOOR DATASET: Performance metric of Method 1 estimates $\widehat{\boldsymbol{\theta}}$ (in degrees)

	$\delta = 5°$	$\delta = 4°$	$\delta = 3°$	$\delta = 2°$	$\delta = 1°$
$RMSE_{(\widehat{\boldsymbol{\theta}})}$	1.37	1.37	1.38	1.37	1.45

Table 3.5
INDOOR DATASET: $RMSE_{(\widehat{\boldsymbol{\theta}}^s)}$ of Method 2 estimates varied by the online set learning parameters (in degrees)

		$\theta_{difference} = 1°$					$\theta_{difference} = 2°$				
		$\delta = 5°$	$\delta = 4°$	$\delta = 3°$	$\delta = 2°$	$\delta = 1°$	$\delta = 5°$	$\delta = 4°$	$\delta = 3°$	$\delta = 2°$	$\delta = 1°$
$\theta_{interval}$	5°	1.35	1.34	1.35	1.32	1.41	1.67	1.33	1.33	1.33	1.38
	6°	1.34	1.36	1.32	1.37	1.43	1.70	1.51	1.29	1.47	1.42
	7°	1.32	1.34	1.35	1.37	1.44	1.69	1.41	1.38	1.44	1.33
	8°	1.37	1.39	1.38	1.41	1.47	1.76	1.36	1.25	1.23	1.34
	9°	1.37	1.37	1.32	1.40	1.46	1.67	1.35	1.35	1.44	1.41
	10°	1.39	1.39	1.35	1.40	1.49	1.73	1.48	1.40	1.47	1.45

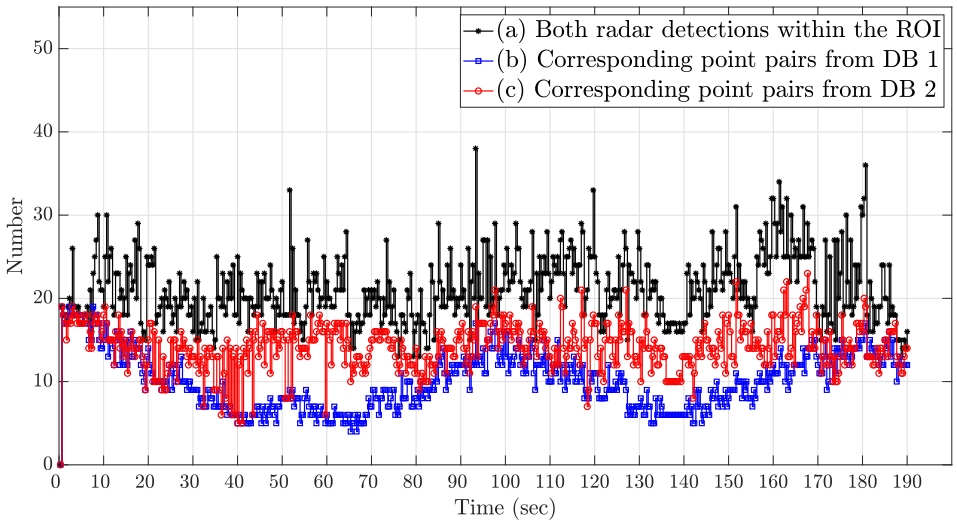

Figure 3.19: INDOOR DATASET: (a) The number of the combined detections from both radars found within the ROI. (b) The number of point pairs matched by the point set correspondence module in detector block 1, ($\boldsymbol{\delta = 2°}$). (c) The number of point pairs matched by the point set correspondence module in detector block 2, ($\boldsymbol{\delta = 2°}, \theta_{interval} = 5°$, and $\theta_{difference} = 1°$).

Figure 3.20: The experimental apparatus in an outdoor environment for data collection. The inset image shows the roughness of the ground surface.

3.6.2 Trailer Angle Estimates with Supplemental Outdoor Dataset

Another experiment was conducted in an outdoor environment which is shown in Figure 3.20. As depicted in the figure, the texture of the ground is rough. The roughness makes the radars on the truck mock-up vibrate significantly during data collection. The trailer was rotated through a range of ground truth angles $[-39.00^\circ \;\; 47.00^\circ]$ and the data was collected at a rate of $3Hz$ for a total of 335 data samples. This gives a duration of about 111.67 secs.

Again, the trailer angle estimates are obtained using the two estimation methods. The estimates for Method 1 ($\delta = 2^\circ$) and Method 2 ($\delta = 2^\circ, \theta_{interval} = 5^\circ$, and $\theta_{difference} = 1^\circ$) are provided in Figure 3.21. More results are summarized using the RMSE performance metric in Table 3.6 for the Method 1 estimates and in Table 3.7 for the Method 2 estimates. Like the indoor-based results, the number of point set matches obtained with estimation Method 2 are in most cases more than the number of matches obtained with Method 1, this is shown in Figure 3.22.

We observe from Figure 3.21 that the estimates seem to follow the trend of the ground truth. However, there are some estimation errors. One of the causes of the errors is the vibration of the truck mock-up. Vehicle vibration is known to degrade

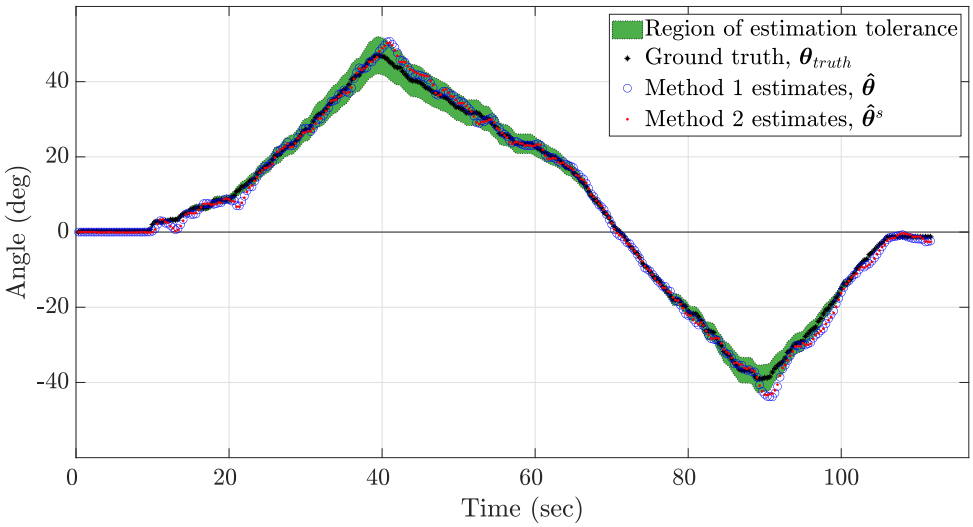

Figure 3.21: OUTDOOR DATASET: The **Kalman-filtered** estimates from both methods: Method 1 ($\boldsymbol{\delta = 2°}$) and Method 2 ($\boldsymbol{\delta = 2°}, \theta_{interval} = 5°$, and $\theta_{difference} = 1°$).

Table 3.6
OUTDOOR DATASET: Performance metric of Method 1 estimates $\widehat{\boldsymbol{\theta}}$ (in degrees)

	$\delta = 5°$	$\delta = 4°$	$\delta = 3°$	$\delta = 2°$	$\delta = 1°$
$RMSE_{(\widehat{\boldsymbol{\theta}})}$	2.97	1.70	1.52	1.57	1.73

Table 3.7
OUTDOOR DATASET: $RMSE_{(\widehat{\boldsymbol{\theta}}^s)}$ of Method 2 estimates varied by the online set learning parameters (in degrees)

		$\theta_{difference} = 1°$					$\theta_{difference} = 2°$				
		$\delta = 5°$	$\delta = 4°$	$\delta = 3°$	$\delta = 2°$	$\delta = 1°$	$\delta = 5°$	$\delta = 4°$	$\delta = 3°$	$\delta = 2°$	$\delta = 1°$
$\theta_{interval}$	5°	3.22	1.75	1.63	1.61	1.76	8.98	1.52	1.39	1.52	1.78
	6°	3.19	1.48	1.69	1.57	1.83	1.37	1.44	1.47	1.40	1.77
	7°	3.10	1.67	1.59	1.55	1.84	10.15	1.59	1.60	1.38	1.85
	8°	3.20	1.54	1.50	1.56	1.84	1.88	1.84	1.60	1.51	1.76
	9°	3.25	1.56	1.58	1.54	1.69	1.65	1.42	1.39	1.39	1.79
	10°	3.25	3.09	1.60	1.55	1.77	1.73	1.46	1.53	1.66	1.77

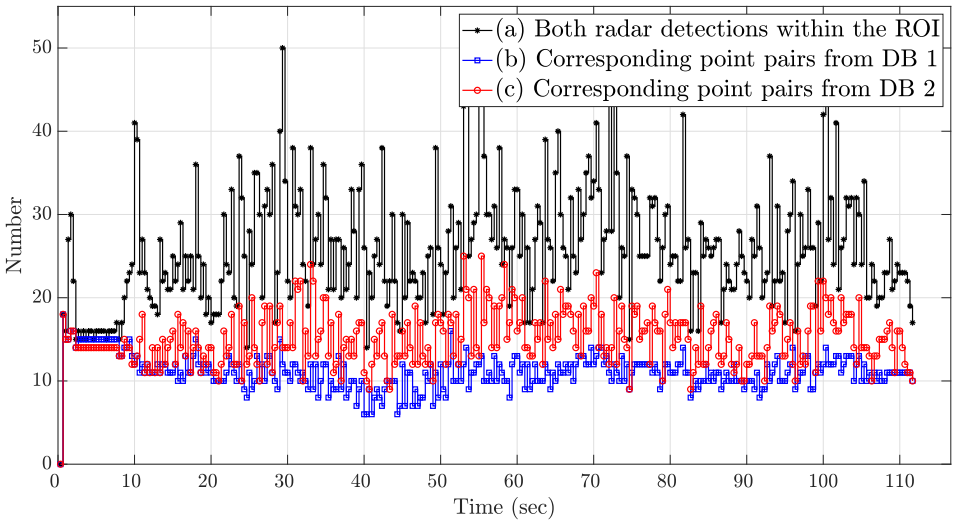

Figure 3.22: OUTDOOR DATASET: (a) The number of the combined detections from both radars found within the ROI. (b) The number of point pairs matched by the point set correspondence module in detector block 1, ($\boldsymbol{\delta = 2°}$). (c) The number of point pairs matched by the point set correspondence module in detector block 2, ($\boldsymbol{\delta = 2°}, \theta_{interval} = 5°$, and $\theta_{difference} = 1°$).

the performance of radar detections [32–34]. This suggests that the vibration effect should be mitigated [35–37] before using the detections in the estimation algorithm.

We also observe from Tables 3.6 and 3.7 that the RMSE values of most estimates are below 2.00°. In many cases, the RMSE values which exceed 2.00°, show that the algorithm lost track of the trailer during motion, suggesting that radar-only data may not be sufficient to track the trailer in motion. Hence, the radars may be fused with another sensor such as the camera for improved tracking performance.

We include the mitigation of radar vibration effects and a consideration of multi-sensor fusion for trailer tracking in a list of future research recommendations in chapter 7.

3.7 Conclusion

We showed that the trailer angle (or hitch angle) can be estimated using the already-installed radar sensors on a truck. This was implemented in experiments conducted in both indoor and outdoor environments. The apparatus used in the experiments consisted of two radars installed on a trailer-coupled mock-up truck. We provided two methods for the estimation. The basic operating principle is in the reduction of the radar threshold to obtain more trailer detections. This increased the false positives. While the true trailer detections are persistent, the false positives are not. The two methods used this idea to obtain the persistent detections which in turn resulted in an estimate of the trailer angle. It is shown from the results that the estimates obtained based on indoor dataset are more accurate than those obtained based on outdoor dataset. The challenges observed with the outdoor dataset are presented. In general, the results and computational cost analysis on both methods are promising and they suggest that the estimation approach is feasible for deployment.

Chapter 4

Least Squares Calibration of Automotive Radar Mount Angles and Translation Vectors

4.1 Chapter abstract

Radars are part of the sensor suite installed on modern vehicles for environmental perception. The position and orientation of the radar must be known in order to transform the detections from the radar coordinate system to a vehicle coordinate

The material contained in this chapter has been submitted to the IEEE Transactions on Instrumentation and Measurement. The work was supported by the Ford Motor Company as an Alliance Project under Ford/MTU Master Agreement #83437205.

system (VCS), which is a common requirement for multi-sensor fusion. We present an extrinsic calibration method which estimates the radar mount angle and translation vector parameters needed to transform radar detections onto the VCS. The origin of the VCS is not constrained to be on the vehicle, it can be chosen as convenient. The method compares the radar detections of objects such as corner reflectors and known locations of the objects in the VCS for the estimation. It also considers the quantization of the detections for refined estimation of the parameters. The algorithm can be used with one or two radars installed either in front or at the back of a vehicle. It was tested with both synthetic and radar data. The radar data experiment was conducted using two blind spot information radars installed in the tail light fixtures of a truck. The results obtained from the synthetic and radar data suggest that the algorithm is feasible for deployment.

4.2 Introduction

Multiple sensors are increasingly being deployed in systems, and the sensors are often integrated for fused measurements. This is commonly seen in multi-sensor fusion and environmental perception applications. The measurement precision of the individual sensors and the fused sensor network depends on successful calibration of the sensors. Calibration methods can either be intrinsic or extrinsic. Intrinsic calibration is concerned with the internal working parameters of a sensor, such as its frequency of

operation, while extrinsic calibration considers the installation geometry. The sensor geometry is often considered with respect to rigid transformation; sensor orientation (due to the mount angles) and position. Hence, extrinsic calibration, which is considered in this work, deals with the spatial transformation of the detections from different sensor coordinates onto a common coordinate system for signal processing.

There are some existing extrinsic calibration methods available for different types of sensors. For instance, extrinsic calibration algorithms are presented for cameras in [38, 39], for a combination of lidar and camera in [40–42], and for a combination of laser scanner and camera in [43–46]. We consider automotive radar sensors in this work. Unlike lidars and laser scanners which provide high density detections for signal processing and camera image frames which contain a considerably large number of pixels for image processing, the detections from radar sensors are sparse. The sparsity of the radar detections tends to make the processing of radar-only data challenging.

Interestingly, the development of methods and apparatus for extrinsic calibration of radars has attracted the interests of researchers, especially those in the automotive industry. This has resulted in a number of research articles and patents. The method presented in [47] requires a truck, on which radars have been installed, to be placed on a transport system. The longitudinal axis of the truck is made to align with that of the transport system using a track system such as a conveyor belt. The transport system is then moved along a known path past one or more corner reflectors.

The radar detections with respect to the corner reflectors are used to calibrate the radars. The method in [48, 49] also requires the vehicle to be driven past a target object. The captured data is then evaluated offline with an occupancy grid map over a range of candidate mount angles. The optimum angle estimate is selected based on a performance metric. The authors in [50] calibrated multiple radars with respect to a high definition digital map intended for autonomous navigation of the vehicle. The work considered both rotation and translation components needed for the calibration. Two 3D radar sensors were calibrated in [51] using the difference in locations reported by the radars for the same target. Among other considerations, the algorithm assumes that the detections do not contain location error. It was tested using synthetic data. The authors in [52] studied the angular misalignment of a group of sensors using synthetic data. They estimated only the rotation components. The sensor locations, used as translation components in the algorithm, were to be known. In [53], an alignment apparatus having a minimum of three corner-reflector targets was provided. The method requires the distances of the targets to the radar sensor on the truck. It then compares the known distances of the targets with the radar detections for calibration. The method in [54] requires at least one target with known location to be placed in a radar's field of view. The radar detection is then compared with the known location to compute a correction value.

In this work, we perform an extrinsic calibration of [1]two radars installed at the rear

[1]The algorithm can be used with one or two radars installed either in front or at the back of a truck.

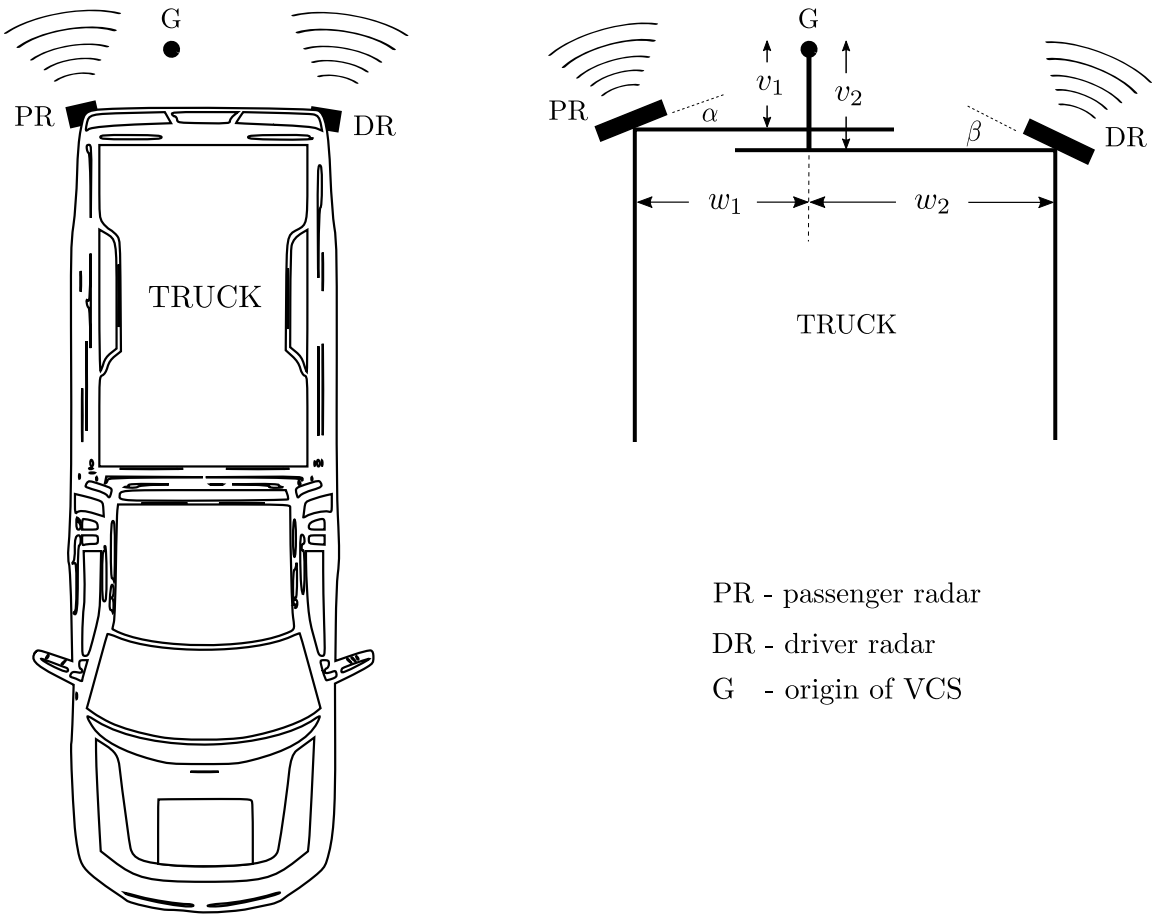

Figure 4.1: *Left*: A diagram showing two radars installed at the rear of a truck and a user-defined spatial point G, which is the origin of the vehicle coordinate system (VCS). *Right*: A schematic diagram showing the geometry of the two radars with respect to the spatial point. Six parameters will be estimated; the radar **mount angles** α, β and the **translation parameters** w_1, w_2, v_1, v_2. The mount angles are defined with respect to the truck's lateral line. The perpendicular distances from G to the lateral lines which connect PR and DR are respectively v_1 and v_2. The geometry is robust to both cases where $v_1 = v_2$ and $v_1 \neq v_2$.

of a truck (as illustrated in Figure 4.1) with respect to a user-defined spatial point G. We assume that the radars have been calibrated intrinsically. The spatial point G is the origin of the vehicle coordinate system (VCS) onto which the detections will be transformed, the point does not have to be located on the truck. The algorithm

requires the locations of objects such as corner reflectors (CRs) to be known in the VCS for comparison with the radar detections of the CRs to estimate the rotation and translation parameters needed for the calibration. The rotation parameters correspond to the mount angles of the radars while the translation parameters define two translation vectors for both radars. When used with one radar, the algorithm estimates the radar's mount angle and a translation vector. The work was tested using both synthetic and radar data. Unlike prior methods such as [53, 54], the location requirement of the CRs are not defined with respect to the radar, but the VCS, which is an advantage since a radar installed behind a radome is not easily accessible.

The rest of the paper is arranged as follows: section 4.3 describes the problem statement and experimental apparatus, a preliminary result is presented in section 4.4, the calibration method is discussed in section 4.5, the results are presented and discussed in section 4.6, and conclusion presented in section 4.7. These define the general notations: $\boldsymbol{x}$ in bold lower case is a column vector, X in upper case is a matrix, and ^{T} represents a transpose operation.

4.3 Problem Statement and Experimental Apparatus

4.3.1 Problem Statement

We want to estimate the **six parameters** illustrated in Figure 4.1 with respect to the geometry of the passenger radar (PR), the driver radar (DR), and the spatial point G. The parameters are **mount angles** α, β and **translation parameters** w_1, w_2, v_1, v_2. The mount angles are defined with respect to the truck's lateral line. Both radars provide detections in two dimensions. There are three parameters per radar. For instance, extrinsically calibrating only the passenger radar reduces the problem to estimating α, w_1, and v_1. The estimates are needed to rigidly transform detections from the coordinates of the radars onto the VCS.

4.3.2 Experimental Apparatus for Data Collection

This work was tested using both synthetic data and radar data collected in an experiment. In the radar data experiment, we let G in Figure 4.1 be the location of the hitch ball (the user may define another location). The radar data was collected

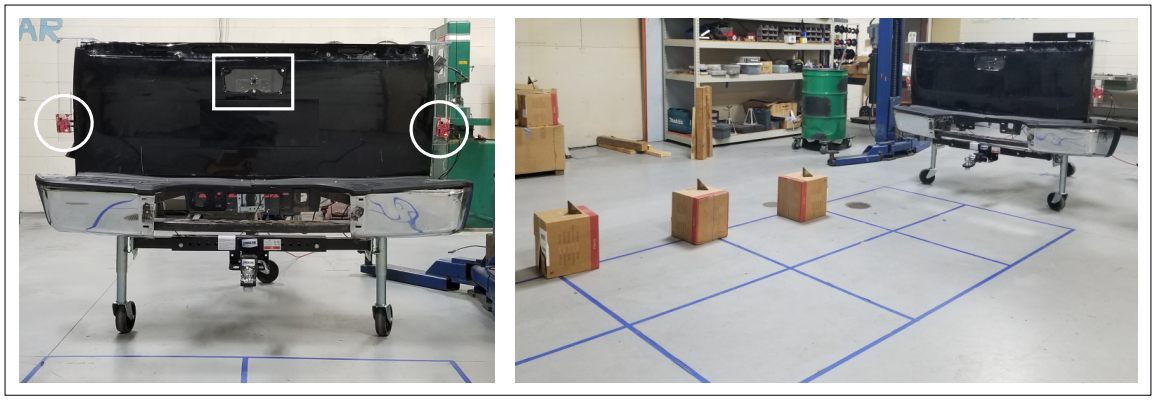

Figure 4.2: *Left*: A truck mock-up consisting of a rear gate mounted on a three-wheel platform. Two **radars** (encircled) are installed on a plexiglass surface at the tail light areas. A **camera** (in square bounds) was also installed for visualization, it was not used for the calibration. A **protractor** is locked to the top of each radar's plexiglass to read the mount angle (ground truth) which will be estimated. *Right*: A calibration scenario where corner reflectors (on top of boxes) were placed in the field of view of one of the radars.

using the apparatus shown in Figure 4.2. The apparatus consists of a truck's rear gate mounted on a three-wheel platform, referred to as the truck mock-up. The blue grid lines on the floor represent the VCS whose origin is at G, the hitch ball. The grid is marked at $1m$ apart in the longitudinal direction. The lateral distances from the grid's origin extend in each direction at lengths $w_1 = 0.8m$ and $w_2 = 0.8m$. The grid was used as a quick guide to measure the locations of the CRs in the VCS. The CRs used in this work are $10dBsm$ trihedral.

Two TI AWR1642BOOST automotive radar modules [25] were installed at the sides of the truck mock-up. Each radar has 2 transmit and 4 receive channels and operates in the $76-81$GHz frequency band. Its frequency-modulated continuous-wave (FMCW) waveform use up to 4GHz bandwidth. Both radars are separately located and have

individual oscillators. No attempt was made to synchronize the operation of the two radars. Also, we did not process the raw radar data since the TI module provides the two-dimensional point detections already. The radar's waveform was designed to have a range resolution of about $4.1cm$ and a maximum range of about $6.5m$ based on our experiment. We used a high constant false alarm rate (CFAR) range threshold of $15dB$ to reject as much clutter as possible. The user may adapt the waveform and CFAR threshold according to the use case.

4.4 Preliminary Result

In many applications involving rigid transformation of point sets, there exists the following mathematical problem, defined in this work for two-dimensional sets and in the form provided below. Given two corresponding point sets $A, B \in \mathbb{R}^{2\times k}$ such that

$$A = Q_{(\phi)}B - \begin{bmatrix} t_1 \\ t_2 \end{bmatrix} \mathbf{1}_k^T + N$$

where

$$Q_{(\phi)} = \begin{bmatrix} \cos(\phi) & -\sin(\phi) \\ \sin(\phi) & \cos(\phi) \end{bmatrix}$$

is a rotation matrix which rotates a two-dimensional vector at an angle ϕ in the counter-clockwise direction for positive ϕ, $\mathbf{1}_k^T$ is a row vector of k ones so that the

term

$$-\begin{bmatrix} t_1 \\ t_2 \end{bmatrix} \mathbf{1}_k^T$$

is a translation matrix, and $N \in \mathbb{R}^{2\times k}$ is a noise matrix. We are required to estimate the rotation angle ϕ and translation vector parameters t_1, t_2 according to the least squares minimization

$$\widetilde{\phi}, \widetilde{t}_1, \widetilde{t}_2 = \underset{\phi, t_1, t_2}{\operatorname{argmin}} \left\| A - \left(Q_{(\phi)} B - \begin{bmatrix} t_1 \\ t_2 \end{bmatrix} \mathbf{1}_k^T \right) \right\|_F^2 \tag{4.1}$$

where $\|.\|_F$ is the Frobenius norm. Let $\boldsymbol{a}_i$ and $\boldsymbol{b}_i$ be the ith column vectors in A and B respectively; then (4.1) can be re-written as

$$\widetilde{\phi}, \widetilde{t}_1, \widetilde{t}_2 = \underset{\phi, t_1, t_2}{\operatorname{argmin}} \sum_{i=1}^{k} \left\| \boldsymbol{a}_i - \left(Q_{(\phi)} \boldsymbol{b}_i - \begin{bmatrix} t_1 \\ t_2 \end{bmatrix} \right) \right\|^2 \tag{4.2}$$

where $\|.\|$ is the 2-norm.

We assume that the rotation operation performed by $Q_{(\widetilde{\phi})}$ is around an axis that passes through the origin of the coordinate system of B [55, 56]. This assumption makes (4.2) a partial Procrustes superimposition problem whose rotational component is obtained using the Kabsch algorithm [57]. Its solution is given [55, 57] by decoupling the rotation and translation components (a consequence of the centroid coincidence theorem, proof in [56]) as follows:

Let the centroids of point sets A and B be respectively obtained as:

$$\boldsymbol{\mu}_A = \frac{1}{k}\sum_{i=1}^{k} \boldsymbol{a}_i$$
$$\boldsymbol{\mu}_B = \frac{1}{k}\sum_{i=1}^{k} \boldsymbol{b}_i$$

Let us subtract the centroids off the two sets as follows:

$$A_o = A - \boldsymbol{\mu}_A \mathbf{1}_k^T$$

$$B_o = B - \boldsymbol{\mu}_B \mathbf{1}_k^T$$

The best proper rotation is solved using the zero-centroid sets,

$$\widetilde{\phi} = \underset{\phi}{\operatorname{argmin}} \left\| A_o - Q_{(\phi)} B_o \right\|_F^2 \tag{4.3}$$

subject to

$$Q_{(\phi)}^T Q_{(\phi)} = I,\ \det\left(Q_{(\phi)}\right) = +1$$

This is the constrained orthogonal Procrustes problem [28][29] whose solution is provided as function ORTHOANGLE in Algorithm 7. The estimate of the translation vector is then obtained [55] by using $Q_{(\widetilde{\phi})}$ $\left(\text{the best rotation matrix that solves (4.2)}\right)$

Algorithm 7 Estimation of rigid transformation parameters

procedure KABSCH(A, B, `option`)
  $\boldsymbol{\mu}_A, \boldsymbol{\mu}_B \leftarrow$ centroids of sets A, B respectively
  $A_o \leftarrow A - \boldsymbol{\mu}_A \mathbf{1}_k^T$
  $B_o \leftarrow B - \boldsymbol{\mu}_B \mathbf{1}_k^T$
  ▷ Obtain the rotation angle estimate
  $\widetilde{\phi} \leftarrow$ ORTHOANGLE$\big(A_o, B_o\big)$ ▷ The **function** given below
  ▷ Obtain the translation parameter estimates
  $\begin{bmatrix} \widetilde{t}_1 \\ \widetilde{t}_2 \end{bmatrix} = Q_{(\widetilde{\phi})} \boldsymbol{\mu}_B - \boldsymbol{\mu}_A$
  if `option` is `rotation` **then**
    return $\widetilde{\phi}$
  else if `option` is `translation` **then**
    return $\begin{bmatrix} \widetilde{t}_1 \\ \widetilde{t}_2 \end{bmatrix}$
  end if
end procedure

function ORTHOANGLE(A_o, B_o)
  $W \Sigma V^T \leftarrow \text{SVD}\left(A_o B_o^T\right)$
  ▷ This is the singular value decomposition (SVD)
  ▷ Let the singular values in Σ be arranged in descending order
  $Q_{(\widetilde{\phi})} \leftarrow W \begin{bmatrix} 1 & 0 \\ 0 & \det(WV^T) \end{bmatrix} V^T$
  ▷ The diagonal matrix ensures the determinant $\det\left(Q_{(\widehat{\phi})}\right) = +1$
  Obtain angle $\widetilde{\phi}$ from the 2×2 rotation matrix $Q_{(\widetilde{\phi})}$
  return $\widetilde{\phi}$
end function

and the two centroids:

$$\begin{bmatrix} \widetilde{t}_1 \\ \\ \widetilde{t}_2 \end{bmatrix} = Q_{(\widetilde{\phi})} \boldsymbol{\mu}_B - \boldsymbol{\mu}_A$$

The estimation steps provided above are summarized in Algorithm 7, for ease of reuse in the remainder of this paper, such that a given problem of the form provided in

(4.1) is solved as:

$$\widetilde{\phi} = \textsc{Kabsch}\big(A, B, \texttt{rotation}\big)$$

$$\begin{bmatrix} \widetilde{t}_1 \\ \\ \widetilde{t}_2 \end{bmatrix} = \textsc{Kabsch}\big(A, B, \texttt{translation}\big)$$

There should be at least two unique vectors in each set ($k \geq 2$) to ensure a unique solution due to the use of the SVD in the algorithm.

4.5 Method

The basic operating principle of the calibration method is as follows. Let k CRs be placed in the field of view of a radar (as depicted for the passenger radar in Figure 4.3) and their locations in the **vehicle coordinate system** (VCS) be known. The reflectors' known locations in the VCS will be compared with the radar detections to estimate the parameters.

The **point-set variables** which will be used in the algorithm are defined as follows.

(a) *Three variables when the k CRs are in the PR field of view*:

X_{vcs}^{PR} – known locations of the CRs in the VCS

X_{pr} – passenger radar detections of the CRs, expressed in Cartesian coordinates

X_{pr}^{G} – rigid transformation of X_{pr} onto the VCS

(b) *Three variables when the k CRs are in the DR field of view*:

X_{vcs}^{DR} – known locations of the CRs in the VCS

X_{dr} – driver radar detections of the CRs, expressed in Cartesian coordinates

X_{dr}^{G} – rigid transformation of X_{dr} onto the VCS

Assumptions

The algorithm assumes the following:

1. The VCS has an origin at a conveniently chosen point G, and its horizontal and vertical axes align with the lateral and longitudinal lines, respectively, of the vechicle.

2. The three point-set variables defined for each radar have **correspondence** and the size of each set is $2 \times k$. This means that the ith column vector in each set represents the ith CR. The correspondence can be easily achieved if the calibration is performed in a controlled environment, free of clutter. This makes it easy to associate the detections with the CRs.

3. The estimate of the rotational operation (due to the radar mount angle) is taken to be around an axis that passes through the origin of the radar coordinate system. This is also an assumption in [55, 56].

Sign of the parameters

To prevent ambiguity in the equations presented in this paper, all the six parameters (α, β, w_1, w_2, v_1, and v_2) are taken to be positive with respect to the geometry shown in Figure 4.3. This means that v_1 would be negative if G was below the lateral line which connects to PR, and w_1 would be negative if G was located to the left side of PR.

Three parameters will be estimated per radar. The estimation with respect to one radar is independent of the second radar.

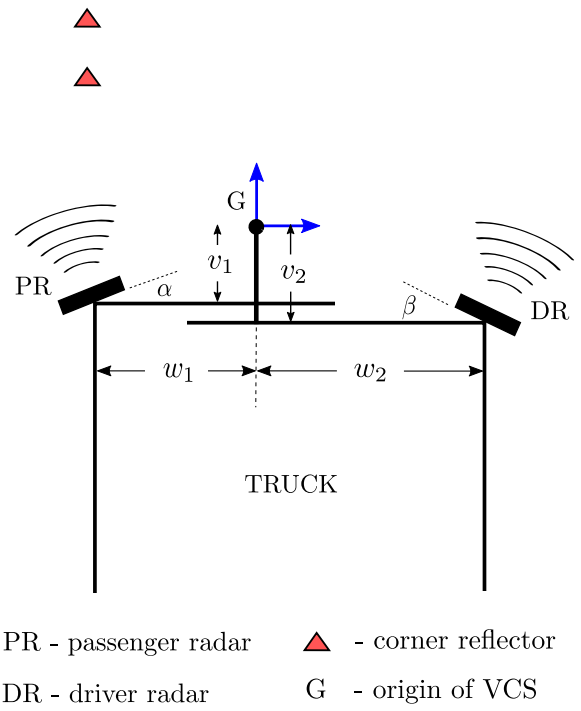

Figure 4.3: An illustration of $k = 2$ corner reflectors placed in the passenger radar's field of view. The orthogonal vectors indicated with blue arrows represent the VCS.

4.5.1 Estimation of α, w_1, and v_1 using the passenger radar

Let k corner reflectors be placed in the PR field of view as illustrated in Figure 4.3.

The PR detections can be transformed onto the VCS as follows:

$$X_{pr}^{G} = Q_{(\alpha)} X_{pr} - \begin{bmatrix} w_1 \\ v_1 \end{bmatrix} \mathbf{1}_k^T$$

Let $X_{pr}^{G} \approx X_{vcs}^{PR}$ i.e. the transformed detections onto the VCS are approximately equal to the known locations of the CRs in the VCS, so that

$$X_{vcs}^{PR} \approx Q_{(\alpha)} X_{pr} - \begin{bmatrix} w_1 \\ \\ v_1 \end{bmatrix} \mathbf{1}_k^T$$

The least-squares estimation problem is to solve for

$$\widetilde{\alpha}, \widetilde{w}_1, \widetilde{v}_1 = \underset{\alpha, w_1, v_1}{\operatorname{argmin}} \left\| X_{vcs}^{PR} - \left(Q_{(\alpha)} X_{pr} - \begin{bmatrix} w_1 \\ \\ v_1 \end{bmatrix} \mathbf{1}_k^T \right) \right\|_F^2 \tag{4.4}$$

which is of the form provided in (4.1). As described in the list of assumptions (Assumption 3), let the rotation estimate $Q_{(\widetilde{\alpha})}$ be around an axis that passes through the origin of the radar coordinate system. Therefore, the estimates of the parameters with respect to Algorithm 7 are:

$$\widetilde{\alpha} = \textsc{Kabsch}\big(X_{vcs}^{PR}, X_{pr}, \texttt{rotation}\big)$$

$$\begin{bmatrix} \widetilde{w}_1 \\ \\ \widetilde{v}_1 \end{bmatrix} = \textsc{Kabsch}\big(X_{vcs}^{PR}, X_{pr}, \texttt{translation}\big)$$

The one-time estimates, obtained with one pair of point sets X_{vcs}^{PR} and X_{pr}, may not be sufficiently accurate since radar detections are quantized in space. Therefore, let us use multiple pairs of point sets (multiple observations) to refine the estimates. The

user can obtain a new set of observations by moving one or more corner reflector(s) at known distance(s), or by moving the truck instead at a known distance, while recording the locations of the CRs in the VCS and also saving the radar detections of the CRs. The process of moving the reflectors may be automated in an industrial setting. We moved the reflectors manually in our experimental work.

Let the number of observations i.e. the number point set pairs obtained be n, which is a value decided by the user. Also, let $X^{PR}_{vcs(i)}$ be the ith set containing the locations of the CRs in the VCS and $X_{pr(i)}$ be the ith set containing the passenger radar detections of the CRs. We present these two methods to refine the estimates:

4.5.1.1 Refinement by averaging multiple estimates

This method models the radar quantization error as additive white noise [58, 59]. Multiple estimates of a parameter will be averaged with the aim of removing the zero-mean noise.

Let the ith observation be used to estimate the parameters as follows:

$$\widetilde{\alpha}_i = \textsc{Kabsch}\big(X^{PR}_{vcs(i)}, X_{pr(i)}, \texttt{rotation}\big)$$

$$\begin{bmatrix} \widetilde{w}_{1_i} \\ \\ \widetilde{v}_{1_i} \end{bmatrix} = \textsc{Kabsch}\big(X^{PR}_{vcs(i)}, X_{pr(i)}, \texttt{translation}\big)$$

such that there are n estimates for each parameter. Using this method, the refined estimate is the average of the n estimates.

$$\Big[\widehat{\alpha},\, \widehat{w}_1,\, \widehat{v}_1\Big] = \frac{1}{n}\sum_{i=1}^{n}\Big[\widetilde{\alpha}_i\, \widetilde{w}_{1_i},\, \widetilde{v}_{1_i}\Big]$$

with the expression taken to be an element-wise operation i.e.

$$\widehat{\alpha} = \frac{1}{n}\sum_{i=1}^{n}\widetilde{\alpha}_i$$

4.5.1.2 Refinement based on global estimation

The objective of this method is to combine point set observations $X^{PR}_{vcs(i)}$ and $X_{pr(i)}$, for $i = 1 : n$, into two large sets so that the least squares estimation procedure can be performed globally, at once. This model aims to reduce the effect of radar quantization as the number of data points in the large sets increases i.e. as n increases.

Let us populate the sets as follows:

$$X^{PR}_{vcs_{all}} = \Big[X^{PR}_{vcs(1)},\ X^{PR}_{vcs(2)},\ \ldots\ ,\ X^{PR}_{vcs(n)}\Big] \in \mathbb{R}^{2\times kn}$$
$$X_{pr_{all}} = \Big[X_{pr(1)},\ X_{pr(2)},\ \ldots\ ,\ X_{pr(n)}\Big] \in \mathbb{R}^{2\times kn}$$

so that the parameters can be estimated globally by extending (4.4) to include all n observations,

$$\widehat{\alpha}_g, \widehat{w}_{1_g}, \widehat{v}_{1_g} = \underset{\alpha, w_1, v_1}{\operatorname{argmin}} \left\| X^{PR}_{vcs_{all}} - \left(Q_{(\alpha)} X_{pr_{all}} - \begin{bmatrix} w_1 \\ \\ v_1 \end{bmatrix} \mathbf{1}^T_{kn} \right) \right\|^2_F \tag{4.5}$$

The estimates are obtained using Algorithm 7:

$$\widehat{\alpha}_g = \textsc{Kabsch}\big(X^{PR}_{vcs_{all}}, X_{pr_{all}}, \texttt{rotation}\big)$$
$$\begin{bmatrix} \widehat{w}_{1_g} \\ \\ \widehat{v}_{1_g} \end{bmatrix} = \textsc{Kabsch}\big(X^{PR}_{vcs_{all}}, X_{pr_{all}}, \texttt{translation}\big)$$

where the subscript g on the estimates denotes that the estimation was performed *globally*.

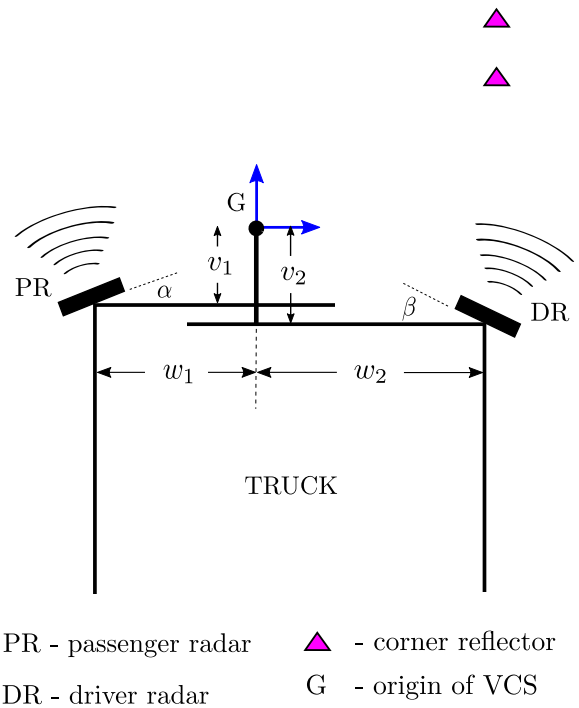

Figure 4.4: An illustration of $k = 2$ corner reflectors placed in the driver radar's field of view. The orthogonal vectors indicated with blue arrows represent the VCS.

4.5.2 Estimation of β, w_2, and v using the driver radar

This will be independently performed like section 4.5.1, however, there will be some **sign changes**. Let k reflectors be placed in the DR field of view as illustrated in Figure 4.4. We transform the DR detections onto the VCS as follows:

$$X_{dr}^{G} = Q_{(\beta)}^{T} X_{dr} - \begin{bmatrix} -w_2 \\ \\ v_2 \end{bmatrix} \mathbf{1}_k^T$$

Let $X_{dr}^{G} \approx X_{vcs}^{DR}$ so that

$$X_{vcs}^{DR} \approx Q_{(\beta)}^{T} X_{dr} - \begin{bmatrix} -w_2 \\ \\ v_2 \end{bmatrix} \mathbf{1}_k^T$$

$$X_{vcs}^{DR} \approx Q_{(-\beta)} X_{dr} - \begin{bmatrix} -w_2 \\ \\ v_2 \end{bmatrix} \mathbf{1}_k^T$$

where $Q_{(\beta)}^{T} = Q_{(-\beta)}$ i.e. a clockwise rotation at an angle β is equivalent to a counter-clockwise rotation at an angle $-\beta$. The least squares estimation problem becomes

$$-\widetilde{\beta}, -\widetilde{w}_2, \widetilde{v}_2 = \underset{-\beta, -w_2, v_2}{\operatorname{argmin}} \left\| X_{vcs}^{DR} - \left(Q_{(-\beta)} X_{dr} - \begin{bmatrix} -w_2 \\ \\ v_2 \end{bmatrix} \mathbf{1}_k^T \right) \right\|_F^2 \tag{4.6}$$

The inclusion of the negative signs on the parameters formats the problem in the form provided in (4.1) so that the solution is provided as:

$$-\widetilde{\beta} = \textsc{Kabsch}\big(X_{vcs}^{DR}, X_{dr}, \texttt{rotation}\big)$$

$$\begin{bmatrix} -\widetilde{w}_2 \\ \\ \widetilde{v}_2 \end{bmatrix} = \textsc{Kabsch}\big(X_{vcs}^{DR}, X_{dr}, \texttt{translation}\big)$$

which, by resolving the negative signs, can be written as:

$$\widetilde{\beta} = -\textsc{Kabsch}\big(X_{vcs}^{DR}, X_{dr}, \texttt{rotation}\big) \tag{4.7}$$

$$\begin{bmatrix} \widetilde{w}_2 \\ \\ \widetilde{v}_2 \end{bmatrix} = \begin{bmatrix} -1 & 0 \\ \\ 0 & 1 \end{bmatrix} \textsc{Kabsch}\big(X_{vcs}^{DR}, X_{dr}, \texttt{translation}\big) \tag{4.8}$$

The estimate refinement methods described for the passenger radar side will also be used. Again, let there be n point set observations, $X_{vcs(i)}^{DR}$ be the ith set containing the locations of the CRs in the VCS and $X_{dr(i)}$ be the ith set containing the driver radar detections of the CRs. The estimates are refined as follows:

4.5.2.1 Refinement by averaging multiple estimates (DR side)

Like (4.7) and (4.8), the ith one-time estimates of the parameters are:

$$\widetilde{\beta}_i = -\textsc{Kabsch}\big(X_{vcs(i)}^{DR}, X_{dr(i)}, \texttt{rotation}\big)$$

$$\begin{bmatrix} \widetilde{w}_{2_i} \\ \\ \widetilde{v}_{2_i} \end{bmatrix} = \begin{bmatrix} -1 & 0 \\ \\ 0 & 1 \end{bmatrix} \textsc{Kabsch}\big(X_{vcs(i)}^{DR}, X_{dr(i)}, \texttt{translation}\big)$$

The refined estimate for each parameter is the average of n estimates,

$$\left[\widehat{\beta},\, \widehat{w}_2,\, \widehat{v}_2\right] = \frac{1}{n}\sum_{i=1}^{n}\left[\widetilde{\beta}_i\, \widetilde{w}_{2_i},\, \widetilde{v}_{2_i}\right]$$

with the expression taken to be an element-wise operation.

4.5.2.2 Refinement based on global estimation (DR side)

Like the passenger side, let two large sets be populated as follows:

$$X^{DR}_{vcs_{all}} = \left[X^{DR}_{vcs(1)},\ X^{DR}_{vcs(2)},\ \ldots,\ X^{DR}_{vcs(n)}\right] \in \mathbb{R}^{2\times kn}$$
$$X_{dr_{all}} = \left[X_{dr(1)},\ X_{dr(2)},\ \ldots,\ X_{dr(n)}\right] \in \mathbb{R}^{2\times kn}$$

so that the parameters can be estimated globally as

$$-\widehat{\beta}_g, -\widehat{w}_{2_g}, \widehat{v}_{2_g} = \underset{-\beta,-w_2,v_2}{\operatorname{argmin}} \left\| X^{DR}_{vcs_{all}} - \left(Q_{(-\beta)}X_{dr_{all}} - \begin{bmatrix} -w_2 \\ \\ v_2 \end{bmatrix} \mathbf{1}^T_{kn}\right)\right\|^2_F$$

using Algorithm 7. The estimates, after resolving the negative signs, are:

$$\widehat{\beta}_g = -\textsc{Kabsch}\big(X^{PR}_{vcs_{all}}, X_{pr_{all}}, \texttt{rotation}\big)$$

$$\begin{bmatrix} \widehat{w}_{2_g} \\ \widehat{v}_{2_g} \end{bmatrix} = \begin{bmatrix} -1 & 0 \\ 0 & 1 \end{bmatrix} \textsc{Kabsch}\big(X^{PR}_{vcs_{all}}, X_{pr_{all}}, \texttt{translation}\big)$$

Again, the subscript g on the estimates denotes that the estimation was performed *globally*.

We have obtained all **six estimates** with respect to each refinement method. Let the estimates be referred to as:

(a) *Averaged estimates*: $\widehat{\alpha},\ \widehat{\beta},\ \widehat{w}_1,\ \widehat{w}_2,\ \widehat{v}_1,\ \widehat{v}_2$ and

(b) *Global estimates*: $\widehat{\alpha}_g,\ \widehat{\beta}_g,\ \widehat{w}_{1_g},\ \widehat{w}_{2_g},\ \widehat{v}_{1_g},\ \widehat{v}_{2_g}$.

Corner reflectors in the overlapping field of view of both radars

If the k CRs are placed in the overlapping field of view of the two radars such that the reflectors are all detected by both radars, then the set containing the known locations of the CRs in the VCS used for the PR side can also be used for the DR side i.e. $X^{PR}_{vcs} = X^{DR}_{vcs}$. The calibration of the radars are still independent. While this may

seem like a more convenient choice in placing the reflectors, the caveat is that radar detections tend to be more accurate near the boresight [60]. The user should consider this when deciding the placement of the reflectors.

4.6 Results and Discussion

The results for both *averaged estimates* and *global estimates* will be presented. Unlike the *global estimate* of a parameter, the *averaged estimate* is obtained by taking the mean of n estimates. Statistically, estimates with lesser variability result in a higher confidence than those with a higher variability. Therefore, let us consider the spread of the multiple estimates, which are averaged, using the margin of error statistic to determine the confidence interval of the *averaged estimate*.

If $\widetilde{x}_i$ is the ith estimate of a parameter, and $\widehat{x}$ is the *averaged estimate*,

$$\widehat{x} = \frac{1}{n}\sum_{i=1}^{n}\widetilde{x}_i$$

the **margin of error** at 95% confidence is defined [61] as

$$e_{95} = t_{n-1}\frac{s}{\sqrt{n}} \tag{4.9}$$

where s is the sample standard deviation of the n estimates, and t_{n-1} is obtained

from the two-tail t-distribution table at $n-1$ degree of freedom. This means that the underlying true parameter x is contained in the interval $\widehat{x} \pm e_{95}$ with 95% statistical confidence.

4.6.1 Synthetic Data Results

This section presents some results from the calibration algorithm based on data simulation. The simulation was performed in MATLAB R2020a [62].

We simulate the two-radar geometry illustrated in Figure 4.1. Each radar is simulated to have a 120° field of view (FoV). The synthetic radar detections are generated as described in Algorithm 8. The four point sets X_{vcs}^{PR}, X_{vcs}^{DR}, X_{pr}, X_{dr} are noisy measurements of the true sets $X_{vcs_{truth}}^{PR}$, $X_{vcs_{truth}}^{DR}$, $X_{pr_{truth}}$, $X_{dr_{truth}}$ respectively, where N_{vcs}^{PR}, N_{vcs}^{DR}, N_{pr}, and N_{pr} are additive white Gaussian noises.

The noise matrices are zero-mean. Their covariances were chosen as follows:

$$\text{cov}\left(N_{vcs}^{PR}\right) = \text{cov}\left(N_{vcs}^{DR}\right) = \begin{bmatrix} 0.01^2 & 0 \\ 0 & 0.01^2 \end{bmatrix} m^2$$

gives the statistics of the error which the user makes in measuring the locations of the CRs in the VCS. The standard deviation in each dimension is $1cm$. This means that the user makes up to $2cm$ error in measurement (two standard deviations) at

Algorithm 8 Generation of the synthetic radar detections

Choose $X_{pr_{truth}}$
▷ Error-free locations of k CRs in the PR coordinate system
for $i = 1 : n$ **do**
    Let $X_{dr_{truth}} \coloneqq X_{pr_{truth}}$
    ▷ Error-free locations of k CRs in the DR coordinate system
    Obtain $X^{PR}_{vcs_{truth}}$ by transforming $X_{pr_{truth}}$ onto VCS
    ▷ True locations of the CRs in the VCS with respect to the PR
    Obtain $X^{DR}_{vcs_{truth}}$ by transforming $X_{dr_{truth}}$ onto VCS
    ▷ True locations of the CRs in the VCS with respect to the DR
    THE NOISY SETS:
    $X^{PR}_{vcs} \leftarrow X^{PR}_{vcs_{truth}} + N^{PR}_{vcs}$
    $X^{DR}_{vcs} \leftarrow X^{DR}_{vcs_{truth}} + N^{DR}_{vcs}$
    $X_{pr} \leftarrow X_{pr_{truth}} + N_{pr}$
    $X_{dr} \leftarrow X_{dr_{truth}} + N_{dr}$
    ▷ New reflector locations for the next iteration
    $X_{pr_{truth}} \leftarrow X_{pr_{truth}} + D$
end for

about 95% of the time. We expect industrial measurement tools to achieve smaller error. Also,

$$\mathrm{cov}\left(N_{pr}\right) = \mathrm{cov}\left(N_{dr}\right) = \begin{bmatrix} 0.02^2 & 0 \\ 0 & 0.02^2 \end{bmatrix} m^2$$

gives the statistics of the radar detection error. The $2cm$ standard deviation in each dimension means that each radar makes up to $4cm$ error in detection (two standard deviations) at about 95% of the time. This value is chosen based on the $4cm$ approximate range resolution of a typical automotive radar, whose FMCW chirp sweeps up to $4GHz$ bandwidth.

Corner reflectors are required to be moved after each data collection procedure in

order to obtain multiple observations, which are needed for the estimate refinement process. We simulate the movement of the reflectors by adding a displacement matrix $D \sim \mathcal{N}\big(\mathbf{0},\, K_D\big)$ of an appropriate size to $X_{pr_{truth}}$ in Algorithm 8 (i.e. $X_{pr_{truth}} \leftarrow X_{pr_{truth}} + D$), so that the reflectors have new locations at the next loop iteration. The covariance matrix for the displacement matrix statistics is chosen as

$$K_D = \begin{bmatrix} 0.3^2 & 0 \\ 0 & 0.3^2 \end{bmatrix} m^2 \ .$$

The points in the initial set $X_{pr_{truth}}$ (line 1 of Algorithm 8) are chosen randomly within ranges $1m$ and $6m$ in the radar's FoV. Also, the points in $X_{pr_{truth}}$ (line 10) are constrained in the bounds such that if the addition of D results in one or more points to be moved or displaced outside the bounds, the algorithm undoes the displacement of the affected points and re-samples a new displacement matrix, of the appropriate size, from the distribution to be added to the affected points until all the points are located within the bounds.

The estimation procedure follows from the above information. We chose the true parameters to be estimated as:

$$\alpha = 40^\circ,\ \beta = 40^\circ$$

$$w_1 = 0.6m,\ w_2 = 1.0m,\ v_1 = 0.3m,\ v_2 = 0.4m$$

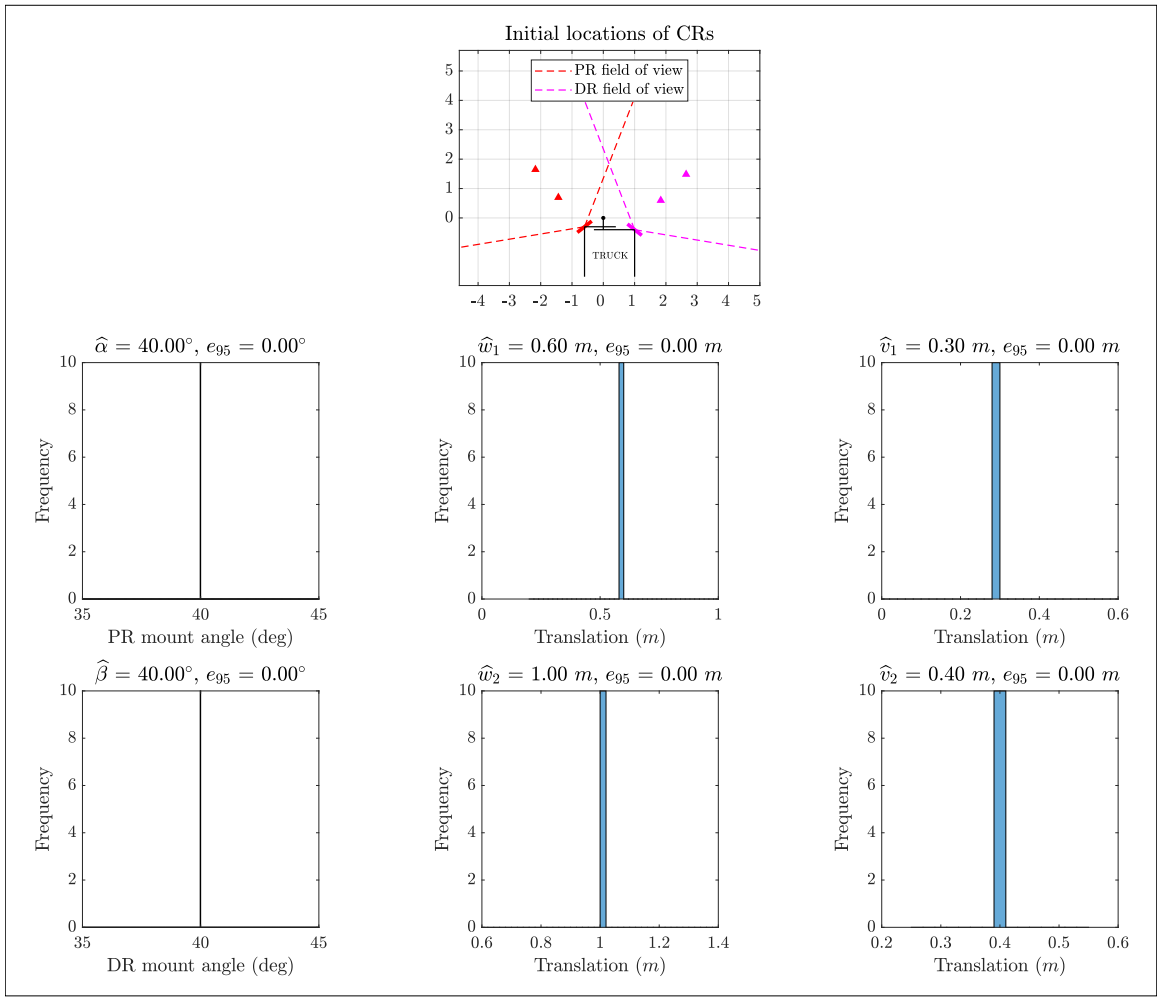

Figure 4.5: Noiseless synthetic data: *Averaged estimates* with $k = 2$ reflectors.

To test the algorithm, we set all the four Gaussian noises in Algorithm 8 to zero to make **noiseless synthetic data**. The reflectors were not moved for the test i.e. D is a zero matrix. The *averaged estimates* obtained with the noiseless data sets are presented in Figure 4.5, for $k = 2$ reflectors. The top-most subplot, in the figure, gives an illustration of the two-radar geometry in which the CRs are placed in the FoV of each radar, the origin of the subplot is at G. Each of the remaining six subplots is an histogram of n parameter estimates. The *average estimate* of a parameter and its

margin of error with 95% confidence are provided at the top of each histogram[1]. It can be observed from the histograms that the algorithm returned the exact values of the six parameters for all $n = 10$ observations. The *global estimates* are also obtained to be exact values of the six parameters. This test confirms that the algorithm produces correct locations with noiseless data.

Following the confirmation, we sample the noise from the covariance matrices to make **noisy synthetic data**. The displacement matrix D is also sampled from its distribution and used to simulate the movement of the CRs, as described earlier. The *averaged estimates* obtained from 10 observations are presented with varying values of k (the number of CRs) in Figure 4.6. The same results are summarized in Table 4.1(a) sectioned under the $n = 10$ header. It can be observed from the figure and table that the mount angle estimates for $k = 2$ have the most error margins, which translates to the largest sample standard deviations based on the direct proportionality in (4.9), when compared with those for which $k = 3, 4, 5$. The *global estimates* are provided in Table 4.1(b). It can be observed from both tables that the two refinement methods provide comparable estimates.

[1]The descriptions of the subplots in Figure 4.5 applies to each subfigure in Figures 4.6, 4.8 and 4.10.

Table 4.1
Estimation results from the noisy synthetic data
(a) *Averaged estimates* based on n observations

	$n = 10$								$n = 1000$	
	$k = 2$		$k = 3$		$k = 4$		$k = 5$		$k = 3$	
	AVG.	e_{95}	AVG.	e_{95}	AVG.	e_{95}	AVG.	e_{95}	AVG.	e_{95}
$\widehat{\alpha}$ (°)	**40.02**	1.07	**40.06**	0.48	**39.85**	0.21	**40.01**	0.33	**39.99**	0.03
$\widehat{\beta}$ (°)	**40.26**	1.00	**39.79**	0.38	**40.12**	0.28	**39.88**	0.24	**40.01**	0.03
$\widehat{w}_1$ (m)	**0.59**	0.04	**0.60**	0.01	**0.61**	0.02	**0.60**	0.02	**0.60**	0.00
$\widehat{w}_2$ (m)	**0.99**	0.03	**1.00**	0.02	**1.00**	0.01	**1.00**	0.01	**1.00**	0.00
$\widehat{v}_1$ (m)	**0.30**	0.01	**0.29**	0.02	**0.30**	0.01	**0.30**	0.02	**0.30**	0.00
$\widehat{v}_2$ (m)	**0.39**	0.03	**0.41**	0.01	**0.39**	0.02	**0.40**	0.01	**0.40**	0.00

(b) *Global estimates* based on n observations

	$n = 10$				$n = 1000$
	$k = 2$	$k = 3$	$k = 4$	$k = 5$	$k = 3$
$\widehat{\alpha}_g$ (°)	**40.06**	**39.94**	**39.85**	**40.03**	**39.98**
$\widehat{\beta}_g$ (°)	**40.06**	**39.84**	**40.06**	**39.89**	**40.01**
$\widehat{w}_{1_g}$ (m)	**0.59**	**0.60**	**0.61**	**0.60**	**0.60**
$\widehat{w}_{2_g}$ (m)	**1.00**	**1.00**	**1.00**	**1.00**	**1.00**
$\widehat{v}_{1_g}$ (m)	**0.30**	**0.30**	**0.30**	**0.29**	**0.30**
$\widehat{v}_{2_g}$ (m)	**0.40**	**0.41**	**0.40**	**0.40**	**0.40**

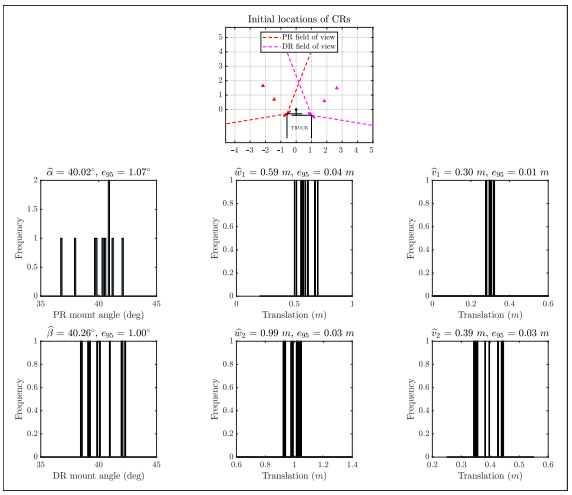

(a) $k = 2$

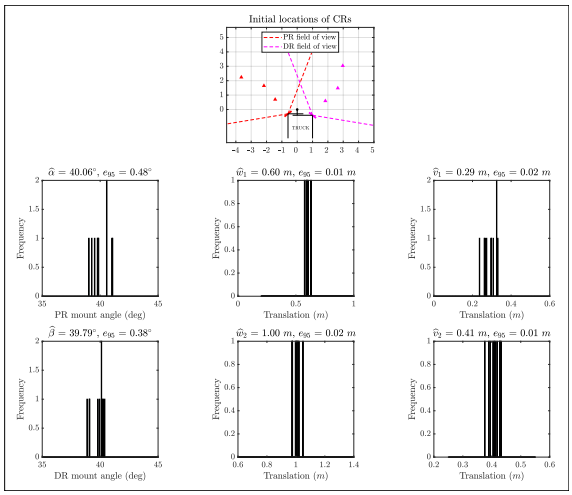

(b) $k = 3$

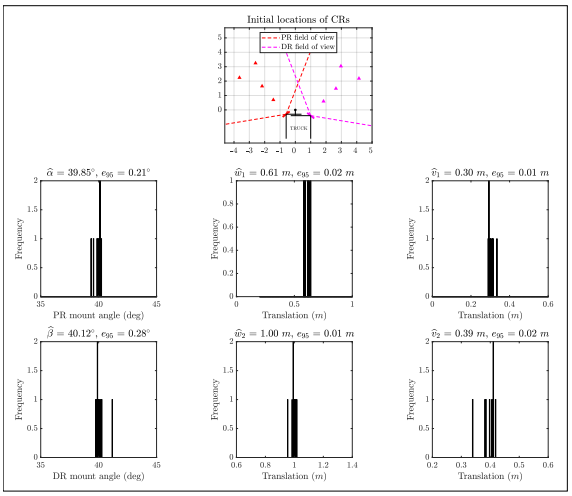

(c) $k = 4$

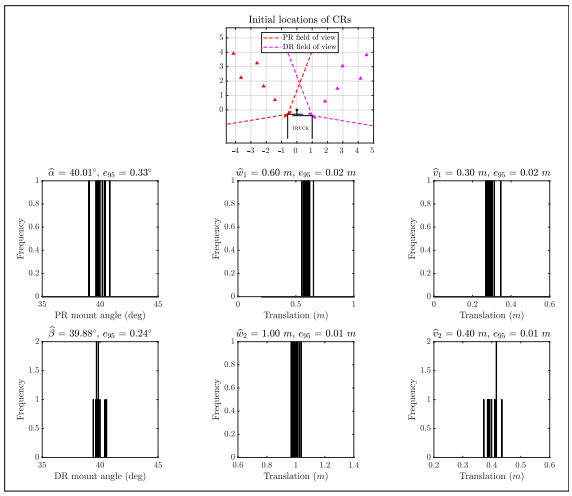

(d) $k = 5$

Figure 4.6: Noisy synthetic data: *Averaged estimates* with the number of corner reflectors, k varied. The number of observations $n = 10$.

We proceed to show that if the number of observations n is large, then the estimator appears to become more accurate. Figure 4.7 presents the root mean square error (RMSE) performance of the estimates, where the functions in the legend of each subfigure are defined with respect to the *averaged estimates* as:

$$\text{rmse}_{(\widehat{\alpha},\widehat{\beta})} = \left(\frac{1}{2} \left\| \begin{bmatrix} \alpha \\ \beta \end{bmatrix} - \begin{bmatrix} \widehat{\alpha} \\ \widehat{\beta} \end{bmatrix} \right\|^2 \right)^{\frac{1}{2}} \quad deg.\ (^\circ)$$

$$\text{rmse}_{(\widehat{w}_1,\widehat{w}_2,\widehat{v}_1,\widehat{v}_2)} = \left(\frac{1}{4} \left\| \begin{bmatrix} w_1 \\ w_2 \\ v_1 \\ v_2 \end{bmatrix} - \begin{bmatrix} \widehat{w}_1 \\ \widehat{w}_2 \\ \widehat{v}_1 \\ \widehat{v}_2 \end{bmatrix} \right\|^2 \right)^{\frac{1}{2}} \quad m$$

and likewise with respect to the *global estimates* as:

$$\text{rmse}_{(\widehat{\alpha}_g,\widehat{\beta}_g)} \quad \textit{and} \quad \text{rmse}_{(\widehat{w}_{1_g},\widehat{w}_{2_g},\widehat{v}_{1_g},\widehat{v}_{2_g})}\,.$$

The figure contains four log-log plots based on the number of reflectors $k = 2, 3, 4, 5$. Each plot shows the RMSE values of the estimates as the number of observations n increases from 1 to 1000. The high value of n is set for theoretical analysis, not for practical situations. It can be seen from the trends of all four plots that the

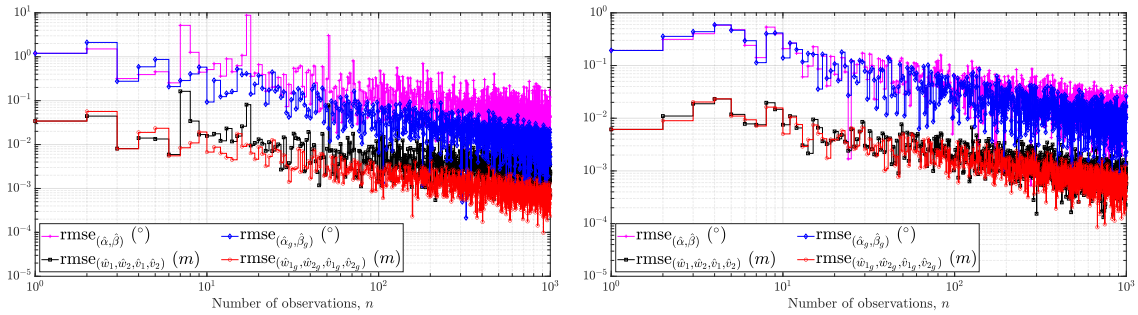

(a) $k = 2$ **(b)** $k = 3$

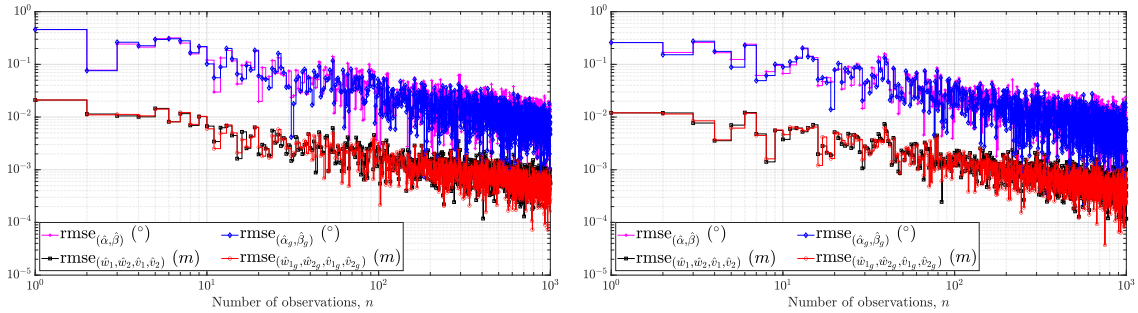

(c) $k = 4$ **(d)** $k = 5$

Figure 4.7: Noisy synthetic data: Each subfigure is a log-log plot showing the root mean square error (**RMSE**) values of both *averaged estimates* and *global estimates* for different number of corner reflectors, as the number of observations increase from $n = 1$ to $n = 1000$.

RMSE values for the mount angle estimates and the RMSE values for the translation parameter estimates appear to reduce as n increases. Hence, the estimates tend to become more accurate as the number of observations increase. At $k = 2$, the RMSE values of the *global estimates* appear to decay faster than the RMSE values of the *averaged estimates*. However, at $k = 3, 4, 5$ the RMSE values for both refinement methods appear to decay comparably.

The distribution of the *averaged estimates*, for $k = 3$ reflectors and $n = 1000$ observations, is presented in Figure 4.8. The *averaged estimates* and *global estimates* for

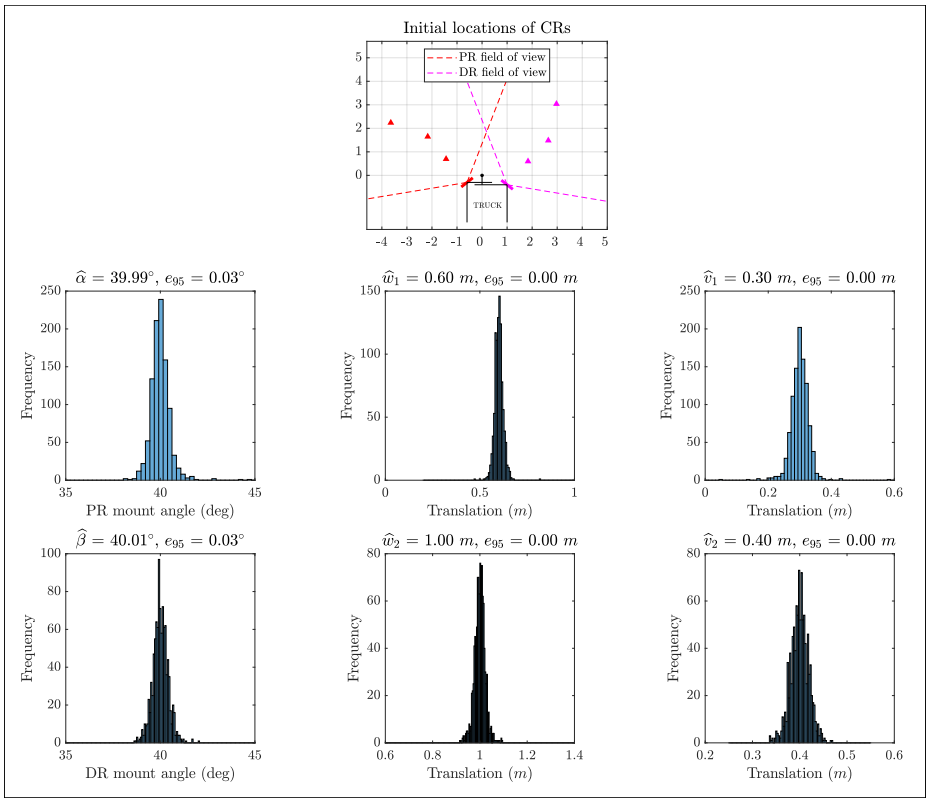

Figure 4.8: Noisy synthetic data: *Averaged estimates* with $k = 3$ reflectors, $n = 1000$.

the same n and k values are summarized in Table 4.1 under the $n = 1000$ headers. It can be observed from the figure (taking note of the very small margins of error; the e_{95} values) and tables (in Table 4.1) that the estimates of all the six parameters approach their true values as the number of observations increase. However, there is a trade-off in increasing n for estimation precision since it would increase the work needed to be done in moving the reflectors.

4.6.2 Experimental Data Results

We are going to present the results obtained from testing the algorithm with experimental radar data. Based on the experimental apparatus shown in Figure 4.2, we let G be the location of the hitch ball. The true parameters to be estimated are determined from the geometry of the apparatus, they are:

$$\alpha = 19.0^\circ,\ \beta = 20.0^\circ$$

$$w_1 = w_2 = 0.8m, \qquad v_1 = v_2 = 0.32m$$

The radar mount angles α, β were read from the protractors (installed on the apparatus as described in the figure) and the translation parameters w_1, w_2, v_1, v_2 were obtained with a meter rule. We placed three CRs ($k = 3$) in the PR field of view as shown in Figure 4.9. The reflectors' locations in the VCS were recorded. The radar detections of the reflectors were also saved. We then moved the reflectors manually in a random manner and repeated the process to obtain 10 different sets of data at the PR side ($n = 10$). The same procedure was performed at the DR side to also obtain 10 different sets of data. The data obtained from both radar sides were used to estimate the parameters as described in section 4.5. The *averaged estimates* are presented in Figure 4.10 and summarized in Table 4.2(a), which includes the 10 one-time estimates that are averaged. The *global estimates* are provided in Table 4.2(b).

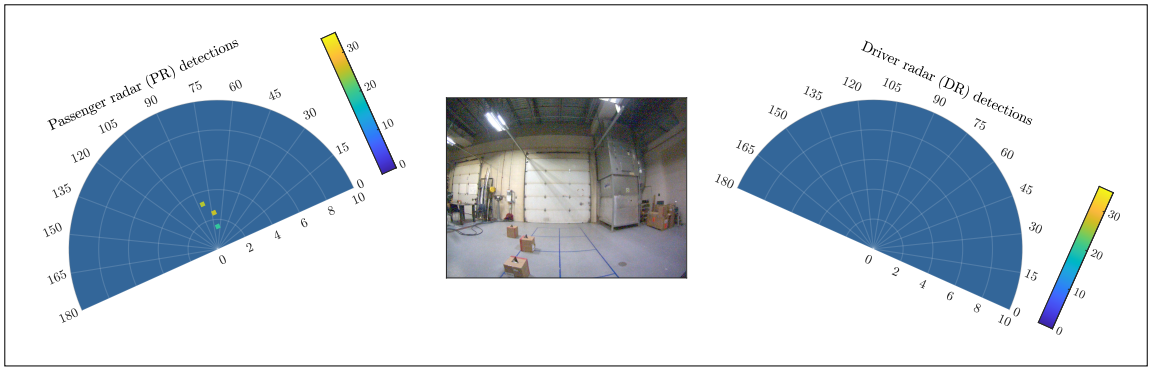

(a) Corner reflectors in the passenger radar's FoV

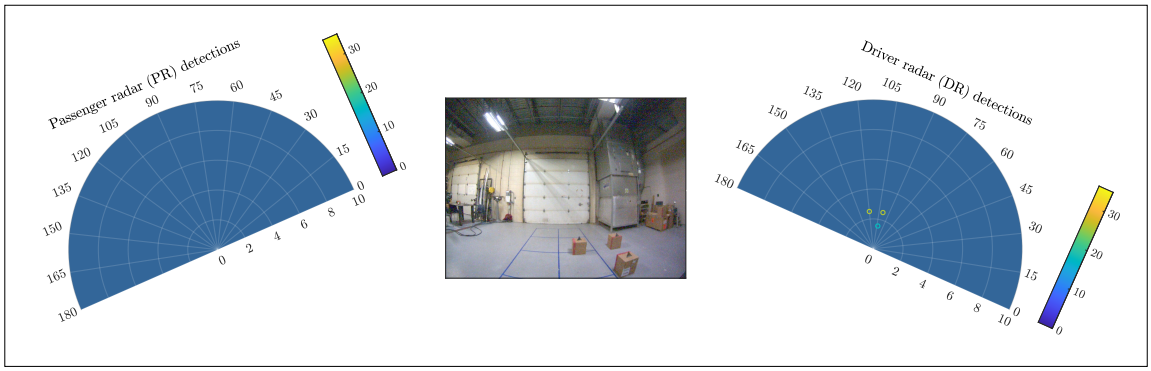

(b) Corner reflectors in the driver radar's FoV

Figure 4.9: Three corner reflectors (on top of boxes) were placed in each radar's FoV. The locations of the reflectors were known in the VCS (in this experiment, the origin of the VCS is the hitch ball location). An empty radar detection in each subfigure indicates that no corner reflector was present in the radar's FoV. The experiment in subfigure (a) provides estimates for parameters α, w_1, and v while that in subfigure (b) provides estimates for parameters β, w_2, and v. The clutter detections in the subfigures were removed. This will not be necessary in a controlled environment.

The results show that the mount angle estimates, with respect to both refinement methods, are within 0.35° range of the ground truth, while the translation parameter estimates are all within $0.01m$ range of the ground truth. While the results presented are based on our experiment, the user should note that the accuracy of the estimates depends on the accuracy of the radar detections and the precision in measuring the reflector locations in the VCS.

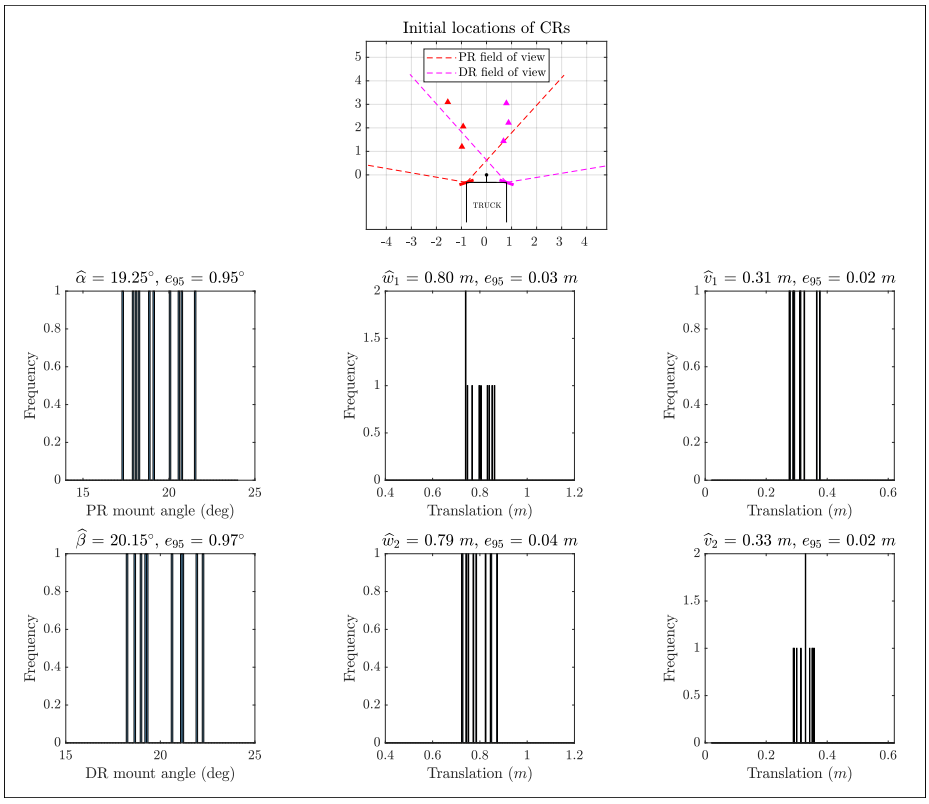

Figure 4.10: Radar data: *Averaged estimates* with $k = 3$ reflectors, $n = 10$.

With respect to both synthetic and experimental radar data results, the estimates obtained from using the two refinement methods seem to be comparable. However, the refinement procedures have different computational requirements. The *averaged estimates* require Algorithm 7 to be run n times for all observations, while the *global estimates* are obtained by running the algorithm once.

Table 4.2
Estimation results from the radar data, $k = 3$

(a) *Averaged estimates* based on $n = 10$ observations

One-time Estimates											Average		e_{95}
$\widetilde{\alpha}$ (°)	18.07	20.07	17.94	18.88	17.31	20.72	18.28	19.12	21.56	20.54	$\widehat{\alpha}$ (°)	**19.25**	0.95
$\widetilde{\beta}$ (°)	19.35	20.58	19.22	21.10	21.21	21.92	18.65	22.24	19.00	18.20	$\widehat{\beta}$ (°)	**20.15**	0.97
$\widetilde{w}_1$ (m)	0.84	0.81	0.86	0.83	0.85	0.74	0.80	0.77	0.75	0.74	$\widehat{w}_1$ (m)	**0.80**	0.03
$\widetilde{w}_2$ (m)	0.85	0.78	0.74	0.75	0.77	0.73	0.85	0.72	0.82	0.87	$\widehat{w}_2$ (m)	**0.79**	0.04
$\widetilde{v}_1$ (m)	0.31	0.29	0.29	0.37	0.38	0.28	0.31	0.33	0.28	0.29	$\widehat{v}_1$ (m)	**0.31**	0.02
$\widetilde{v}_2$ (m)	0.35	0.33	0.34	0.35	0.29	0.30	0.33	0.31	0.29	0.36	$\widehat{v}_2$ (m)	**0.33**	0.02

(b) *Global estimates* based on $n = 10$ observations

$\widehat{\alpha}_g$	$\widehat{\beta}_g$	$\widehat{w}_{1_g}$ (m)	$\widehat{w}_{2_g}$ (m)	$\widehat{v}_{1_g}$ (m)	$\widehat{v}_{2_g}$ (m)
19.33	**19.72**	**0.79**	**0.81**	**0.31**	**0.33**

4.7 Conclusion

We have shown that the mount angle of a radar and the translation vector needed to transform detections onto a vehicle coordinate system (VCS) can be estimated by comparing the radar's detections of objects, such as corner reflectors, with the known locations of the objects in the VCS. The required known locations of the objects are not defined with respect to the radar, but the VCS, which is an advantage since a radar installed behind a radome is not easily accessible. Multiple estimates are obtained and refined based on multiple data observations. Two refinement methods are provided; averaging the estimates and performing a global estimation on combined data observations. The results obtained from testing the calibration method on synthetic and radar data, with respect to both refinement methods, suggest that the algorithm is a feasible tool for extrinsic calibration of automotive radars.

Chapter 5

Extrinsic Radar Calibration with Overlapping FoV and Hitch Ball Position Estimation

5.1 Chapter abstract

Sensor fusion, in many perception algorithms, requires the detections from multiple sensors to be transformed onto a common coordinate system (CCS) for joint processing. The position and orientation of the sensors need to be determined for

The material contained in this chapter is in preparation for submission to a journal. The work was supported by the Ford Motor Company as an Alliance Project under Ford/MTU Master Agreement #83437205.

the fusion procedure. Two automotive blind spot information (BSI) radar sensors are considered in this work and their orientation is defined with respect to the straight line connecting them. We estimate the rotation and translation parameters which are needed to transform the detections from the radars onto a CCS whose origin is at the hitch ball of a truck. This CCS is a convenient choice for algorithms which use BSI radars to monitor or sense the rotation of an attached trailer about the hitch ball. The estimation is performed by rotating a trailer or a pivoting platform (upon which corner reflectors are placed) about the hitch ball in the direction of both radars. The algorithm is based on two principles: (1) the use of common detections found in the overlapping field of view of the radars to estimate the rotation parameters and (2) a search for the center of trailer or platform rotation to determine the translation parameters which define the hitch ball position relative to the radars. The experimental results obtained, based on the data collected, suggest that the algorithm is feasible for deployment.

5.2 Introduction

Multiple sensors are often fused for combined measurements. This is seen in perception and multi-sensor applications. A common task for the fusion procedure is to rigidly transform detections from the individual sensor coordinates onto a conveniently chosen common coordinate system (CCS) based on knowing the location and

orientation of the sensors. Hence, an accurate representation of sensor measurements in the CCS depends on the use of optimal parameters for the transformation. The determination of the transformation parameters in a sensor network is referred to as extrinsic calibration, while intrinsic calibration is concerned with the internal working parameters of the sensor.

Some existing calibration methods have been proposed for different sensors; for cameras in [38, 39], for lidar and camera in [40–42], for laser scanner and camera in [43–46], for radar and camera in [63–65], and for radar, lidar, and camera in [66, 67]. Like in [49–51, 68], radar sensors only are considered for the calibration in this work.

We present an extrinsic calibration method for two automotive radars installed in the tail light fixtures of a truck as illustrated in Figure 5.1, and assume that intrinsic calibration has been performed. Each radar is installed such that its boresight is at an angle away from the truck's longitudinal line, like it is often done for blind spot applications. We estimate the parameters needed to rigidly transform the detections from both radars onto a CCS whose origin is the hitch ball; the parameters are in terms of rotation (due to the radar's orientation) and translation. This CCS is a convenient choice for algorithms which monitor or sense the rotation of a trailer attached to the hitch ball, using sensors such as blind spot information radars.

The estimation procedure requires a trailer or a pivoting platform, on which corner reflectors (CRs) are placed, to be rotated about the hitch ball. The detections from

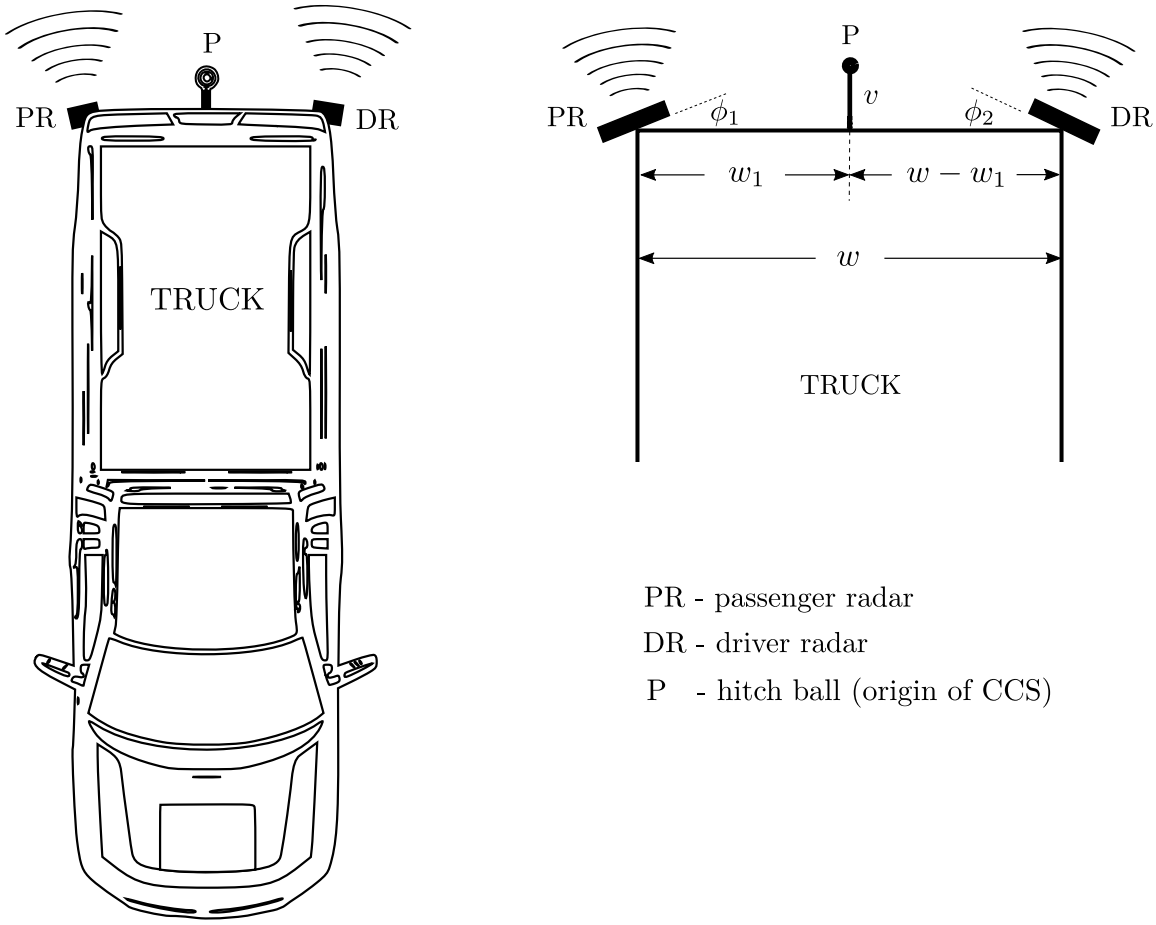

Figure 5.1: *Left*: A diagram of a truck showing two blind spot information radars and the hitch ball. *Right*: A schematic diagram of the two-radar geometry with respect to the hitch ball. Four parameters ϕ_1, ϕ_2, w_1, and v will be estimated. [1]The distance between the radars, w is known. The **rotation angle parameters** ϕ_1, ϕ_2 are defined with respect to the line connecting the radars. The **translation parameters** are w_1, v; where v is the perpendicular distance of the hitch ball to the line connecting the radars, intersecting the line at a distance of w_1 away from the passenger radar. Meanwhile, w_1 is not necessarily an exact half of w depending on the locations of the radars.

CRs found in the overlapping field of view (FoV) of the radars are used to estimate the rotation parameters, while the transformation parameters are estimated by finding the center of trailer rotation, the hitch ball position. Many camera-based sensor fusion

[1]An analysis which supports the requirement for w to be known is provided in Appendix A.

methods have used the overlapping FoV concept for calibration in the literature, some methods are presented in [69–75]. It was also considered in [51, 68] to remove alignment errors from two 3D radars using the objects that are tracked by both sensors.

This paper is arranged as follows: section 5.3 contains the problem statement and a description of the experimental apparatus, the calibration method is presented in section 5.4, results are provided and discussed in section 5.5, and the conclusion in section 5.6. These are the general notations used: $\boldsymbol{y}$ in bold lower case is a column vector, Y in upper case is a matrix, and ^{T} represents a transpose operation.

5.3 Problem Statement and Experimental Apparatus

5.3.1 Problem Statement

The objective of this work is to estimate the **rotation angle parameters** ϕ_1, ϕ_2, due to the orientation of the radars, and the **translation parameters** w_1, v with respect to the geometry illustrated in Figure 5.1 using the detections from the passenger radar (PR) and the driver radar (DR). The rotation angle parameters are defined

Figure 5.2: *Left*: The experimental apparatus (truck mock-up) used for radar data collection. Each of the two **radars** (encircled) is installed on a plexiglass. A **protractor**, locked to the top of each plexiglass, provides the ground truth of the rotation angle which will be estimated. A rear gate **camera** (in square bounds) was also installed on the mock-up for visualization of the procedure, it was not used for the calibration. *Right*: A calibration scenario where corner reflectors were placed on a trailer attached to the truck.

with respect to the line which connects both radars. The line is parallel to the truck's lateral line if the radar positions on the truck are symmetric. Each radar provides detections in two dimensions; range and azimuth. The parameter estimates will be used to rigidly transform the detections onto the chosen CCS, whose origin is the hitch ball.

5.3.2 Experimental Apparatus

The apparatus used in this work for data collection consists of a truck's rear gate mounted on a three-wheel platform as shown in Figure 5.2. It will be referred to as a truck mock-up. The rotation of the trailer about the hitch ball, during the calibration

process, was simulated by rotating the truck mock-up instead, while the trailer was kept stationary. This helped to prevent the truck-mockup from being displaced. Therefore, the trailer's rotation described in this work refers to this procedure. Two automotive radars were installed at the sides of the truck mock-up. We used the TI AWR1642BOOST radar module [25], which has 2 transmit and 4 receive elements. The radar provides point detections in range and azimuth. It operates in the $76-81$GHz frequency band, and uses up to 4GHz bandwidth for its frequency-modulated continuous-wave (FMCW) waveform. The waveform used in this work has a range resolution of about $4.1cm$ and a maximum range of about $6.5m$. To reject as much clutter as possible, we set the constant false alarm rate (CFAR) range threshold of the detections to $15dB$. Both radars contain different oscillators and their operations are not synchronized, they are separately located. The waveform and the CFAR threshold provided are not guaranteed to be optimal in all situations, they were chosen based on our experiment and the workshop space used for the calibration. The CRs used in this work are $10dBsm$ trihedral.

5.4 Calibration Method

The calibration procedure can be simply described as follows. Let there be k corner reflectors (CRs) placed on either a trailer or a pivoting platform attached to the hitch ball as illustrated in Figure 5.3. The trailer or platform will be rotated in both

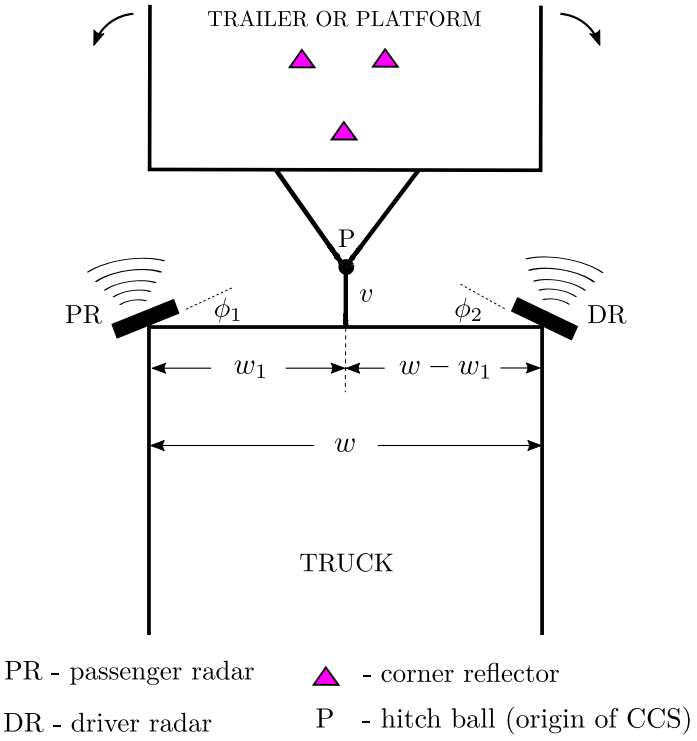

Figure 5.3: An illustration of the rotation of a trailer or platform (on which corner reflectors are placed in a pattern determined by the user) about the truck's hitch ball. The distance between the radars, w is known.

radar directions. As the trailer rotates, let us keep each radar's set of detections which contains all k reflectors. Let $X_i \in \mathbb{R}^{2\times k}$ and $Y_i \in \mathbb{R}^{2\times k}$ respectively be the ith detection sets provided by the passenger radar and driver radar respectively, during the trailer rotation.

The algorithm will estimate the four parameters (ϕ_1, ϕ_2, w_1, and v) based on two principles: (a) the detections of reflectors in the overlapping field of view (FoV) of both radars as the trailer rotates and (b) a search for the center of rotation, the hitch ball position.

Assumptions

The algorithm assumes the following:

1. The CCS has an origin at the hitch ball position and its horizontal axis is parallel to the straight line connecting the radars.

2. The distance between the two radars, width w is known. A simulation analysis which supports the requirement for this assumption is presented in Appendix A.

3. Both radar detection sets X_i and Y_i have correspondence. This means that the mth column vectors in the sets represent the detections of the mth reflector. This can be easily achieved by performing the calibration in a clutter-free environment.

The two estimation principles are presented as follows.

5.4.1 Principle 1: Detections in the overlapping field of view

Let us use subscript j on the point set variables in this section. Let the k CRs be located in the overlapping FoV region at an instance during the rotation of the trailer or platform, such that both radars **simultaneously** detect the reflectors as a pair of

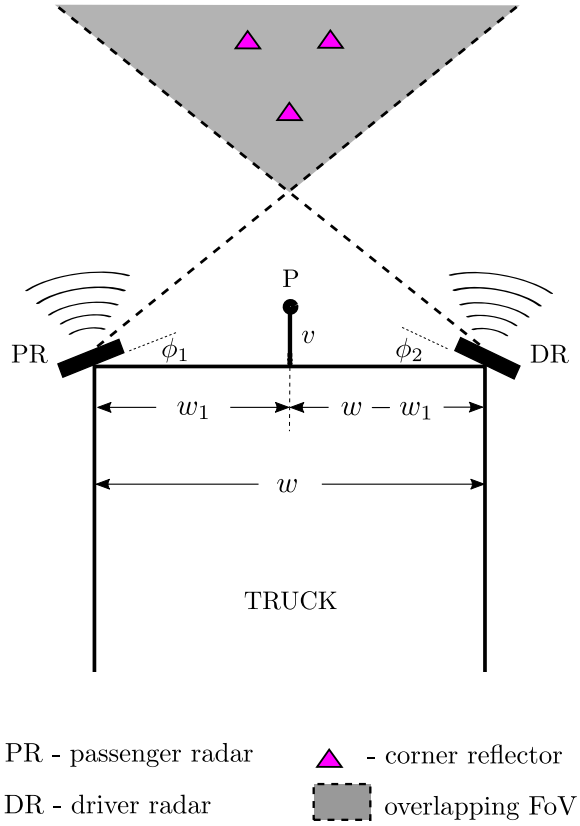

Figure 5.4: An illustration of corner reflectors in the overlapping field of view of both radars during trailer rotation (the trailer is not shown in this figure). The distance between the radars, w is known.

detection sets (X_j, Y_j). An illustration is provided in Figure 5.4. The algorithm will estimate the rotation angles based on the common detections.

Let

$$Q_{(\phi)} = \begin{bmatrix} \cos(\phi) & -\sin(\phi) \\ \sin(\phi) & \cos(\phi) \end{bmatrix}$$

be a two-dimensional rotation matrix which rotates a vector at an angle ϕ in the counter-clockwise direction for positive ϕ.

Let us transform the detection sets onto the CCS:

$$X_j^p = Q_{(\phi_1)} X_j - \begin{bmatrix} w_1 \\ \\ v \end{bmatrix} \mathbf{1}_k^T \tag{5.1}$$

$$\begin{aligned} Y_j^p &= Q_{(\phi_2)}^T Y_j - \begin{bmatrix} -(w - w_1) \\ \\ v \end{bmatrix} \mathbf{1}_k^T \\ &= Q_{(\phi_2)}^T Y_j + \begin{bmatrix} w - w_1 \\ \\ -v \end{bmatrix} \mathbf{1}_k^T \end{aligned} \tag{5.2}$$

where X_j^p and Y_j^p are the transformed PR and DR detections respectively, and $\mathbf{1}_k$ is a column vector of k ones. The estimation task is to find the parameters that achieve the approximation,

$$X_j^p \approx Y_j^p$$

$$Q_{(\phi_1)} X_j - \begin{bmatrix} w_1 \\ \\ v \end{bmatrix} \mathbf{1}_k^T \approx Q_{(\phi_2)}^T Y_j + \begin{bmatrix} w - w_1 \\ \\ -v \end{bmatrix} \mathbf{1}_k^T$$

since the detections from both radars represent the same spatial locations of the

reflectors in the CCS. The parameters will be estimated by minimizing the following:

$$\min \left\| \left(Q_{(\phi_1)} X_j - \begin{bmatrix} w_1 \\ \\ v \end{bmatrix} \mathbf{1}_k^T \right) - \left(Q_{(\phi_2)}^T Y_j + \begin{bmatrix} w - w_1 \\ \\ -v \end{bmatrix} \mathbf{1}_k^T \right) \right\|_F$$

$$= \min \left\| Q_{(\phi_1)} X_j - \left(Q_{(\phi_2)}^T Y_j + \begin{bmatrix} w \\ \\ 0 \end{bmatrix} \mathbf{1}_k^T \right) \right\|_F \tag{5.3}$$

$$\text{i.e.} \quad \underset{\phi_1, \phi_2}{\operatorname{argmin}} \left\| Q_{(\phi_1)} X_j - \left(Q_{(\phi_2)}^T Y_j + \begin{bmatrix} w \\ \\ 0 \end{bmatrix} \mathbf{1}_k^T \right) \right\|_F \tag{5.4}$$

where $\|.\|_F$ is the Frobenius norm. The translation parameters w_1 and v cancel in (5.3), therefore, they are **not observable**. Instead, the rotation angles ϕ_1 and ϕ_2 are observable and will be estimated.

Meanwhile, the estimation problem in (5.4) is based on one-time detection sets X_j and Y_j as illustrated with a minimal example in Figure 5.5. The one-time estimates are not guaranteed to be accurate due to the quantization of radar detections. Therefore, let us refine the estimates by using multiple detection sets. Let the total number of *unique* set pairs (X_j, Y_j) for which the radars simultaneously detect the reflectors in the overlapping FoV be n. *Uniqueness* means that duplicate set pairs have been

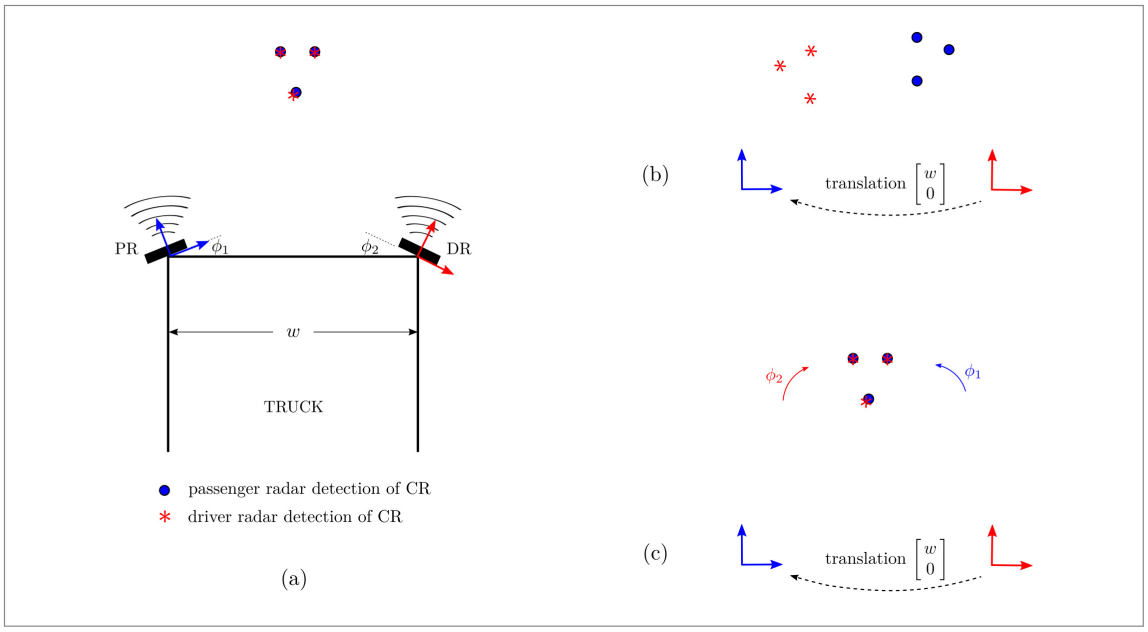

Figure 5.5: An illustration of the rotation angle estimation with a minimal example.

(a) Let there be three corner reflectors in the overlapping FoV of both radars i.e. $k = 3$. Let sets X_j and Y_j contain the passenger radar and driver radar detections, respectively.

(b) The two radar coordinate systems, where their horizontal axes are aligned with the line connecting the radars. Both coordinate systems are separated by the translation vector shown. Let us realign both point sets like the first subfigure.

(c) Estimate angles ϕ_1 and ϕ_2 which aligns $Q_{(\phi_1)}X_j$ (a counter-clockwise rotation of X_j in the PR coordinate system) and $Q^T_{(\phi_2)}Y_j + \begin{bmatrix} w \\ 0 \end{bmatrix} \mathbf{1}_k^T$ (a clockwise rotation of Y_j in the DR coordinate system followed by a translation onto the PR coordinate system), where $\mathbf{1}_k$ is a column vector of k ones.

removed. Let us populate each radar's detection sets for $j = 1 : n$ as:

$$X_{ofov} = \Big[X_1,\ X_2,\ \ldots,\ X_n\Big] \in \mathbb{R}^{2\times kn}$$

$$Y_{ofov} = \Big[Y_1,\ Y_2,\ \ldots,\ Y_n\Big] \in \mathbb{R}^{2\times kn}$$

where X_{ofov} and Y_{ofov} each contain n detections (i.e. observations) in the overlapping FoV, provided by the passenger radar and the driver radar respectively, as the trailer

rotates. Also, the two sets have correspondence based on the correspondence between sets X_j and Y_j. Hence, the problem in (5.4) can be extended with respect to all n observations as:

$$\widehat{\phi}_1, \widehat{\phi}_2 = \underset{\phi_1,\phi_2}{\operatorname{argmin}} \left\| Q_{(\phi_1)} X_{ofov} - \left(Q_{(\phi_2)}^T Y_{ofov} + \begin{bmatrix} w \\ \\ 0 \end{bmatrix} \mathbf{1}_{kn}^T \right) \right\|_F \tag{5.5}$$

$$\coloneqq \underset{\phi_1,\phi_2}{\operatorname{argmin}} \; f_{(\phi_1,\phi_2)} \tag{5.6}$$

where $\widehat{\phi}_1, \widehat{\phi}_2$ are the refined estimates of the rotation parameters and $f_{(\phi_1,\phi_2)}$ is the cost function. The minimization problem can be solved by fixing a value for ϕ_2 to make a constrained orthogonal Procrustes (CoP) problem [28][29].

When compared with (5.5), the CoP problem is of the form:

$$\acute{\phi}_1 = \underset{\phi_1}{\operatorname{argmin}} \left\| Q_{(\phi_1)} X_{ofov} - G \right\|_F \tag{5.7}$$

where $G \coloneqq Q_{(\phi_2)}^T Y_{ofov} + \begin{bmatrix} w \\ \\ 0 \end{bmatrix} \mathbf{1}_{kn}^T$ for a fixed value of ϕ_2. The solution to (5.7) is provided as function ProcrustesAngle in Algorithm 9. Hence, due to the convexity of the Frobenius norm, we solve (5.5) by combining a coarse-to-fine grid search over a range of values for ϕ_2 and a CoP solution for ϕ_1 as described in the EstRotAngles

Algorithm 9 Estimation of the rotation angle parameters

procedure ESTROTANGLES($X_{ofov}, Y_{ofov}, vecBnd, w$)
  while range($vecBnd$) $> \epsilon$ **do** ▷ We set $\epsilon = 10^{-6}$
    $\left\{\acute{\phi}_{2i}\right\}_{i=1}^{p} \leftarrow$ Split $vecBnd$ to p divisions
    ▷ We chose $p = 5$
    for $i = 1 : p$ **do**
      $G \leftarrow Q_{(\acute{\phi}_{2i})}^{T} Y_{ofov} + \begin{bmatrix} w \\ 0 \end{bmatrix} \mathbf{1}_{kn}^{T}$
      $\acute{\phi}_{1i} =$ PROCRUSTESANGLE(X_{ofov}, G)
      ▷ The **function** is provided below
      $fVal_i \leftarrow f_{(\acute{\phi}_{1i}, \acute{\phi}_{2i})}$ from (5.6)
    end for
    $\left[minVal,\ id\right] \leftarrow \min\left(\left\{fVal_i\right\}_{i=1}^{p}\right)$
    ▷ id is the index of the minimum value, $minVal$
    $vecBnd \leftarrow$ two values in $\left\{\acute{\phi}_{2i}\right\}_{i=1}^{p}$ which are the closest boundaries of $\acute{\phi}_{2id}$
  end while
  ▷ Obtain the rotation angle estimates for both radars
  $\widehat{\phi}_1 \leftarrow \acute{\phi}_{1id}$
  $\widehat{\phi}_2 \leftarrow \acute{\phi}_{2id}$
  return $\widehat{\phi}_1, \widehat{\phi}_2$
end procedure

function PROCRUSTESANGLE(X_{ofov}, G)
  $W\Sigma V^T \leftarrow \text{SVD}\left(GX_{ofov}^{T}\right)$
  ▷ This is the singular value decomposition (SVD)
  ▷ Let the singular values in Σ be arranged in descending order
  $Q_{(\acute{\phi}_1)} \leftarrow W \begin{bmatrix} 1 & 0 \\ 0 & \det(WV^T) \end{bmatrix} V^T$
  ▷ The diagonal matrix ensures the determinant $\det\left(Q_{(\acute{\phi}_1)}\right) = +1$
  Obtain angle $\acute{\phi}_1$ from the 2×2 rotation matrix $Q_{(\acute{\phi}_1)}$
  return $\acute{\phi}_1$
end function

procedure (Algorithm 9) i.e.

$$\widehat{\phi}_1, \widehat{\phi}_2 = \text{ESTROTANGLES}(X_{ofov}, Y_{ofov}, vecBnd, w) \tag{5.8}$$

where *vecBnd* is a two-element vector which defines the range of angle bounds to be searched for $\widehat{\phi}_2$. The algorithm splits the vector into p divisions to make a list of angles $\left\{\acute{\phi}_{2i}\right\}_{i=1}^{p}$ (line 3 of the procedure). It then obtains the CoP solution $\acute{\phi}_{1i}$ with respect to a fixed value $\acute{\phi}_{2i}$. The cost function is evaluated for each pair of candidate solutions $\acute{\phi}_{1i}$ and $\acute{\phi}_{2i}$ (line 7). The minimum of the p cost-function values (having an index *id*) will be used to filter the candidate solutions, since the sought estimate $\widehat{\phi}_2$ is somewhere close to $\acute{\phi}_{2id}$. Therefore, the algorithm checks for two values in $\left\{\acute{\phi}_{2i}\right\}_{i=1}^{p}$ which are the closest boundaries of $\acute{\phi}_{2id}$. The two boundary values in $\left\{\acute{\phi}_{2i}\right\}_{i=1}^{p}$ make a new *vecBnd* vector (line 10) which is further split at the next iteration. The algorithm iterates in this manner until convergence (i.e. when the range of *vecBnd* becomes approximately zero) and returns the rotation angle estimates, $\widehat{\phi}_1$ and $\widehat{\phi}_2$.

5.4.2 Principle 2: A search for the center of trailer rotation

The entire rotation of the trailer will be considered in this section and subscript i will be used on the point set detections of the reflectors. We denote X_i and Y_i as the ith sets of reflector detections by the passenger radar and driver radar respectively. As the trailer rotates in the direction of both radars (Figure 5.3), the detections of a reflector would *approximately* appear in a circular path in the CCS with respect to the hitch ball origin. The path is *approximately* circular because the detections are noisy and quantized. The algorithm will find the center of trailer rotation P, which

is the hitch ball location, based on the range-invariant property of any point on a circle from its origin. In other words, the radar detections of a reflector should be approximately range-invariant from P.

Let us transform both the PR set X_i and the DR set Y_i onto the CCS as functions of the translation parameters w_1 and v:

$$X^p_{i_{(w_1,v)}} = Q_{(\widehat{\phi}_1)} X_i - \begin{bmatrix} w_1 \\ v \end{bmatrix} \mathbf{1}_k^T \tag{5.9}$$

$$\begin{aligned} Y^p_{i_{(w_1,v)}} &= Q^T_{(\widehat{\phi}_2)} Y_i - \begin{bmatrix} -(w - w_1) \\ v \end{bmatrix} \mathbf{1}_k^T \\ &= Q^T_{(\widehat{\phi}_2)} Y_i + \begin{bmatrix} w - w_1 \\ -v \end{bmatrix} \mathbf{1}_k^T \end{aligned} \tag{5.10}$$

where $\widehat{\phi}_1$ and $\widehat{\phi}_2$ are the estimated rotation angles obtained in (5.8).

We know that the range (or radius) of a 2×1 vector point $\boldsymbol{m}$ from its coordinate origin is the Euclidean norm, $\sqrt{\boldsymbol{m}^T \boldsymbol{m}}$. Let $M = \begin{bmatrix} \boldsymbol{m}_1 & \boldsymbol{m}_2 & \dots & \boldsymbol{m}_k \end{bmatrix} \in \mathbb{R}^{2 \times k}$ contain k points, the range of each point in M from the origin is contained in the vector function,

$$\boldsymbol{r}(M) = \sqrt{\operatorname{diag}\left(M^T M\right)} \in \mathbb{R}^{k \times 1}$$

where diag (.) returns the diagonal elements of its matrix argument as a column vector and $\sqrt{.}$ is taken to be an element-wise square root operation.

Therefore, $\boldsymbol{r}\left(X^p_{i_{(w_1,v)}}\right)$ and $\boldsymbol{r}\left(Y^p_{i_{(w_1,v)}}\right)$ are $k \times 1$ vector-valued functions which respectively contain the ranges of the k reflectors from the hitch ball as detected by the passenger and driver radars. Throughout the entire trailer rotation, let the total number of *unique* X_i sets be a and the total number of *unique* Y_i sets be b. *Uniqueness* means that duplicate detections have been removed. Let us populate two matrices (one for each radar) containing the ranges of the reflectors from the hitch ball:

$$R^{PR}_{(w_1,v)} = \left[\boldsymbol{r}\left(X^p_{1_{(w_1,v)}}\right) \quad \boldsymbol{r}\left(X^p_{2_{(w_1,v)}}\right) \quad \ldots \quad \boldsymbol{r}\left(X^p_{a_{(w_1,v)}}\right)\right]$$
$$R^{DR}_{(w_1,v)} = \left[\boldsymbol{r}\left(Y^p_{1_{(w_1,v)}}\right) \quad \boldsymbol{r}\left(Y^p_{2_{(w_1,v)}}\right) \quad \ldots \quad \boldsymbol{r}\left(Y^p_{b_{(w_1,v)}}\right)\right]$$

Combining both matrices in no particular order:

$$R_{(w_1,v)} = \left[R^{PR}_{(w_1,v)} \quad | \quad R^{DR}_{(w_1,v)}\right] \in \mathbb{R}^{k\times(a+b)} \tag{5.11}$$

The mth row vector in $R_{(w_1,v)}$ contains all the ranges of the mth reflector from the hitch ball as detected by both radars through the entire rotation of the trailer. We want the **minimum variance** of the values in each row vector i.e. the ranges of the detections for each reflector to be approximately the same or invariant to trailer rotation. Therefore, by taking the k row vectors as random variables and the column

vectors as observations, the translation parameters can be estimated as:

$$\widehat{w}_1, \widehat{v} = \underset{w_1, v}{\operatorname{argmin}} \ \operatorname{Tr}\left[\operatorname{cov}\left(R^T_{(w_1,v)}\right)\right] \tag{5.12}$$

where $\operatorname{cov}\left(R^T_{(w_1,v)}\right) \in \mathbb{R}^{k\times k}$ is a covariance matrix and $\operatorname{Tr}[.]$ is the trace operation which sums the diagonals of its argument matrix. This means that the estimates $\widehat{w}_1$ and $\widehat{v}$ result in the minimum sum of k variances on the diagonals of the covariance matrix.

5.5 Results and Discussion

The algorithm was tested on radar data collected at a rate of 3Hz in an experiment in which the trailer was rotated steadily about the hitch ball. Three reflectors ($k = 3$) were placed on the trailer as depicted in Figure 5.6. The required distance between the radars was measured with a meter rule to be $w = 1.6m$. The true rotation angles are $\phi_1 = 19.00^\circ$ and $\phi_2 = 20.00^\circ$, they were measured with the protractors installed on the truck mock-up as described in Figure 5.2. The true translation parameters were also measured with a meter rule to be $w_1 = 0.80m, v = 0.32m$. The estimation results, presented in Table 5.1, are discussed as follows.

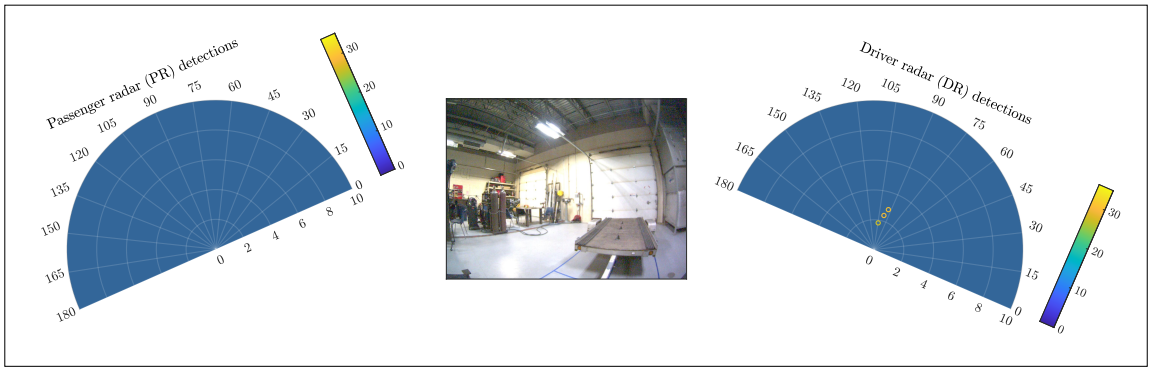

(a) The reflectors are in the driver radar FoV as the trailer rotates

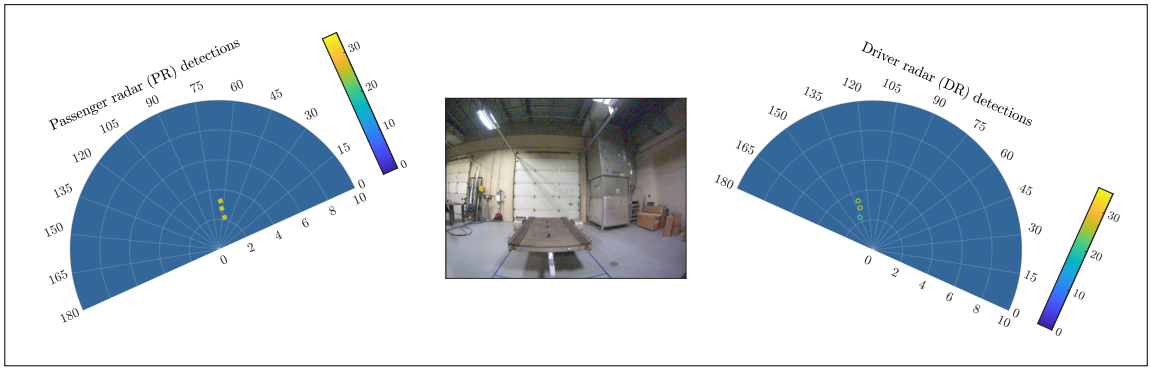

(b) The reflectors are in the overlapping FoV of the radars as the trailer rotates

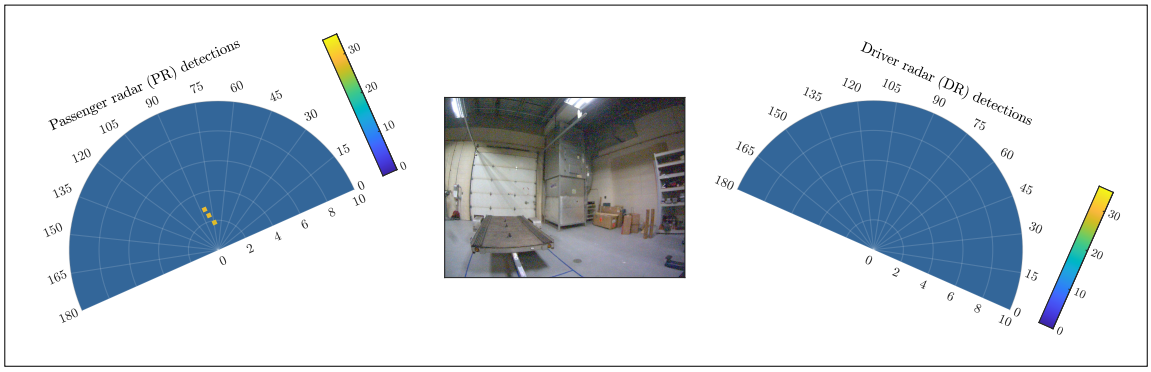

(c) The reflectors are in the passenger radar FoV as the trailer rotates

Figure 5.6: Three moments during the **rotation** of the trailer (on which three corner reflectors were placed) about the hitch ball in the direction of both radars. An empty radar detection in each subfigure indicates that the trailer was not in the radar's FoV at that moment. The clutter detections have been removed. This will not be necessary in a controlled environment.

Table 5.1
The estimates of the parameters
$k = 3$, $a = 69$, $b = 93$, $n = 10$

TRUTH		ESTIMATES	
ϕ_1	$19.00°$	$\widehat{\phi}_1$	$\mathbf{18.87°}$
ϕ_2	$20.00°$	$\widehat{\phi}_2$	$\mathbf{19.99°}$
w_1	$0.80m$	$\widehat{w}_1$	$\mathbf{0.81}\boldsymbol{m}$
v	$0.32m$	$\widehat{v}$	$\mathbf{0.35}\boldsymbol{m}$

5.5.1 Rotation angle estimates from Principle 1

The result presented here is based only on the radar detections obtained while the reflectors are in the overlapping FoV during the trailer rotation, like in Figure 5.6(b). The total number of unique radar observations in the overlapping FoV is $n = 10$. The estimates of the rotation angles were obtained using (5.8). The estimate for ϕ_2 was searched within the range $vecBnd = [0°\ \ 40°]$, which is an input vector parameter to Algorithm 9. The results obtained are $\widehat{\phi}_1 = \mathbf{18.87°}$, $\widehat{\phi}_2 = \mathbf{19.99°}$, which are within a range of $0.20°$ from the ground truth.

5.5.2 Translation parameter estimates from Principle 2

The translation parameters were estimated with respect to (5.12). The total number of unique detections through the entire trailer rotation are $a = 69$ (from the passenger radar) and $b = 93$ (from the driver radar). This means that $R_{(w_1,v)}$ in (5.11) contain 162 column vectors. The minimization problem was solved by conducting a global search over a range of lower and upper bound values for each parameter using MATLAB's `GlobalSearch` algorithm with `fmincon` as its local solver, as provided in the program's global optimization toolbox [76]. The search bounds used are $w_1 \in [0.5m \;\; 1m]$ and $v \in [0m \;\; 0.5m]$. The estimates from the global search are $\widehat{w}_1 = \mathbf{0.81}\boldsymbol{m}$ and $\widehat{v} = \mathbf{0.35}\boldsymbol{m}$, which are within $0.03m$ range from the ground truth.

5.6 Conclusion

We have presented an extrinsic calibration method for automotive radars. The method requires the distance between two radars to be known. It estimates the rotation and translation parameters needed to rigidly transform radar detections onto a common coordinate system whose origin is the hitch ball. The method uses two principles for the estimation, which are based on the detections of corner reflectors in the overlapping field of view of the radars and a search for the center of trailer rotation, the hitch ball position. The experimental results suggest that the calibration method is feasible for deployment.

A Appendix

A simulation analysis on parameter w

The algorithm presented in this work assumes that the distance between the two radars, w is known. To support the requirement for this assumption, we will discuss a [1]simulation analysis in which noisy radar detections are used to estimate the parameters based on these two cases:

Case 1: The parameter w is unknown. Three parameters ϕ_1, ϕ_2, and w will be estimated.

Case 2: The parameter w is known. Two parameters ϕ_1 and ϕ_2 will be estimated.

The objective of the analysis is to show the sensitivity of radar detection noise on the estimates for both cases. The estimates will be obtained with respect to the problem defined in (5.3) since the problem shows the relationship among the rotation angles ϕ_1, ϕ_2 and the distance w.

[1]We chose to conduct a simulation analysis, rather than a non-numerical mathematical analysis, because we did not find closed-form solutions to the problems in (5.13) and (5.14) to the best of our knowledge. In this work, (5.13) is solved by performing a global search and (5.14) is solved by using Algorithm 9 (a combination of the constrained orthogonal Procrustes solution and a grid search).

Let the estimates for Case 1 be obtained as:

$$\acute{\phi}_1, \acute{\phi}_2, \acute{w} = \underset{\phi_1,\phi_2,w}{\operatorname{argmin}} \left\| Q_{(\phi_1)} X_j - \left(Q^T_{(\phi_2)} Y_j + \begin{bmatrix} w \\ \\ 0 \end{bmatrix} \mathbf{1}^T_k \right) \right\|_F \tag{5.13}$$

and the estimates for Case 2 be obtained as:

$$\widetilde{\phi}_1, \widetilde{\phi}_2 = \underset{\phi_1,\phi_2}{\operatorname{argmin}} \left\| Q_{(\phi_1)} X_j - \left(Q^T_{(\phi_2)} Y_j + \begin{bmatrix} w \\ \\ 0 \end{bmatrix} \mathbf{1}^T_k \right) \right\|_F \tag{5.14}$$

The radar point sets X_j and Y_j in (5.13) and (5.14) are, respectively, the passenger radar and driver radar detections of reflectors placed in the overlapping FoV of both radars. Unlike (5.5), in which multiple observations are used to refine the estimates (i.e. reduce the effect of the radar detection noise), this analysis is actually concerned with the noise effect on the estimates. Therefore, unrefined estimates are considered in this analysis using one-time detection sets X_j and Y_j.

The two sets X_j, Y_j are simulated as noisy measurements of the true reflector locations (each set contains 3 points i.e. $k = 3$) in the radar coordinates,

$$X_j = X_{j_{truth}} + N_X$$

$$Y_j = Y_{j_{truth}} + N_Y$$

The true reflector locations are randomly generated, $N_{_X}$ and $N_{_Y}$ are additive zero-mean Gaussian noise matrices whose covariances are chosen as follows:

$$\text{cov}\left(N_{_X}\right) = \text{cov}\left(N_{_Y}\right) = \sigma^2 \begin{bmatrix} 1 & 0 \\ 0 & 1 \end{bmatrix} cm^2 \tag{5.15}$$

where σ is the standard deviation of the noise matrices in each uncorrelated dimension, it will be varied in the results.

The true values of the parameters to be estimated are:

$$\phi_1 = 30^\circ, \quad \phi_2 = 30^\circ, \quad w = 1.6m$$

The estimates $\acute{\phi}_1, \acute{\phi}_2, \acute{w}$ in (5.13) are obtained by conducting a global search, using MATLAB's global optimization toolbox [76], over the bounds $\phi_1, \phi_2 \in [0^\circ \;\; 40^\circ]$ and $w \in [1m \;\; 2m]$, while the estimates in (5.14) are obtained using Algorithm 9 as

$$\widetilde{\phi}_1, \widetilde{\phi}_2 = \textsc{EstRotAngles}(X_j, Y_j, vecBnd, w) \tag{5.16}$$

where $vecBnd = [0^\circ \;\; 40^\circ]$.

The performance of the estimates for both cases are assessed using these root mean

squared error (RMSE) functions.

$$\text{rmse}_{(\acute{\phi}_1,\acute{\phi}_2)} = \left(\frac{1}{2} \left\| \begin{bmatrix} \phi_1 \\ \\ \phi_2 \end{bmatrix} - \begin{bmatrix} \acute{\phi}_1 \\ \\ \acute{\phi}_2 \end{bmatrix} \right\|^2 \right)^{\frac{1}{2}} \quad deg.\ (^\circ) \tag{5.17}$$

$$\text{rmse}_{(\acute{w})} = \sqrt{(w - \acute{w})^2} \times 100 \quad cm \tag{5.18}$$

$$\text{rmse}_{(\widetilde{\phi}_1,\widetilde{\phi}_2)} = \left(\frac{1}{2} \left\| \begin{bmatrix} \phi_1 \\ \\ \phi_2 \end{bmatrix} - \begin{bmatrix} \widetilde{\phi}_1 \\ \\ \widetilde{\phi}_2 \end{bmatrix} \right\|^2 \right)^{\frac{1}{2}} \quad deg.\ (^\circ) \tag{5.19}$$

For any value of σ in (5.15), the functions in (5.17) and (5.18) provide the RMSE of the estimates for Case 1 (w is unknown), where the multiplicative factor in (5.18) converts the unit from meters to centimeters; and the function in (5.19) provides the RMSE of the estimates for Case 2 (w is known).

The parameter σ is evenly varied over 200 values in the range $0cm \leq \sigma \leq 5cm$. The RMSE for all σ values are plotted in Figure 5.7. For Case 1, the red plot shows the RMSE values of the rotation angle estimates $\acute{\phi}_1, \acute{\phi}_2$ while the black plot shows the RMSE values of the $\acute{w}$ estimates. For Case 2, the blue plot shows the RMSE values of the rotation angle estimates $\widetilde{\phi}_1, \widetilde{\phi}_2$. At $\sigma = 0cm$, all three RMSE functions return zero values, this is noticeable in the figure as all the three plots begin at the origin. This means that the estimates for both cases are accurate with noiseless data sets. However, the RMSE values differ with noisy data sets i.e when $\sigma > 0cm$. It can be observed that the rotation estimates for Case 2 (blue plot) generally result in lower

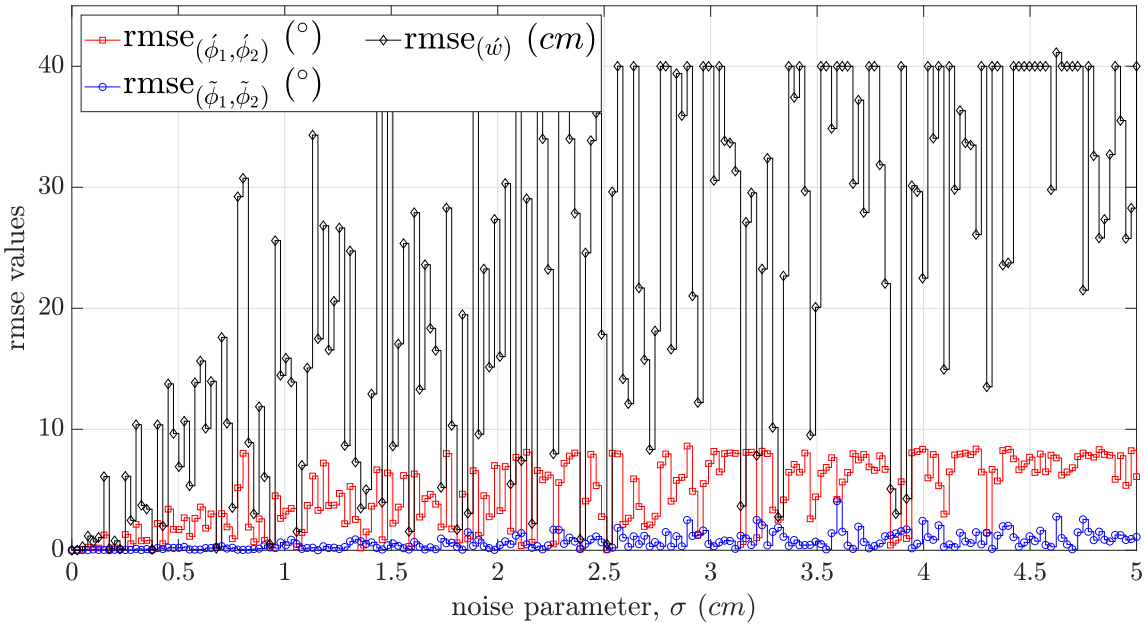

Figure 5.7: A plot showing the root mean squared error (RMSE) values of estimates, varied by a noise parameter on the point sets used for the estimation. The red and black plots are based on modelling parameter w (the distance between the two radars) as unknown, while the blue plot is based on known w.

RMSE values when compared with the rotation estimates for Case 1 (red plot). As the value of σ increases, most of the RMSE values for the estimates of w (black plot) are bounded at $40cm$, this means that the estimates returned by the global search are $\acute{w} \coloneqq 2m$, which is a boundary value in the search range $w \in [1m \;\; 2m]$.

The plots in Figure 5.7 show that the same noise N_x, N_y in the radar detections, generally result in larger estimation errors in the rotation angle estimates in Case 1 when compared with those in Case 2. In particular, the error in estimating w in Case 1 is significant. The simulation results show that the problem defined in (5.13) is ill-conditioned since small changes in the input point sets result in large changes in

the output estimates unlike the problem defined in (5.14). Hence, w is modelled as a known parameter in this work to avoid the ill-conditioned problem.

Chapter 6

Implementation of the Calibration Methods in the Trailer Angle Detection Algorithm

An algorithm which estimates the angle of trailer rotation was presented in chapter 3. The first step in the algorithm is to implement a radar fusion procedure i.e. to transform the detections from the radars onto a coordinate system centered at the hitch ball position for further signal processing. The fusion was performed in the chapter by using ground truth measurements of the radar geometry; the measurements were obtained with protractors and a meter rule. Meanwhile, the geometry parameters can be estimated using the extrinsic calibration methods presented in chapters 4 and 5.

The calibration results provided in each of the two chapters showed that the resulting estimates of the parameters are close in values to their ground truths, hence, they can be used in the trailer angle estimation algorithm. The objective of this chapter is to check if the use of the geometry parameters obtained from the calibration methods result in comparable trailer angle estimates with the use of ground truth geometry parameters.

To perform the analysis, we reuse the same radar data collected in the indoor and outdoor experiments described in section 3.6 to estimate the trailer angle. Unlike in section 3.6 where the geometry parameters were ground truth measurements, the geometry parameters obtained from the calibration methods are used in the trailer angle estimation algorithm for radar fusion. The parameters are obtained from the following sources:

(a) Extrinsic calibration algorithm presented in chapter 4. The calibration algorithm considers the geometry shown in Figure 6.1(a). The parameters are estimated with respect to two refinement methods. The estimates, as presented in the chapter, are provided below:

    i. Averaged estimates:

$$\widehat{\alpha} = 19.25^{\circ}, \quad \widehat{\beta} = 20.15^{\circ}$$

$$\widehat{w}_1 = 0.80m, \quad \widehat{w}_2 = 0.79m, \quad \widehat{v}_1 = 0.31m, \quad \widehat{v}_2 = 0.33m$$

ii. Global estimates:

$$\widehat{\alpha}_g = 19.33^\circ, \quad \widehat{\beta}_g = 19.72^\circ$$

$$\widehat{w}_{1_g} = 0.79m, \quad \widehat{w}_{2_g} = 0.81m, \quad \widehat{v}_{1_g} = 0.31m, \quad \widehat{v}_{2_g} = 0.33m$$

(b) Extrinsic calibration algorithm presented in chapter 5. The calibration method considers the geometry shown in Figure 6.1(b) and the parameter estimates presented in the chapter are:

$$\widehat{\phi}_1 = 18.87^\circ, \quad \widehat{\phi}_2 = 19.99^\circ$$

$$\widehat{w}_1 = 0.81m, \quad \widehat{v} = 0.35m$$

In total, we have **three sources of the radar geometry parameters**; two sources from the extrinsic calibration algorithm presented in chapter 4 (averaged estimates and global estimates), and the third source from the extrinsic calibration algorithm presented in chapter 5.

The trailer angle estimation results will be presented using the same notations described in chapter 3; estimation Method 1 refers to the `Detector block and the Kalman filter` algorithm, Method 2 refers to the `Augmented detector block and the Kalman filter` algorithm, δ is the angle parameter used to track the trailer when it is in motion, and $\{\theta_{interval}, \theta_{difference}\}$ are the online set learning parameters.

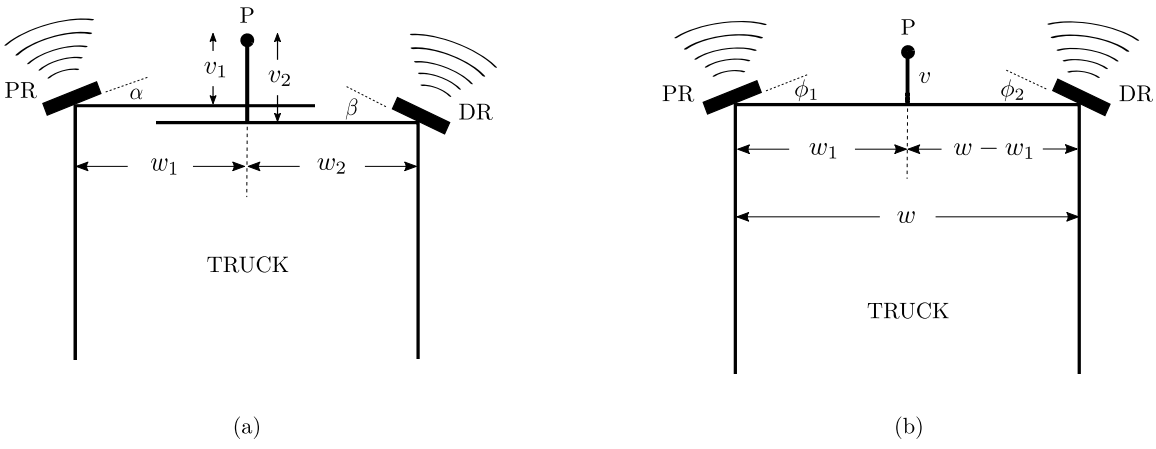

Figure 6.1: Two schematic diagrams showing the geometries of the radars with respect to the hitch ball location, P.
(a) The geometry considered in chapter 4, where P is taken as the origin of the vehicle coordinate system (VCS) as described in the chapter.
(b) The geometry considered in chapter 5, where P is taken as the origin of the common coordinate system (CCS) and the distance between the radars w is assumed to be known, as described in the chapter.

6.1 Trailer Angle Estimates with Supplemental Indoor Dataset

This section extends the results presented in section 3.6.1 by reusing the same dataset obtained in the indoor environment to estimate the trailer angle. The trailer angle

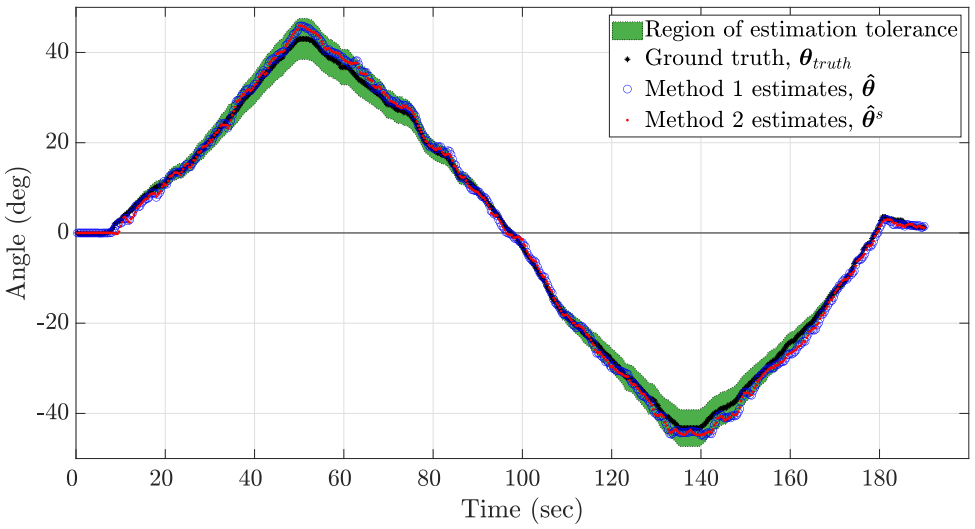

Figure 6.2: INDOOR DATASET: Radar geometry parameters obtained from the **extrinsic calibration algorithm in chapter 4 (averaged estimate refinement)**. Kalman-filtered estimates of the trailer rotation: Method 1 ($\delta = 2°$) and Method 2 ($\delta = 2°, \theta_{interval} = 5°,$ and $\theta_{difference} = 1°$).

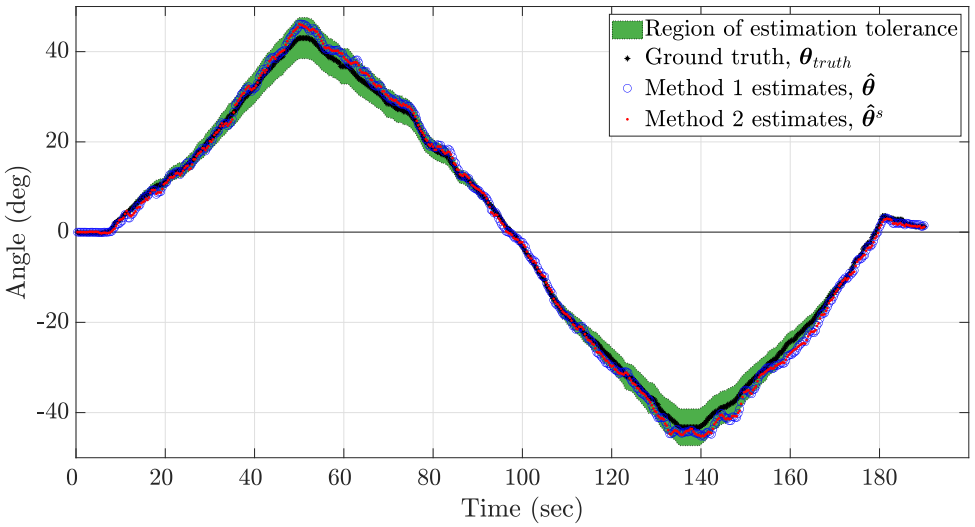

Figure 6.3: INDOOR DATASET: Radar geometry parameters obtained from the **extrinsic calibration algorithm in chapter 4 (global estimate refinement)**. Kalman-filtered estimates of the trailer rotation: Method 1 ($\delta = 2°$) and Method 2 ($\delta = 2°, \theta_{interval} = 5°,$ and $\theta_{difference} = 1°$).

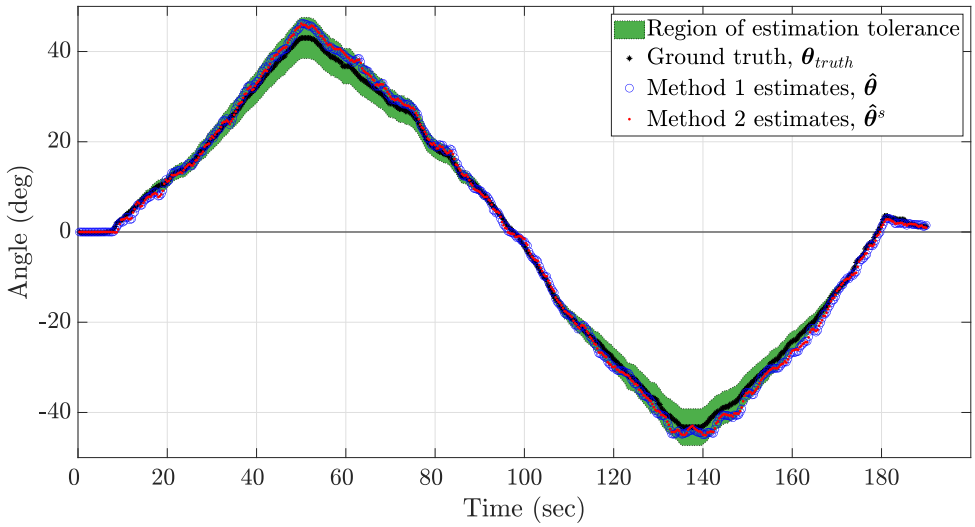

Figure 6.4: INDOOR DATASET: Radar geometry parameters obtained from the **extrinsic calibration algorithm in chapter 5**. Kalman-filtered estimates of the trailer rotation: Method 1 ($\delta = 2°$) and Method 2 ($\delta = 2°, \theta_{interval} = 5°,$ and $\theta_{difference} = 1°$).

estimates are obtained with respect to the three sources of radar geometry parameters; the estimates are plotted in Figures 6.2 to 6.4. Each figure shows the estimates for both estimation Method 1 ($\delta = 2°$) and Method 2 ($\delta = 2°, \theta_{interval} = 5°,$ and $\theta_{difference} = 1°$). More results are summarized with the root mean square (RMSE) performance metric for each estimation method in Tables 6.1 and 6.2. The estimates plotted in the figures closely look like those plotted in Figure 3.18, and the RMSE values in the two tables are also comparable with the values provided in Table 3.4 for both estimation methods. This shows that the trailer angle estimates obtained by implementing the calibrated geometry parameters are comparable with those obtained by using the ground truth geometry parameters.

Table 6.1
INDOOR DATASET: Performance metric of Method 1 trailer angle estimates $\widehat{\boldsymbol{\theta}}$ (in degrees) **based on the source of radar geometry parameters**

(a) *Extrinsic calibration algorithm in chapter 4 (averaged estimate refinement)*

	$\delta = 5°$	$\delta = 4°$	$\delta = 3°$	$\delta = 2°$	$\delta = 1°$
$RMSE_{(\widehat{\boldsymbol{\theta}})}$	1.37	1.36	1.36	1.35	1.40

(c) *Extrinsic calibration algorithm in chapter 4 (global estimate refinement)*

	$\delta = 5°$	$\delta = 4°$	$\delta = 3°$	$\delta = 2°$	$\delta = 1°$
$RMSE_{(\widehat{\boldsymbol{\theta}})}$	1.48	1.48	1.49	1.49	1.55

(d) *Extrinsic calibration algorithm in chapter 5*

	$\delta = 5°$	$\delta = 4°$	$\delta = 3°$	$\delta = 2°$	$\delta = 1°$
$RMSE_{(\widehat{\boldsymbol{\theta}})}$	1.57	1.58	1.56	1.53	1.58

Table 6.2
INDOOR DATASET: $RMSE_{(\widehat{\boldsymbol{\theta}}^s)}$ of Method 2 trailer angle estimates varied by the online set learning parameters (in degrees) **based on the source of radar geometry parameters**

(a) *Extrinsic calibration algorithm in chapter 4 (averaged estimate refinement)*

		$\theta_{difference} = 1°$					$\theta_{difference} = 2°$				
		$\delta = 5°$	$\delta = 4°$	$\delta = 3°$	$\delta = 2°$	$\delta = 1°$	$\delta = 5°$	$\delta = 4°$	$\delta = 3°$	$\delta = 2°$	$\delta = 1°$
$\theta_{interval}$	5°	1.29	1.33	1.31	1.37	1.41	1.26	1.37	1.32	1.36	1.50
	6°	1.32	1.33	1.38	1.35	1.46	1.31	1.37	1.29	1.32	1.39
	7°	1.31	1.35	1.34	1.34	1.48	1.32	1.42	1.39	1.49	1.50
	8°	1.34	1.37	1.36	1.33	1.45	1.32	1.40	1.32	1.36	1.46
	9°	1.36	1.38	1.36	1.40	1.43	1.35	1.37	1.37	1.44	1.51
	10°	1.38	1.38	1.37	1.39	1.46	1.35	1.47	1.36	1.39	1.47

(b) *Extrinsic calibration algorithm in chapter 4 (global estimate refinement)*

		$\theta_{difference} = 1°$					$\theta_{difference} = 2°$				
		$\delta = 5°$	$\delta = 4°$	$\delta = 3°$	$\delta = 2°$	$\delta = 1°$	$\delta = 5°$	$\delta = 4°$	$\delta = 3°$	$\delta = 2°$	$\delta = 1°$
$\theta_{interval}$	5°	1.46	1.45	1.44	1.48	1.52	1.36	1.48	1.43	1.55	1.37
	6°	1.47	1.46	1.46	1.46	1.49	1.35	1.33	1.44	1.34	1.49
	7°	1.45	1.43	1.47	1.46	1.55	1.35	1.52	1.45	1.46	1.53
	8°	1.47	1.48	1.46	1.44	1.51	1.45	1.33	1.44	1.56	1.27
	9°	1.46	1.48	1.47	1.50	1.51	1.45	1.41	1.45	1.54	1.52
	10°	1.50	1.51	1.51	1.55	1.53	1.51	1.49	1.49	1.43	1.43

(c) *Extrinsic calibration algorithm in chapter 5*

		$\theta_{difference} = 1°$					$\theta_{difference} = 2°$				
		$\delta = 5°$	$\delta = 4°$	$\delta = 3°$	$\delta = 2°$	$\delta = 1°$	$\delta = 5°$	$\delta = 4°$	$\delta = 3°$	$\delta = 2°$	$\delta = 1°$
$\theta_{interval}$	5°	1.57	1.53	1.57	1.51	1.57	1.43	1.65	1.69	1.62	1.51
	6°	1.58	1.54	1.54	1.52	1.56	1.51	1.61	1.53	1.66	1.47
	7°	1.55	1.53	1.52	1.50	1.60	1.53	1.65	1.51	1.65	1.49
	8°	1.57	1.57	1.57	1.53	1.58	1.43	1.65	1.52	1.61	1.71
	9°	1.54	1.56	1.52	1.55	1.57	1.48	1.61	1.57	1.61	1.56
	10°	1.57	1.57	1.55	1.54	1.60	1.44	1.67	1.52	1.64	1.58

6.2 Trailer Angle Estimates with Supplemental Outdoor Dataset

This section is also an extension of the results presented in section 3.6.2. The same dataset obtained in the outdoor environment are reused to estimate the trailer angle with respect to the three sources of radar geometry parameters.

The plots of the estimates for Method 1 ($\delta = 2°$) and Method 2 ($\delta = 2°, \theta_{interval} = 5°$, and $\theta_{difference} = 1°$) are provided in Figures 6.5 to 6.7. More results are also summarized with the RMSE performance metric in Tables 6.3 and 6.4. It can be observed that the results plotted in the figures closely look like those plotted in Figure 3.18. The RMSE values in the tables are also comparable with the values provided in Table 3.6. Again, this shows that the trailer angle estimates obtained by implementing the calibrated geometry parameters are comparable with those obtained by using the ground truth geometry parameters.

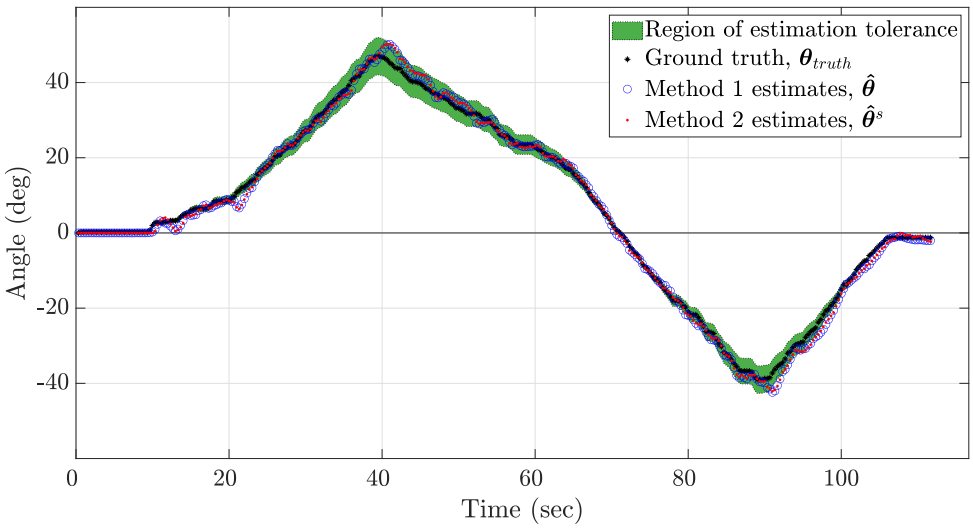

Figure 6.5: OUTDOOR DATASET: Radar geometry parameters obtained from the **extrinsic calibration algorithm in chapter 4 (averaged estimate refinement)**. Kalman-filtered estimates of the trailer rotation: Method 1 ($\delta = 2°$) and Method 2 ($\delta = 2°, \theta_{interval} = 5°,$ and $\theta_{difference} = 1°$).

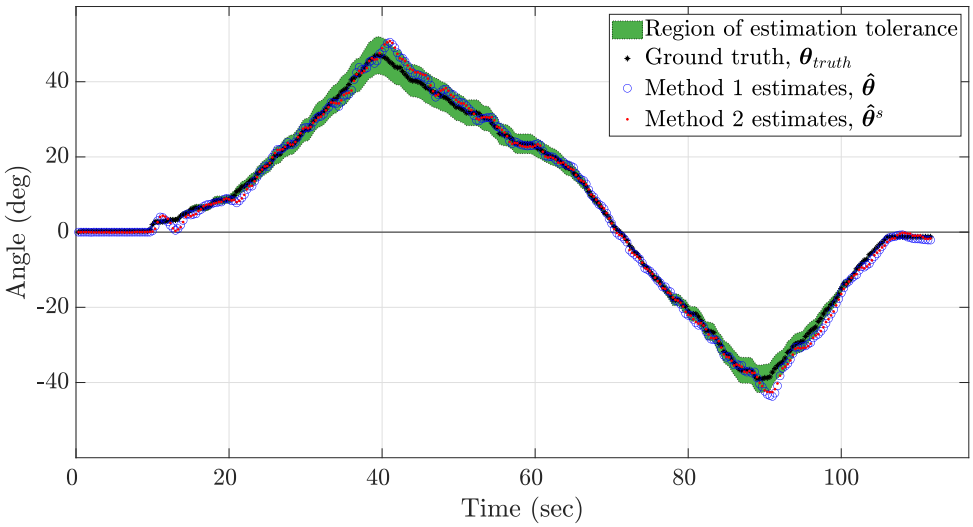

Figure 6.6: OUTDOOR DATASET: Radar geometry parameters obtained from the **extrinsic calibration algorithm in chapter 4 (global estimate refinement)**. Kalman-filtered estimates of the trailer rotation: Method 1 ($\delta = 2°$) and Method 2 ($\delta = 2°, \theta_{interval} = 5°,$ and $\theta_{difference} = 1°$).

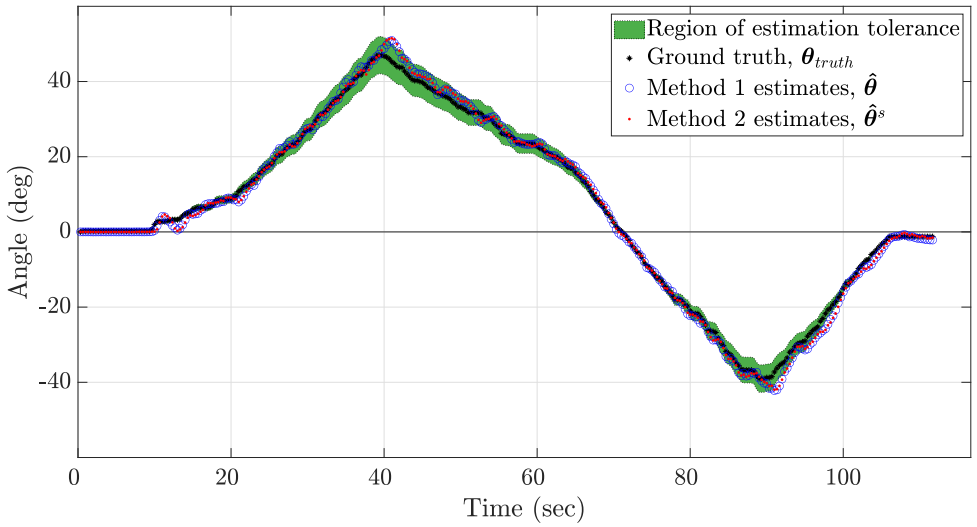

Figure 6.7: OUTDOOR DATASET: Radar geometry parameters obtained from the **extrinsic calibration algorithm in chapter 5**. Kalman-filtered estimates of the trailer rotation: Method 1 ($\delta = 2°$) and Method 2 ($\delta = 2°, \theta_{interval} = 5°,$ and $\theta_{difference} = 1°$).

Table 6.3
OUTDOOR DATASET: Performance metric of Method 1 trailer angle estimates $\widehat{\boldsymbol{\theta}}$ (in degrees) **based on the source of radar geometry parameters**

(a) *Extrinsic calibration algorithm in chapter 4 (averaged estimate refinement)*

	$\delta = 5°$	$\delta = 4°$	$\delta = 3°$	$\delta = 2°$	$\delta = 1°$
$RMSE_{(\widehat{\boldsymbol{\theta}})}$	3.12	1.67	1.51	1.54	1.73

(c) *Extrinsic calibration algorithm in chapter 4 (global estimate refinement)*

	$\delta = 5°$	$\delta = 4°$	$\delta = 3°$	$\delta = 2°$	$\delta = 1°$
$RMSE_{(\widehat{\boldsymbol{\theta}})}$	3.21	1.73	1.60	1.55	1.74

(d) *Extrinsic calibration algorithm in chapter 5*

	$\delta = 5°$	$\delta = 4°$	$\delta = 3°$	$\delta = 2°$	$\delta = 1°$
$RMSE_{(\widehat{\boldsymbol{\theta}})}$	2.97	1.77	1.61	1.64	1.83

Table 6.4

OUTDOOR DATASET: $RMSE_{(\hat{\boldsymbol{\theta}}^s)}$ of Method 2 trailer angle estimates varied by the online set learning parameters (in degrees) **based on the source of radar geometry parameters**

(a) *Extrinsic calibration algorithm in chapter 4 (averaged estimate refinement)*

		$\theta_{difference} = 1°$					$\theta_{difference} = 2°$				
		$\delta = 5°$	$\delta = 4°$	$\delta = 3°$	$\delta = 2°$	$\delta = 1°$	$\delta = 5°$	$\delta = 4°$	$\delta = 3°$	$\delta = 2°$	$\delta = 1°$
$\theta_{interval}$	5°	1.83	1.74	1.60	1.62	1.76	1.83	1.44	1.39	1.54	1.66
	6°	3.09	1.77	1.54	1.54	1.68	3.15	1.75	1.49	1.41	1.60
	7°	1.79	3.00	1.57	1.51	1.78	8.95	1.78	1.62	1.65	1.61
	8°	3.17	2.98	1.51	1.54	1.75	1.86	1.71	1.44	1.50	1.69
	9°	3.23	1.85	1.49	1.54	1.74	1.37	1.61	1.43	1.44	1.67
	10°	1.81	1.90	1.60	1.52	1.83	1.84	1.56	1.38	1.54	1.75

(b) *Extrinsic calibration algorithm in chapter 4 (global estimate refinement)*

		$\theta_{difference} = 1°$					$\theta_{difference} = 2°$				
		$\delta = 5°$	$\delta = 4°$	$\delta = 3°$	$\delta = 2°$	$\delta = 1°$	$\delta = 5°$	$\delta = 4°$	$\delta = 3°$	$\delta = 2°$	$\delta = 1°$
$\theta_{interval}$	5°	3.15	1.77	1.53	1.58	1.73	5.22	1.55	1.36	1.53	1.80
	6°	3.17	1.85	1.54	1.55	1.68	3.07	1.32	1.40	1.54	1.84
	7°	3.18	1.80	1.66	1.53	1.73	13.58	1.57	1.46	1.46	1.96
	8°	3.20	2.89	1.62	1.63	1.74	1.85	1.59	1.59	1.45	1.72
	9°	3.23	3.03	1.55	1.57	1.63	1.76	1.40	1.43	1.28	1.80
	10°	3.19	1.57	1.54	1.51	1.67	3.18	1.76	1.42	1.58	1.73

(c) *Extrinsic calibration algorithm in chapter 5*

		$\theta_{difference} = 1°$					$\theta_{difference} = 2°$				
		$\delta = 5°$	$\delta = 4°$	$\delta = 3°$	$\delta = 2°$	$\delta = 1°$	$\delta = 5°$	$\delta = 4°$	$\delta = 3°$	$\delta = 2°$	$\delta = 1°$
$\theta_{interval}$	5°	3.05	3.01	1.57	1.63	1.78	7.58	1.68	1.43	1.62	1.77
	6°	3.12	1.82	1.63	1.62	1.81	1.54	1.49	1.44	1.57	1.63
	7°	3.02	3.14	1.63	1.63	1.87	9.16	1.73	1.66	1.50	1.65
	8°	2.99	1.91	1.63	1.70	1.80	8.91	1.54	1.69	1.64	1.73
	9°	2.95	1.90	1.65	1.68	1.79	1.53	1.48	1.51	1.43	1.89
	10°	2.88	1.84	1.65	1.65	1.79	3.04	1.38	1.49	1.75	1.89

6.3 Conclusion

We have shown that the radar geometry parameters required for the fusion procedure in the trailer angle detection algorithm, which was introduced chapter 3, can be obtained by using the extrinsic calibration methods presented in chapters 4 and 5. This was demonstrated by reusing the indoor and outdoor data collected in section 3.6 of chapter 3 with respect to the calibrated geometry parameters. It is also shown that the trailer angle estimates obtained by using the calibrated geometry parameters are comparable with those obtained by using the ground truth geometry parameters.

Chapter 7

Conclusions and Research Suggestions

7.1 Conclusions

This dissertation contains algorithms which estimate the rotation of a trailer about the hitch ball of a vehicle using the point cloud detections provided by automotive radars, which are installed at the rear of the vehicle. It also contains two extrinsic calibration algorithms for radar sensor fusion. The fusion procedure is one of the steps required for the trailer rotation estimation method presented in this work.

Chapter 2 gives an account of a preliminary study of the problem. It considered two

radars which are directly located behind the vehicle, the radars' boresights are in the direction of the vehicle's longitudinal axis. Three methods based on the ordinary least squares, principal component analysis, and maximum likelihood are presented and tested using synthetic data only. The results suggest that the trailer angle estimates vary more when the radar point cloud has a large variance in the vehicle's longitudinal direction than in situations when it has a low variance in the vehicle's longitudinal direction. The performance of the maximum likelihood estimation method also depends on knowing the probability density function of the point cloud's distribution, which is a challenging task with non-synthetic data.

Chapter 3 presents another approach to the problem which considers experimental data collected from two blind spot information radars which are installed in the tail light fixtures of a truck. The radars are installed at non-zero mount angles such that their boresights are not in the direction of the vehicle's longitudinal axis. The algorithm presented estimated the trailer rotation based on the experimental data collected in both indoor and outdoor environments. The radar detections are first transformed onto a coordinate system, centered at the hitch ball position, for further signal processing. The approach then uses a rotational point set registration algorithm, which matches one set of detections obtained after trailer rotation with another baseline set of detections (referred to as the reference set), to establish rotational correspondence between the two sets and also obtain an initial rotation angle estimate. The estimate is then refined in the least squares sense by the constrained orthogonal

Procrustes optimization method. The estimates, before and after the refinement, are provided as input observations to a Kalman filter to obtain the overall estimate of the rotation angle. Two variants of the approach were presented based on the number of reference sets used for the estimation. One variant (Method 1, Detector block and the Kalman filter) uses the detections obtained at the zero-degree trailer position as its reference set and provides two input observations to the Kalman filter while the other variant (Method 2, Augmented detector block and the Kalman filter) adds a second reference set as the trailer rotates and provides four input observations to the Kalman filter. The results, based on the experiments conducted, showed that the root mean square error of trailer angle estimates obtained using both methods are comparable, and also suggested that Method 2 will be preferred in situations where Method 1 could only match very few detections for correspondence. It was also shown that the trailer angle estimates are more accurate with data collected in an indoor environment having a smooth floor surface than with data collected in an outdoor environment having a rough ground surface. The challenges identified with the outdoor-based estimation were identified and included in a list of suggested future research in chapter 7.

The first step in the estimation approach presented in chapter 3 is to transform the radar detections from their sensor coordinates onto a coordinate system centered at the hitch ball. Two extrinsic calibration methods were provided in chapters 4 and 5 to estimate the radar geometry parameters needed for the transformation.

In chapter 4, an extrinsic calibration algorithm was presented to estimate the mount angle of a radar and a translation vector needed to transform detections from the radar onto a vehicle coordinate system (VCS) whose origin is at a conveniently chosen location. The horizontal axis of the VCS aligns with the lateral line of the vehicle. The algorithm can be used with one or two radars installed either at the front or rear of a vehicle. It compares known locations of objects such as corner reflectors in the VCS with the radar detections to estimate the parameters. Different data observations are collected to obtain refined estimates of the parameters. Two refinement methods are presented; one which averages multiple estimates and another which combines all observations for global estimation. The algorithm was tested on both synthetic and experimental data collected from two radars. With respect to the radar data results obtained from both refinement methods, the estimates of the mount angles are within 0.35° range of the ground truth, while the estimates of the translation parameters are within $0.01m$ range of the ground truth.

The second extrinsic calibration algorithm discussed in chapter 5 estimates the rotation and translation parameters needed to transform the detections obtained from two blind spot information radars, having an overlapping field of view (FoV) region, onto a common coordinate system (CCS) whose origin is the hitch ball position. The horizontal axis of the CCS aligns with the straight line connecting the radars. The estimation procedure requires a trailer or rotating platform, on which corner reflectors (CRs) are placed, to be rotated about the hitch ball in the direction of both radars.

Two principles are used for the calibration. The first principle estimates the rotation parameters using the detections of CRs in the overlapping FoV of both radars as the trailer rotates. The second principle estimates the translation parameters by searching for the center of trailer rotation, the hitch ball, based on the ranges of the reflector detections. The algorithm was tested on radar data collected in an experiment, the results presented showed that the estimates of the rotation parameters are within 0.20° range of the ground truth and the estimates of the translation parameters are within $0.03m$ range from the ground truth.

Chapter 6 was introduced to combine the theories presented in chapters 3 to 5. This was necessary because the trailer angle estimation in chapter 3 was performed by using the ground truth radar geometry parameters. Meanwhile, the parameters can be estimated by using the extrinsic calibration methods presented in chapters 4 and 5. The indoor and outdoor radar data collected in section 3.6 were reused in chapter 6 to estimate the trailer angle using the same algorithm provided in chapter 3. The algorithm was used with the calibrated geometry parameters. It is shown that the trailer angle estimates obtained based on using the ground truth radar geometry are comparable with the estimates obtained based on using the calibrated radar geometry.

This dissertation has provided algorithms which estimate the rotation of a trailer

attached to a vehicle's hitch ball using radar detections obtained from multiple viewpoints. The position of the hitch ball, which is the center of rotation, was also determined in the estimation problem. In a broader sense, the work provided methods which estimate the rotation of a rigid body attached to another body at a pivot, and the rotation operation is constrained to a plane. An example of the motion model is seen in the hinge joint in anatomy, which allows motion (flexion and extension) in a plane; flexion reduces the angle between two coupled body parts while extension increases the angle between the body parts. The motion model can also be extended to three dimensions such that a rigid body which attaches to a pivot can move in a three-dimensional space as is the case for ball and socket joints. The kinematics of human joints with respect to different pivots on the body is of interest to researchers in the computer vision and the biomechanics fields. Efficient methods for finding the position of a pivot (center of rotation) and the axis of rotation in body parts are also sought in the fields. Sensors such as lidars and camera (used with markers placed on a body) provide the point detections on the body of interest from one or more viewpoints so that the body pose can be estimated for use in applications such as virtual and augmented realities. Hence, the methods provided in this dissertation or derivatives of the methods may also be helpful to study the motion of human body parts with respect to pivot joints in the body.

7.2 Suggestions for Future Research

The results presented in this dissertation have demonstrated the feasibility of the trailer angle estimation using radars, based on experiments conducted off the road. Subsequently, the algorithms presented or derivatives of the algorithms will need to be tested on the road. These are some future research directions to be considered for on-the-road experiments.

7.2.1 Mitigating the effects of radar vibration

The trailer angle estimation algorithm introduced in chapter 3 was tested in both indoor and outdoor environments. Unlike the indoor environment, the outdoor environment has a rough ground surface which makes the radars vibrate significantly as the trailer rotates during data collection. The trailer angle estimation results indicate that the vibration of the radars has effects on the performance of the algorithm. This is supported in the literature, as vehicle vibration is shown to degrade the performance of radars [32–34]. Meanwhile, the effects of the vibration can be mitigated [35–37]. Hence, it is suggested that the vibration effects be mitigated first before using the radar detections in the trailer angle estimation algorithm.

7.2.2 Multi-sensor fusion for improved trailer tracking

The algorithm presented in chapter 3 needs to track the trailer when it rotates in order to estimate the trailer angle successfully. It is shown, based on the results obtained with outdoor data, that the algorithm sometimes loses track of the trailer. Hence, radar-only detections may not be sufficient or robust to track the trailer in all situations. Therefore, it is suggested that the radars be fused with another sensor such as the camera to improve the tracking of the trailer.

7.2.3 Online radar calibration

This dissertation includes two extrinsic calibration methods which are used to estimate the radar geometry parameters needed in the trailer angle estimation algorithm. Both calibration methods make use of corner reflectors and assume that the calibration procedure is performed in a controlled environment. Hence, the calibration methods do not apply to driving situations. It will be useful if the radars self-calibrate when the vehicle is being driven. This becomes very helpful when the position and orientation of the radars gradually change. Therefore, methods which would achieve online calibration of the radars are also recommended for future research.

References

[1] K. Olutomilayo and D. R. Fuhrmann, "Estimation of trailer-vehicle articulation angle using 2d point-cloud data," in *2019 IEEE Radar Conference (RadarConf)*. IEEE, 2019, pp. 1–6.

[2] © 2019 IEEE. Reprinted, with permission, from K. Olutomilayo, D. R. Fuhrmann, Estimation of Trailer-Vehicle Articulation Angle Using 2D Point-Cloud Data, 2019 IEEE Radar Conference (RadarConf), April 2019.

[3] S. M. Patole, M. Torlak, D. Wang, and M. Ali, "Automotive radars: A review of signal processing techniques," *IEEE Signal Processing Magazine*, vol. 34, no. 2, pp. 22–35, 2017.

[4] N. Azad, A. Khajepour, and J. McPhee, "Analysis of jackknifing in articulated steer vehicles," in *Vehicle Power and Propulsion, 2005 IEEE Conference*. IEEE, 2005, pp. 86–90.

[5] Y. H. Lee, W. Deng, W. A. Hall, T. R. Brown, and J. J. Gies III, "Sensing mechanism for hitch articulation angle," Oct. 18 2005, US Patent 6,956,468.

[6] J. B. Dierker Jr, T. A. Gee, and J. Dresden III, "Articulation angle sensor," Oct. 6 1992, US Patent 5,152,544.

[7] J. J. Greenwood, S. Nicholls, and A. S. B. Crawford, "Vehicle trailer angle detection system and method," Feb. 14 2017, US Patent 9,566,911.

[8] S. T. Oreh, R. Kazemi, and S. Azadi, "A new desired articulation angle for directional control of articulated vehicles," *Proceedings of the Institution of Mechanical Engineers, Part K: Journal of multi-body dynamics*, vol. 226, no. 4, pp. 298–314, 2012.

[9] L. Chu, Y. Fang, M. Shang, J. Guo, and F. Zhou, "Estimation of articulation angle for tractor semi-trailer based on state observer," in *Measuring Technology and Mechatronics Automation (ICMTMA), 2010 International Conference on*, vol. 2. IEEE, 2010, pp. 158–163.

[10] Y. H. Lee and A. Kade, "Trailer articulation angle estimation," Mar. 8 2011, US Patent 7,904,222.

[11] NXP Semiconductors, "NXP broadens product portfolio to enable high resolution automotive radar sensors," 2018. [Online]. Available: https://is.gd/Ioaukd

[12] X.-D. Zhang, Y. Shi, and Z. Bao, "A new feature vector using selected bispectra for signal classification with application in radar target recognition," *IEEE Transactions on Signal Processing*, vol. 49, no. 9, pp. 1875–1885, 2001.

[13] P. S. Dwyer, "Some applications of matrix derivatives in multivariate analysis," *Journal of the American Statistical Association*, vol. 62, no. 318, pp. 607–625, 1967.

[14] Wolfram Research, Inc., "Mathematica, Version 11.3," Champaign, IL, 2018.

[15] S. Gavit and W. Stenson, "Vehicle-trailer angular position sensor and indicator," Sep. 3 1974, US Patent 3,833,928.

[16] C. H. Dodd, M. Boillat, J. Steeby, and S. F. Lee, "Trailer angle measurement for automated maneuvering," Mar. 1 2018, US Patent App. 15/686,540.

[17] C. Kyrtsos, T. E. Pilutti, and E. M. Lavoie, "System and method for hitch angle detection," Oct. 31 2017, US Patent 9,804,022.

[18] K. Koravadi, "Vehicle trailer angle detection system using short range communication devices," Sep. 7 2017, US Patent App. 15/446,220.

[19] Y. Lu, S. V. Byrne, P. A. VanOphem, and J. D. Harris, "Trailer angle detection system," Sep. 20 2016, US Patent 9,446,713.

[20] S. Pliefke, P. Jarmola, T. Wierich, S. V. Byrne, and Y. Lu, "Vehicle vision system with trailer angle detection," Jan. 31 2017, US Patent 9,558,409.

[21] A. S. Potnis and K. Koravadi, "Trailer angle detection using rear backup camera," Jan. 14 2020, US Patent 10,532,698.

[22] C. de Saxe and D. Cebon, "A visual template-matching method for articulation angle measurement," in *2015 IEEE 18th International Conference on Intelligent Transportation Systems*. IEEE, 2015, pp. 626–631.

[23] L. Caup, J. Salmen, I. Muharemovic, and S. Houben, "Video-based trailer detection and articulation estimation," in *2013 IEEE Intelligent Vehicles Symposium (IV)*. IEEE, 2013, pp. 1179–1184.

[24] L. Xu, E. Tseng, T. Pilutti, and S. Schondorf, "Yaw rate based trailer hitch angle estimation for trailer backup assist," SAE Technical Paper, Tech. Rep., 2017.

[25] Texas Instruments, "AWR1642 single-chip 77- and 79-GHz FMCW radar sensor datasheet (Rev. A)," 2018.

[26] H. Zhu, B. Guo, K. Zou, Y. Li, K.-V. Yuen, L. Mihaylova, and H. Leung, "A review of point set registration: From pairwise registration to groupwise registration," *Sensors*, vol. 19, no. 5, p. 1191, 2019.

[27] P. J. Besl and N. McKay, "Iterative point matching for registration of free-form curves and surfaces," *IEEE Transactions on Pattern Analysis and Machine Intelligence*, vol. 14, no. 239-256, p. 2, 1992.

[28] P. H. Schönemann, "A generalized solution of the orthogonal Procrustes problem," *Psychometrika*, vol. 31, no. 1, pp. 1–10, 1966.

[29] J. M. Ten Berge, "The rigid orthogonal Procrustes rotation problem," *Psychometrika*, vol. 71, no. 1, pp. 201–205, 2006.

[30] M. Brian, "Kalman filter package," https://www.mathworks.com/matlabcentral/fileexchange/38302-kalman-filter-package, 2020, MATLAB Central File Exchange. Retrieved June 13, 2020.

[31] MATLAB, "Matlab, Version 9.7.0.1190202 (R2019b)," Natick, Massachusetts.

[32] M. Harter and J. Hildebrandt, "Vibrations in automotive radar systems," in *2016 IEEE MTT-S International Conference on Microwaves for Intelligent Mobility (ICMIM)*. IEEE, 2016, pp. 1–4.

[33] F. Hau, F. Baumgärtner, and M. Vossiek, "Influence of vibrations on the signals of automotive integrated radar sensors," in *2017 IEEE MTT-S International Conference on Microwaves for Intelligent Mobility (ICMIM)*. IEEE, 2017, pp. 159–162.

[34] ——, "The degradation of automotive radar sensor signals caused by vehicle vibrations and other nonlinear movements," *Sensors*, vol. 20, no. 21, p. 6195, 2020.

[35] O. Longman, I. Bilik, S. Villeval, and S. Shayovitz, "Mitigation of vehicle vibration effect on automotive radar," in *2019 IEEE Radar Conference (RadarConf)*. IEEE, 2019, pp. 1–6.

[36] S. D. Da Cruz, H.-P. Beise, U. Schröder, and U. Karahasanovic, "A theoretical investigation of the detection of vital signs in presence of car vibrations and radar-based passenger classification," *IEEE Transactions on Vehicular Technology*, vol. 68, no. 4, pp. 3374–3385, 2019.

[37] G. Ciattaglia, A. De Santis, D. Disha, S. Spinsante, P. Castellini, and E. Gambi, "Performance evaluation of vibrational measurements through mmwave radars," in *2020 IEEE 7th International Workshop on Metrology for AeroSpace (MetroAeroSpace)*. IEEE, 2020, pp. 160–165.

[38] B. Hui, G. Wen, P. Zhang, and D. Li, "A novel line scan camera calibration technique with an auxiliary frame camera," *IEEE Transactions on Instrumentation and Measurement*, vol. 62, no. 9, pp. 2567–2575, 2013.

[39] Y. Liu, Q. Wang, J. Liu, J. Chen, and T. Wark, "An efficient and effective localization method for networked disjoint top-view cameras," *IEEE Transactions on Instrumentation and Measurement*, vol. 62, no. 9, pp. 2526–2537, 2013.

[40] B. Fu, Y. Wang, X. Ding, Y. Jiao, L. Tang, and R. Xiong, "Lidar-camera calibration under arbitrary configurations: Observability and methods," *IEEE Transactions on Instrumentation and Measurement*, vol. 69, no. 6, pp. 3089–3102,

2019.

[41] L. Zhou and Z. Deng, "A new algorithm for the extrinsic calibration of a 2d lidar and a camera," *Measurement Science and Technology*, vol. 25, no. 6, p. 065107, 2014.

[42] Y. Li, Y. Ruichek, and C. Cappelle, "Optimal extrinsic calibration between a stereoscopic system and a lidar," *IEEE Transactions on Instrumentation and Measurement*, vol. 62, no. 8, pp. 2258–2269, 2013.

[43] Z. Hu, Y. Li, N. Li, and B. Zhao, "Extrinsic calibration of 2-d laser rangefinder and camera from single shot based on minimal solution," *IEEE Transactions on Instrumentation and Measurement*, vol. 65, no. 4, pp. 915–929, 2016.

[44] Y. Zhuang, F. Yan, and H. Hu, "Automatic extrinsic self-calibration for fusing data from monocular vision and 3-d laser scanner," *IEEE Transactions on Instrumentation and Measurement*, vol. 63, no. 7, pp. 1874–1876, 2014.

[45] T. J. Osgood and Y. Huang, "Calibration of laser scanner and camera fusion system for intelligent vehicles using nelder–mead optimization," *Measurement Science and Technology*, vol. 24, no. 3, p. 035101, 2013.

[46] J. L. L. Galilea, J.-M. Lavest, C. A. L. Vázquez, A. G. Vicente, and I. B. Muñoz, "Calibration of a high-accuracy 3-d coordinate measurement sensor based on laser beam and cmos camera," *IEEE Transactions on Instrumentation and Measurement*, vol. 58, no. 9, pp. 3341–3346, 2009.

[47] N. Tietze, A. Ruppel, and S. Dorenkamp, "Automatic calibration of a vehicle radar sensor," Sep. 19 2019, US Patent App. 16/351,714.

[48] M. Z. Ikram and A. Ahmad, "Radar mount-angle calibration," May 21 2020, US Patent App. 16/679,404.

[49] ——, "Automated radar mount-angle calibration in automotive applications," in *2019 IEEE Radar Conference (RadarConf)*. IEEE, 2019, pp. 1–5.

[50] R. Izquierdo, I. Parra, D. Fernández-Llorca, and M. Sotelo, "Multi-radar self-calibration method using high-definition digital maps for autonomous driving," in *2018 21st International Conference on Intelligent Transportation Systems (ITSC)*. IEEE, 2018, pp. 2197–2202.

[51] J. H. Pan and J. Z. He, "On-line absolute sensor registration in 3-D radars networking," in *Proceedings of 2011 Cross Strait Quad-Regional Radio Science and Wireless Technology Conference*, vol. 2. IEEE, 2011, pp. 1085–1089.

[52] D. Sigalov, A. Gal, and B. Vigdor, "On universal sensor registration," in *2018 21st International Conference on Information Fusion (FUSION)*. IEEE, 2018, pp. 1472–1479.

[53] R. Hellinger and O. F. Schwindt, "Automotive radar alignment," Mar. 10 2020, US Patent 10,585,170.

[54] T. M. Scheschko and B. Lehnertz, "Method for calibrating a radar sensor, and radar system," Jan. 9 2018, US Patent 9,865,933.

[55] K. S. Arun, T. S. Huang, and S. D. Blostein, "Least-squares fitting of two 3-D point sets," *IEEE Transactions on pattern analysis and machine intelligence*, no. 5, pp. 698–700, 1987.

[56] T. Huang, S. Blostein, and E. Margerum, "Least-squares estimation of motion parameters from 3-D point correspondences," in *Proc. IEEE Conf. Computer Vision and Pattern Recognition*, vol. 10, 1986, pp. 112–115.

[57] W. Kabsch, "A discussion of the solution for the best rotation to relate two sets of vectors," *Acta Crystallographica Section A: Crystal Physics, Diffraction, Theoretical and General Crystallography*, vol. 34, no. 5, pp. 827–828, 1978.

[58] W. R. Bennett, "Spectra of quantized signals," *The Bell System Technical Journal*, vol. 27, no. 3, pp. 446–472, 1948.

[59] B. Widrow, "Statistical analysis of amplitude-quantized sampled-data systems," *Transactions of the American Institute of Electrical Engineers, Part II: Applications and Industry*, vol. 79, no. 6, pp. 555–568, 1961.

[60] S. Sharenson, "Angle estimation accuracy with a monopulse radar in the search mode," *IRE Transactions on Aerospace and Navigational Electronics*, no. 3, pp. 175–179, 1962.

[61] D. J. Rumsey, *Intermediate statistics for dummies.* John Wiley & Sons, 2007.

[62] MATLAB, "Matlab, Version 9.7.0.1190202 (R2020a)," Natick, Massachusetts.

[63] J. Kim, D. S. Han, and B. Senouci, "Radar and vision sensor fusion for object detection in autonomous vehicle surroundings," in *2018 Tenth International Conference on Ubiquitous and Future Networks (ICUFN).* IEEE, 2018, pp. 76–78.

[64] C. Schöller, M. Schnettler, A. Krämmer, G. Hinz, M. Bakovic, M. Güzet, and A. Knoll, "Targetless rotational auto-calibration of radar and camera for intelligent transportation systems," in *2019 IEEE Intelligent Transportation Systems Conference (ITSC).* IEEE, 2019, pp. 3934–3941.

[65] D. Cormack, I. Schlangen, J. R. Hopgood, and D. E. Clark, "Joint registration and fusion of an infrared camera and scanning radar in a maritime context," *IEEE Transactions on Aerospace and Electronic Systems*, vol. 56, no. 2, pp. 1357–1369, 2019.

[66] J. Peršić, I. Marković, and I. Petrović, "Extrinsic 6dof calibration of a radar–lidar–camera system enhanced by radar cross section estimates evaluation," *Robotics and Autonomous Systems*, vol. 114, pp. 217–230, 2019.

[67] J. Domhof, K. J. FP *et al.*, "An extrinsic calibration tool for radar, camera and lidar," in *2019 International Conference on Robotics and Automation (ICRA).* IEEE, 2019, pp. 8107–8113.

[68] R. Helmick and T. Rice, "Removal of alignment errors in an integrated system of two 3-D sensors," *IEEE Transactions on Aerospace and Electronic Systems*, vol. 29, no. 4, pp. 1333–1343, 1993.

[69] F. Vasconcelos, J. P. Barreto, and U. Nunes, "A minimal solution for the extrinsic calibration of a camera and a laser-rangefinder," *IEEE transactions on pattern analysis and machine intelligence*, vol. 34, no. 11, pp. 2097–2107, 2012.

[70] C. Stauffer and K. Tieu, "Automated multi-camera planar tracking correspondence modeling," in *2003 IEEE Computer Society Conference on Computer Vision and Pattern Recognition, 2003. Proceedings.*, vol. 1. IEEE, 2003, pp. I–I.

[71] S. Khan and M. Shah, "Consistent labeling of tracked objects in multiple cameras with overlapping fields of view," *IEEE Transactions on Pattern Analysis and Machine Intelligence*, vol. 25, no. 10, pp. 1355–1360, 2003.

[72] L. Lee, R. Romano, and G. Stein, "Monitoring activities from multiple video streams: Establishing a common coordinate frame," *IEEE Transactions on pattern analysis and machine intelligence*, vol. 22, no. 8, pp. 758–767, 2000.

[73] S. Xie, D. Yang, K. Jiang, and Y. Zhong, "Pixels and 3-D points alignment method for the fusion of camera and lidar data," *IEEE Transactions on Instrumentation and Measurement*, vol. 68, no. 10, pp. 3661–3676, 2018.

[74] S. Khan, O. Javed, and M. Shah, "Tracking in uncalibrated cameras with overlapping field of view," in *2nd IEEE Workshop on Performance Evaluation of Tracking and Surveillance*, vol. 5, 2001.

[75] D. S. Ly, C. Demonceaux, P. Vasseur, and C. Pégard, "Extrinsic calibration of heterogeneous cameras by line images," *Machine vision and applications*, vol. 25, no. 6, pp. 1601–1614, 2014.

[76] MATLAB, "Matlab, Version 9.7.0.1190202 (R2020a)," Natick, Massachusetts.

Copyright documentation

Chapter 2:

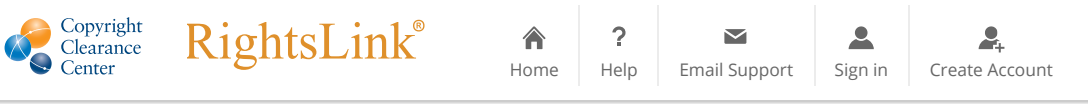

Estimation of Trailer-Vehicle Articulation Angle Using 2D Point-Cloud Data

Conference Proceedings: 2019 IEEE Radar Conference (RadarConf)

Author: [::Kunle::] [::Olutomilayo::]; Daniel R. Fuhrmann

Publisher: IEEE

Date: 22-26 April 2019

Copyright © 2019, IEEE

Thesis / Dissertation Reuse

The IEEE does not require individuals working on a thesis to obtain a formal reuse license, however, you may print out this statement to be used as a permission grant:

Requirements to be followed when using any portion (e.g., figure, graph, table, or textual material) of an IEEE copyrighted paper in a thesis:

1) In the case of textual material (e.g., using short quotes or referring to the work within these papers) users must give full credit to the original source (author, paper, publication) followed by the IEEE copyright line © 2011 IEEE.
2) In the case of illustrations or tabular material, we require that the copyright line © [Year of original publication] IEEE appear prominently with each reprinted figure and/or table.
3) If a substantial portion of the original paper is to be used, and if you are not the senior author, also obtain the senior author's approval.

Requirements to be followed when using an entire IEEE copyrighted paper in a thesis:

1) The following IEEE copyright/ credit notice should be placed prominently in the references: © [year of original publication] IEEE. Reprinted, with permission, from [author names, paper title, IEEE publication title, and month/year of publication]
2) Only the accepted version of an IEEE copyrighted paper can be used when posting the paper or your thesis on-line.
3) In placing the thesis on the author's university website, please display the following message in a prominent place on the website: In reference to IEEE copyrighted material which is used with permission in this thesis, the IEEE does not endorse any of [university/educational entity's name goes here]'s products or services. Internal or personal use of this material is permitted. If interested in reprinting/republishing IEEE copyrighted material for advertising or promotional purposes or for creating new collective works for resale or redistribution, please go to http://www.ieee.org/publications_standards/publications/rights/rights_link.html to learn how to obtain a License from RightsLink.

If applicable, University Microfilms and/or ProQuest Library, or the Archives of Canada may supply single copies of the dissertation.

BACK CLOSE WINDOW